Advanced Suspended Sediment Sampling and Simulation of Sediment Pulses to Better Predict Fluvial Geomorphic Change in River Networks

Muneer Ahammad

Dissertation submitted to the Faculty of the
Virginia Polytechnic Institute and State University
in partial fulfillment of the requirements for the degree of

Doctor of Philosophy
in
Biological Systems Engineering

Jonathan A Czuba, Chair
Theresa M Thompson
William Cully Hession
Kyle Brent Strom

May 10, 2022
Blacksburg, Virginia

Keywords: Sediment transport, Sediment pulse, Debris flow, River network model, Bedload, Suspended sediment, LISST-SL2, Nisqually River, Jordanelle Reservoir

Advanced Suspended Sediment Sampling and Simulation of Sediment Pulses to Better Predict Fluvial Geomorphic Change in River Networks

Muneer Ahammad

ABSTRACT

Sediment, an integral part of rivers and watersheds, is eroded from, stored in, and transported through various watershed components. Rivers often receive sediment in the form of episodic, discrete pulses from a variety of natural and anthropogenic processes, this sediment can be transported downstream along the bed or suspended in the water column. Most sediment measurements are focused on the component suspended in the water column. Recent advances in data collection techniques have substantially increased both the resolution and spatial scale of data on suspended sediment dynamics, which is helpful in linking small, site-scale measurements of transport processes in the field with large-scale modeling efforts. Part of this research evaluates the accuracy of the latest laser diffraction instrument for suspended-sediment measurement in rivers, LISST-SL2 for measuring suspended sediment concentration (SSC), particle size distribution (PSD), and velocity by comparing to concurrent physical samples analyzed in a lab for SSC and PSD, and velocity measured using an acoustic Doppler current profiler (ADCP) at 11 sites in Washington and Virginia during 2018-2020. Another part of this work employs a 1-D river network, bed material transport model to investigate the magnitude, timing, and persistence of downstream changes due to the introduction of sediment pulses in a linear river network. We specifically focus on comparing bed responses between mixed and uniform grain size sediment pulses. Then the model capability is utilized to explore the control of hydrograph structure on debris flow sediment transport through a more complex river network at different time horizons. Another part of this work investigates the effect of differences in spatial distribution of debris flow

sediment input to the network by analyzing corresponding tributary and mainstem characteristics. Based on an extensive dataset, our results highlight the need for a correction of the raw LISST-SL2 measurements to improve the estimation of effective density and particle size distribution with the help of a physical sample. Simulation results from the river network model show that bed response is primarily influenced by the sediment-pulse grain size and distribution. Intermediate mixed-size pulses are likely to have the largest downstream impact because finer sizes translate quickly and coarser sizes (median bed gravel size and larger) disperse slowly. Furthermore, a mixed-size pulse, with a smaller median grain size than the bed, increases bed mobility more than a uniform-size pulse. While investigating the hydrologic control on debris flow simulation, this study finds that differences between transport by a 30-year daily hydrograph and simplified hydrographs were greatest in the first few years, but errors decreased to around 10% after 10 years. Our simulation results highlight that the sequence of flows (initial high/low flow) is less important for transport of finer sediment. We show that such network-scale modeling can quantitatively identify geomorphically significant network characteristics for efficient transport from tributaries to the mainstem, and eventually to the outlet. Results suggest that watershed area and slope characteristics are important to predict aggradation hotspots in a network. However, to predict aggradation and fluvial geomorphic responses to variations in sediment supply from river network characteristics more confidently, more widespread (in several other river networks) model applications with field validation would be useful. This work has important implications for river management, as it allows us to better predict geomorphically significant tributaries and potential impact on downstream locations, which are important for river biodiversity. Model results lead the way to use of simplified flow hydrographs for different timescales, which is crucial in large-scale modeling as it is often restricted by computational capacity. Finally, given the ability for reliable quantification of a high-resolution time-series of different suspended-sediment characteristics, in-stream laser diffraction offers great po-

tential to advance our understanding of suspended-sediment transport.

Advanced Suspended Sediment Sampling and Simulation of Sediment Pulses to Better Predict Fluvial Geomorphic Change in River Networks

Muneer Ahammad

GENERAL AUDIENCE ABSTRACT

Rivers receive sediment from different natural and human sources, and water moves this sediment in various ways. These ways include along the bottom of the stream or suspended in the water. Quantifying suspended sediment in streams is an important step to estimate the threat to riverine environments as suspended sediments not only carry chemicals and pollutants, but also interact with the river bottom to affect the characteristics of streams. Measurement of suspended-sediment concentration and particle-size is critical for many engineering, ecological, and river-structure issues, but obtaining an accurate measurement of sediment quantity in a river is challenging. The recent advancement of a laser diffraction instrument allows us to obtain frequent measurements of suspended-sediment concentration and particle size by volume. We applied the most recent such instrument at 11 sites in Washington and Virginia during 2018-2020, along with concurrent water samples to measure suspended-sediment concentration and particle size by mass in a laboratory. Our analysis suggests that at least one supporting physical mass measurement be obtained to improve the estimation from laser measurement. Beside this site-scale measurement, we apply a large-scale river network model to estimate how sediment moves along the bed of rivers at large spatial extents. We simulate how this added sediment results in downstream changes in the amount of sediment in the river channel. We compare observed changes in the elevation of the stream bottom and sediment accumulation rates in a downstream lake to model results. Then we investigate the magnitude, timing, and persistence of downstream changes due to the introduction of added sediment by comparing the changes against a baseline condition

(without the added sediment). We find that the added sediment that is half as large as on the river bottom and with a range of sizes are likely to affect the largest downstream changes because smaller sizes move quickly and larger sizes move slowly. Furthermore, added sediment that is smaller than on the river bottom and with a range of sizes help more sediment on the river bottom move than if that sediment addition all had the same particle size. We also employ this model to explore the effect of flow variation and river characteristics on sediment movement. Comparing between a 30-year flow record and simplified flow records, we show that results from simplified flow records vary initially, but errors decrease after 10 years. That is, both flow records result in similar sediment movement in the long-term. In terms of aggradation from added sediment, results show that the characteristics of elevation change of the river bottom play a vital role along with the contributing landscape area. This work has important implications for river management, as it not only allows us to accurately measure suspended sediment with an advanced instrument, but also better understand how rivers and aquatic habitat are affected by variations in added sediment.

Dedication

To My Parents - the constant source of my inspiration.

I left home to write this line!

Acknowledgments

First of all, I would like to express my endless gratefulness to the almighty Allah who has provided me with the opportunity to complete this work. I want to express my gratitude to all the people around me who encouraged me to complete this dissertation directly or indirectly.

I would like to express my sincere gratitude to my adviser Dr. Jonathan A. Czuba for his guidance, encouragement, and inspiration during the past four years. He has been the best adviser I could have ever imagined and I am grateful for his support in all the projects I have endeavored on. I would also like to thank all members of Dr. Czuba's lab group. I appreciate all of their feedback, constant support, and the help during data collection.

I would also like to thank the members of my committee: Dr. Tess Wynn Thompson (Biological Systems Engineering), Dr. Cully Hession (Biological Systems Engineering), and Dr. Kyle Strom (Civil & Environmental Engineering). I am grateful for their guidance in my dissertation research. The knowledge I gained from their courses, and from StREAM Lab at Virginia Tech, is not only valuable for completing this work but also important for my future steps. Thank you to my co-authors: Dr. Brendan P. Murphy (Simon Fraser University), Dr. Allison M. Pfeiffer (Western Washington University), Dr. Patrick Belmont (Utah State University), and Christopher A. Curran (US Geological Survey). I thank B.P. Murphy, and Dr. Scott David (Postdoctoral Associate, Utah State University) for the sediment input data of Provo River network; and C.A. Curran for providing the LISST-SL2 datasest of Washington state. I am thankful for their expertise and willingness to collaborate.

Finally, I would like to thank my friends and family, particularly my wife and sister,

for their continuous support and encouragement during these years. I would like to mention my uncle Rezaul Karim, who always motivated me to dream big.

This research was partially supported by the National Science Foundation grant (NSF-EAR 1848672), the Virginia Agricultural Experiment Stations, and the USDA Hatch program (1017457). This work was also partly funded by the Federal Interagency Sedimentation Program (FISP).

Contents

List of Figures

List of Tables

Chapter 1

Introduction

Understanding the sources of sediment and delivery processes are critical to understand watershed impairment and target management practices to maintain water quality and sustain aquatic habitat (Wharton et al., 2017). As watershed managers are under pressure of growing population and changing climate, the use of advanced techniques to estimate sediment quantity and understand sediment transfer processes are gaining in importance. With increasing awareness of potential consequences of sedimentation processes, scientific studies are now focusing on basin-wide assessment of sediment sources, transport routes, and depositional sinks to predict the potential future effects on the environment. There are time-lags associated with each step from erosion of the landscape sediment to its transportation through river systems to a downstream outlet (Pizzuto et al., 2014). When sediment is emplaced on the river bed, its evolution is influenced by flow characteristics (Humphries et al., 2012; Phillips et al., 2018; Mao, 2018), river channel morphology and bed texture (Lisle, 2008), river network structure (Gran & Czuba, 2017), and watershed historical legacy (James, 2010). A thorough understanding of sediment measurement, transport, fate, and delivery is therefore necessary for effective river and watershed management.

Fine sediments easily reach stream networks from cropland, disturbed forestland, rangeland, construction sites, mined land, reclaimed land, military training grounds, landfills, waste disposal sites, and other lands where rainfall and its associated overland flow cause soil erosion. Sediments are also delivered into river networks from the surrounding watershed as discrete pulses in space and time driven by precipitation or other perturbations

(Benda & Dunne, 1997b; Gran & Czuba, 2017; Murphy et al., 2019). This stochastic supply of sediment may enter the river network from a variety of watershed sources such as uplands, ravines, banks, bluffs, landslides, and debris flows (Benda & Dunne, 1997b; Czuba et al., 2017; Murphy et al., 2019). Anthropogenic perturbations can also alter the frequency and magnitude of sediment supply, such as through dam removal (Cashman et al., 2021; Czuba et al., 2011; Dow et al., 2020; East et al., 2015, 2018; Major et al., 2012; Ritchie et al., 2018). In general, the greater the flow, the more sediment that will be conveyed by the stream. Water flow can be strong enough to suspend particles in the water column as they move downstream, or simply push them along the bottom of a waterway. As the input of sediment can be transported downstream by these two major modes, we are mostly interested in bedload and suspended load in terms of physical quantification; between which bedload is highly varying, and thus, difficult to measure (Garcia, 2008). However, recent advances in data collection techniques have made significant contribution to spatiotemporal resolution of data, and hence, site-scale measurements (locally at any site) of sediment transport processes in the field are now more useful in large-scale modeling efforts. The most recent laser diffraction instrument adapted for rivers (LISST-SL2) obtains at-a-point, high temporal resolution measurements of volumetric suspended-sediment concentration (SSC_V) and volumetric particle-size distribution (PSD_V) along with velocity, temperature, and depth (Sequoia Scientific, Inc., 2017). This technology overcomes the limitation of traditional in-situ sampling and subsequent lab analysis by eliminating time-consuming and labor-intensive efforts. However, the LISST-SL2, being a new instrument, should be thoroughly tested in different fluvial settings against physical measurements to get accurate, consistent, and reliable data (Czuba et al., 2015; Gray & Gartner, 2009).

The evolution of bed sediment is dictated by sediment characteristics, streamflow hydrology, channel and network properties (Cui & Parker, 2005; Czuba et al., 2012; Gran &

Czuba, 2017; Murphy et al., 2019; Sklar et al., 2009). When estimating sediment transport rates for given hydraulic conditions, there are choices from a wide range of procedures, many of which are transferrable to computer programs for sediment transport modeling. The Lagrangian framework based on Czuba (2018) uses a surface-based bedload equation and considers mixed-size sediment transport. This model is also capable of incorporating additional complexities that arise from channel network structure, and thus, provides excellent opportunity to explore bedload transport dynamics with changing sediment characteristics, streamflow hydrology, and channel and network properties.

With this background, this thesis presents guidance for advanced suspended sediment sampling, along with network-scale model application to investigate the effects of sediment properties, flow hydrograph, and network characteristics on bedload transport. The specific objectives of this research are to:

1. Collect physical samples of suspended sediment to evaluate accuracy of the latest laser diffraction instrument (LISST-SL2) for suspended-sediment sampling in rivers, and offer guidance on field deployment and data analysis for the LISST-SL2. (Chapter 2)

2. Build upon an existing river network model (Czuba, 2018), validate the model for the mainstem of Nisqually River, Washington, and investigate the space-time evolution of sediment pulses and their physical disturbances to downstream reaches. (Chapter 3; Ahammad et al., 2021)

3. Apply the updated river network model in the Provo River watershed of northern Utah, to explore the control of flow sequence and constant flow on debris flow transport at different time horizons. Additionally, to investigate the effect of differences in spatial distribution of debris flow sediment input to the network by analyzing corresponding tributary and mainstem characteristics. (Chapter 4)

Chapter 2

Assessment and guidance for using in-stream laser diffraction for measuring suspended sediment concentration and particle size distribution in rivers

2.1 ABSTRACT

This study compares the latest laser diffraction instrument for suspended-sediment sampling in rivers, the LISST-SL2, with concurrent physical measurement of suspended sediment concentration (SSC) and particle size distribution (PSD) and velocity measurement by an acoustic Doppler current profiler (ADCP). We collected 136 LISST-SL2 samples along with 65 physical samples for SSC measurement, and 24 physical samples for PSD measurement during 2018-2020 from 11 sites in Washington and Virginia, USA. We found a best-fit computed effective density (mass SSC/volumetric SSC) of 1.99 g/mL, ranging from 0.4 to 5.8 g/mL, which was much lower than the typical assumed value (of 2.65 g/mL) used by default by the LISST-SL2 for converting volumetric SSC to mass SSC. The PSDs from physical samples showed that the LISST-SL2 was not able to measure the finest sediment sizes in suspension. Therefore, we propose some adjustments of the LISST-SL2 data with a supporting physical sample to account for these effective density and PSD issues. When doing so, we were able to reduce the RMSRE (Root Mean Square Relative Error) to 24% from 117% for SSC, and to 49% from 78% for PSD. We also compared 65 LISST-SL2 velocity samples to concurrent

ADCP measurements. LISST-SL2 velocities were generally higher than ADCP velocities with a 21% RMSRE. Our results and guidance will allow for more accurate sampling by the LISST-SL2, which has great potential for studying spatial and temporal variation of suspended sediment characteristics in rivers.

2.2 INTRODUCTION

Quantifying suspended sediment in streams is an important step to estimate the threat to riverine environments posed by fluvial sediment and sorbed material. Suspended sediments not only carry chemicals and pollutants, but also interact with the river bed to affect the geomorphology of streams (Ahammad et al., 2021; Castro, 1995; Czuba et al., 2022; Gray and Gartner, 2009; Wharton et al., 2017). Measurement of suspended-sediment concentration and particle-size distribution is critical for many engineering, ecological, and geomorphological issues, but obtaining an accurate measurement of sediment quantity and distribution in a river is challenging (Gray and Gartner, 2009).

Traditionally, in-situ sampling and subsequent lab analysis of the collected sample has been performed to determine the mass suspended-sediment concentration (SSC_M) and particle-size distribution (PSD_M) (Edwards and Glysson, 1999; Davis, 2005; Gray et al., 2008; Gray and Landers, 2013). But this traditional technique suffers from many limitations as it is time-consuming and labor-intensive (Czuba et al., 2015). Also, routine physical SSC sampling at stations along a river are rare due to operational costs (Gray and Gartner, 2009). Alternatively, sediment-surrogate technologies have been developed that operate on turbidity, laser diffraction, pressure difference, and acoustic backscatter principles to measure certain characteristics of river sediment (Gray and Gartner, 2009; Kabir and Ahmari, 2020). These surrogate methods can provide continuous SSC at high-temporal frequency

and additionally laser diffraction also measures the PSD.

Laser diffraction has been widely used in laboratories, river, estuaries, and oceans (Agrawal et al., 1991; Agrawal and Pottsmith,1994, 2000; Agrawal and Traykovski, 2001; Czuba et al., 2015; Gartner et al., 2001; Gitto et al., 2017; Mikkelsen and Pejrup, 2000, 2001; Santos et al., 2021). The most recent laser diffraction instrument adapted for rivers (LISST-SL2) obtains at-a-point, high temporal resolution measurements of volumetric suspended-sediment concentration (SSC_V) and volumetric particle-size distribution (PSD_V) along with velocity, temperature, and depth (Sequoia Scientific, Inc., 2017). The former LISST-SL (which is now discontinued) measured volumetric SSCs and PSDs at 2-second resolution, for particles ranging from 1.8 to 415 µm in 32 log-spaced size classes. While the new LISST-SL2, which can be deployed from a bridge or a boat using a modified USGS B-reel mounted to a standard crane, takes isokinetic measurements every second and covers a wider range of particle size. The LISST-SL2 was redesigned after the LISST-SL (Czuba et al., 2015), to measure an expanded grain size range of 1-500 µm in 36 log-spaced size classes, with advanced isokinetic measurement, and improved software. Water entering this newer streamlined instrument, passes through a laser beam. Scattering of the laser beam off of the particles suspended in the water is then sensed by 36 ring detectors, and these 36 measurements are inverted to constitute particle concentrations in 36 size classes. This PSD_V is summed to get a total SSC_V and a particle density is required to convert to SSC_M (Agrawal and Mikkelsen, 2019). Collected data is displayed as numeric, time-series, and vertical profile data in real-time, and is stored for further analysis. The LISST-SL2 can record depth from 0 to 30 m, temperature from -5 to 45 °C, and velocity from 0.056 to 3.6 m/s (Sequoia Scientific, Inc., 2017).

Sediment measurement in natural environments is typically accomplished now using surrogate measurements with the advancement of technologies (Sassi et al., 2012). The Fed-

eral Interagency Sedimentation Project (FISP) that works to standardize the research and development in fluvial sediment studies, has also focused on research of indirect measurement of sediment characteristics. The LISST-SL2 shows great promise in this field as it is capable of characterizing sediment at a point in the water column instantaneously with high resolution (1 Hz) temporal data. Like any new instrument, the LISST-SL2 should be thoroughly tested in different fluvial settings against physical measurements to get accurate, consistent, and reliable data (Czuba et al., 2015; Gray and Gartner, 2009). Previous testing of the former LISST-SL found that the measured SSC_V values required applying a low effective density, of 1.24 g/mL collectively, to be consistent with independent physical samples of SSC_M (Czuba et al., 2015). That study (Czuba et al., 2015) suggested that the shortcoming of the laser-diffraction method in not being able to currently, fully account for shape effects of elongated and flaky fine particles might cause the low computed effective density compared to particle density ($\sim$2.65 g/mL). However, with the new modifications from the LISST-SL in developing the LISST-SL2, questions remain on the efficacy of the LISST-SL2 and guidance on its effective use.

Here, we evaluate the accuracy of the LISST-SL2 for measuring SSC, PSD, and velocity by comparing to concurrent physical samples analyzed in a lab for SSC and PSD, and velocity measured using an acoustic Doppler current profiler (ADCP) at 11 sites in Washington and Virginia during 2018-2020. Based on this dataset and our experiences, we also offer guidance on field deployment and data analysis to improve the accuracy of the data from the LISST-SL2. Given the ability for reliable quantification of a high-resolution time-series of different suspended-sediment characteristics, in-stream laser diffraction offers great potential to advance our understanding of suspended-sediment transport.

2.3 STUDY AREA

Our study sites included four sites in Virginia, and seven sites in Washington (Table 2.1, Figure 2.1). The Washington sites were along five different rivers (two sites on each of the Nisqually and Cowlitz Rivers), and all of those sites were at USGS gages (Table 2.1). These rivers all drain to Puget Sound, except the Cowlitz River drains to the Columbia River. The Sauk, White, and Puyallup Rivers deliver some of the largest sediment loads to the Puget Sound due to the presence of glaciated volcanic slopes in their headwaters (Curran et al., 2016; Czuba et al., 2011, 2012a; Jaeger et al., 2017; Scott, 1988). The Cowlitz River drains the southeast side of Mt. Rainier and the north side of Mount St. Helens (via the Toutle River, which is a tributary of the Cowlitz River), which are glaciated volcanoes. However, this side of Mt. Rainier receives less rainfall and supplies less sediment than the other rivers receive draining Mt. Rainier (Czuba et al., 2012a), and the U.S. Army Corps of Engineer's sediment retention structure has trapped much of Mount St. Helens' post-eruption sediment before it can reach the Cowlitz River (Bradley and Hadley, 2014). The sediment load in the upper Nisqually River, upstream of Alder Lake, is relatively large compared to downstream because of sediment and debris flows generated from Mt. Rainier (Czuba et al., 2012b; Legg et al., 2014). Because Alder Lake traps most of the sediment from the upper Nisqually River, the lower Nisqually River carries a relatively low sediment load compared to other rivers entering the Puget Sound (Curran et al., 2016; Czuba et al., 2011, 2012a). Furthermore, there is seasonal variation in suspended sediment concentration, size, and characteristics, particularly for rivers draining glaciers which often transport fine glacial flour (Fahnestock, 1963; Uhrich et al, 2015).

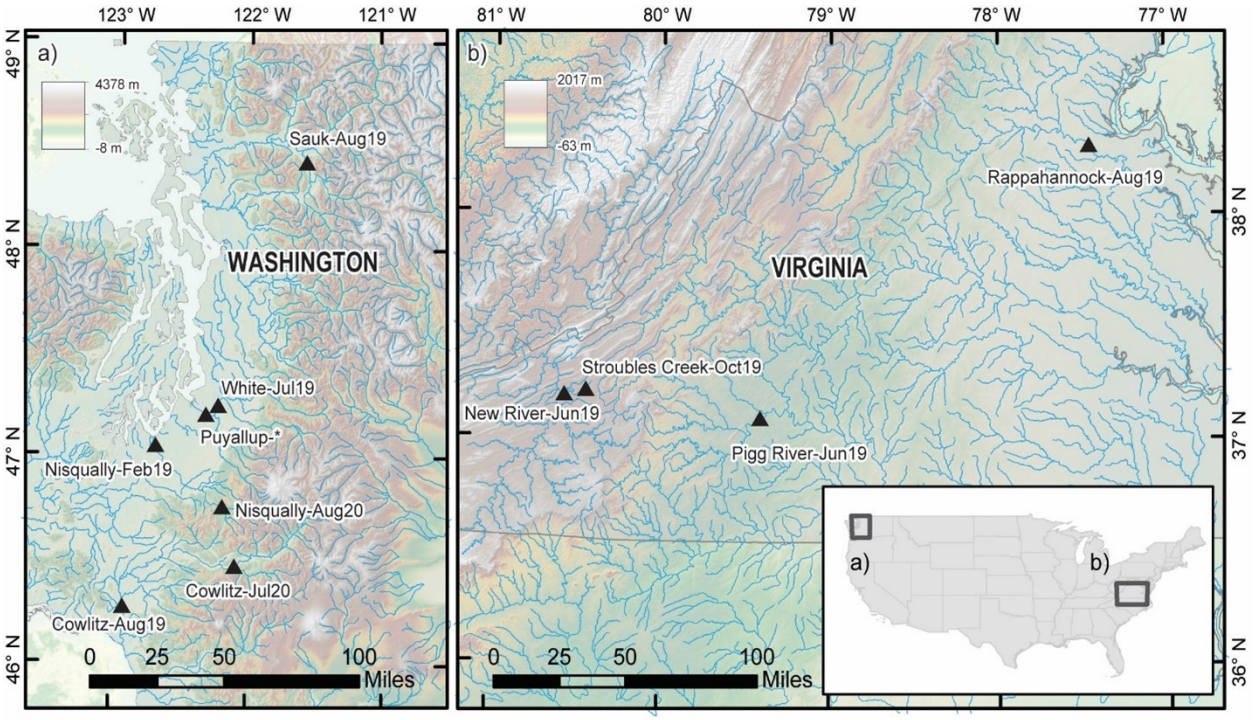

Figure 2.1: Map of the stations where samples were collected in (a) Washington and (b) Virginia. Table 2.1 provides more details of the stations and data type. *Puyallup was sampled in Dec18, Aug19, Oct19, and Aug20.

The four sites in Virginia were along four separate rivers. The Pigg and Rappahannock Rivers drain the Appalachian Piedmont and flow east, whereas the New River drains portions of North Carolina and Virginia and flows west through the Appalachian Mountains to the Kanawha and Ohio Rivers. The New River is one of the oldest rivers in the world as it cuts through and thereby predates the Appalachian Mountains (Houser, 1980). Stroubles Creek is a tributary to the New River and drains the Town of Blacksburg (Hession, 2017). The land cover of these watersheds is mainly forest, pasture, and cropland; except Stroubles Creek watershed is mostly urban. The sampling locations on Stroubles Creek and the New River are just downstream of dams forming the Duck Pond on Virginia Tech's campus (StREAM Lab; vtstreamlab.weebly.com) and Claytor Lake, respectively, that trap sediment. Flat, platy mica particles are present in the sediments of the Pigg River (Jahns et al., 1952). The

wide range of sediment types and particle sizes in these rivers provide a suitable set of sites for testing the LISST-SL2.

Table 2.1: Details of site location, date of data collection, and measured data. The * under PSD indicates that a physical sediment sample from the site was incinerated prior to PSD analysis.

Name	Location	Drainage Area (km^2)	Date	Number of LISST-SL2 measurements		Physical samples analyzed for		ADCP
				Point-integrated	Depth-integrated	SSC_M (mg/L)	PSD	Velocity (m/s)
New River-June19	New River at Whitethorne, VA (37.199°N, 80.562°W)	7500	12 June 2019	14	1	✓	✓	✓
Pigg River-June19	Pigg River at Leesville Lake, VA (37.08°N, 79.403°W)	1030	13 June 2019	11	3	✓	✓*	✓
Rappahannock-Aug19	Rappahannock River at Fredericksburg, VA (38.308°N, 77.459°W)	4144	19 Aug 2019	2		✓	✓	✓
Stroubles Creek-Oct19	Stroubles Creek at Blacksburg, VA (37.208°N, 80.448°W)	57	22 Oct 2019	1		✓	✓*	
Puyallup	Puyallup River at Puyallup, WA (USGS 12101500)	2455	12 Dec 2018, 5 Aug 2019, 22 Oct 2019, 7 Aug 2020	29	8	✓	✓ (7 Aug 2020)	✓ (12 Dec 2018, 5 Aug 2019)
Nisqually-Feb19	Nisqually River at Nisqually, WA (USGS 12090240)	1839	21 Feb 2019	25	12	✓		
Nisqually-Aug20	Nisqually River at Elbe, WA (USGS 12083400)	590	4 Aug 2020	4	1	✓	✓	
Cowlitz-Aug19	Cowlitz River at Castle Rock, WA (USGS 14243000)	5796	6 Aug 2019	5		✓		✓
Cowlitz-Jul20	Cowlitz River at Randle, WA (USGS 14231000)	1400	31 Jul 2020	5	2	✓	✓	
Sauk-Aug19	Sauk River near Sauk, WA (USGS 12189500)	1850	8 Aug 2019	4		✓		✓
White-Jul19	White River at Tacoma Ave Bridge at Sumner, WA (USGS 12101104)	1253	30 Jul 2019	9		✓		

2.4 METHOD

2.4.1 DATA COLLECTION AND LABORATORY ANALYSIS

A LISST-SL2 was deployed during 2018-2020 at 11 different sites in Washington and Virginia along with a FISP-approved physical sediment sampler (Table 2.1, Figure 2.1). A P-6 point sampler was deployed consistently at all Virginia sites, whereas at Washington sites a P-6 sampler was used only for samples collected in 2020; earlier physical samples from Washington were collected using a D-74 depth-integrating sampler (Edwards and Glysson, 1999; Davis, 2005). At three sites each in Washington and Virginia an ADCP was used to collect concurrent data on suspended sediment and flow velocity (Table 2.1, Figure 2.1). We collected 136 LISST-SL2 samples from these 11 sites, along with 65 physical samples for SSC measurement, and 24 physical samples for PSD measurement. A summary of physical sample, LISST-SL2, and ADCP results is shown in Table 2.2. All raw data along with a detailed summary of mass and volumetric suspended sediment concentrations and particle size distributions are available in USGS ScienceBase (*reference to be added here when data are published*).

At the Washington sites, a LISST-SL2 was deployed adjacent to and concurrent with either a P-6 or D-74 physical sediment sampler (Edwards and Glysson, 1999) from the

Table 2.2: Summary of physical sample, LISST-SL2, and ADCP results for the combined 2018-2020 data set

Measured Characteristic	Physical Sample			LISST-SL2				ADCP	Computed effective density (g/mL)
	SSC_M (mg/L)	Percent finer than 62.5 µm	D_{50} (µm)	SSC_V (µL/L)	Velocity (m/s)	Percent finer than 62.5 µm	Sampling duration (s)	Velocity (m/s)	
Maximum	4364	99	207	2023	2.3	100	1465	1.7	5.8
Minimum	12	1	3	13	0.5	14	11	0.2	0.4
Average	553	72	36	188	1.2	58	326	1.0	2.42
Number of samples	65	65	24	136	134	136	136	65	65

upstream side of a bridge. Occasionally, a TRDI RiverRay ADCP was concurrently deployed at the same location but from the downstream side of the bridge (Table 2.1). At the Virginia sites, a LISST-SL2 was deployed from a crane off the side of a 16-foot jon boat and afterwards, a P-6 physical sediment sampler was deployed from the same crane. Additionally, a SonTek M9 ADCP was deployed off the opposite side of the boat concurrent with the LISST-SL2 and P-6 deployments. Both depth-integrated and point-integrated measurements were collected by the LISST-SL2 and point-integrated samples were collected by a physical sampler. In all cases, point samples were collected at 0.6 depth, and when conditions allowed, samples were collected at 0.1, 0.2, 0.4, 0.8, 0.9 depths as well. Physical samples at each site in Virginia and at each depth were collected in roughly 4-10 1-L polymer bottles and each bottle was processed individually for SSC and composited in one or two groups for PSD. In Washington, physical depth-integrated samples were collected in pint-size glass bottles and point samples were collected in 1-L polymer bottles; in order to obtain enough sediment for subsequent analysis, multiple point samples from the same depth were composited into 4-L polymer containers. At Stroubles Creek, Virginia, only the LISST-SL2 was deployed off the upstream side of a bridge and a surface grab sample was collected because the P-6 sampler was not functional at the time. Also, at the Rappahannock River, Virginia, a surface grab sample was collected because the flow velocity was too low for the P-6 to collect a sample. We observed that only fines were in suspension (via the LISST-SL2) at these two sites during sampling, so the suspended sediment was well mixed and a surface sample was representative of deeper depths in the water column.

All physical samples were analyzed at either the USGS Cascades Volcanic Observatory (CVO) sediment laboratory (following Guy, 1969) or at Virginia Tech. These samples were analyzed for SSC_M (all samples) and particle-size information (7 sites) (Table 2.1). At CVO, SSC_M was calculated by filtration and particle size was analyzed using a SediGraph (Welch et

al., 1979) for particle sizes less than 63 µm and wet sieves for particle sizes greater than 63 µm. At Virginia Tech, SSC_M was calculated using the evaporation method (Guy, 1969). Samples collected at each depth from the Pigg River and Stroubles Creek, Virginia, collectively had enough suspended sediment mass to split the samples in two groups for further particle size analysis: one analyzed as is and the other first incinerated. The incinerated group of samples was placed in a furnace at 400°C for 4 hours to incinerate any organic material in the sample (APHA, 1998). At Virginia Tech in the School of Plant and Environmental Sciences, particle size of dispersed sediment samples was analyzed using a CILAS 1190 (laser diffraction) particle size analyzer (Blott et al., 2004; Gyawali and Stewart, 2019).

2.4.2 DATA ANALYSIS

The post processing included extraction of the portion of LISST-SL2 timeseries data for each depth type (point integrated or depth integrated). Each point-integrated measurement from the LISST-SL2 is the average over a roughly 5-minute time period, and from the physical sampler is the composite of a number of collected samples. We identified data points as erroneous that were not consistent with the other data at a similar depth, typically as data points with values near zero or many orders of magnitude higher. This selection was mainly based on a visual assessment of a time-series plot of concentrations. The erroneous measurements were excluded during data processing. Erroneous data were commonly found at the beginning of the instrument deployment, at times of changing depth during stationary measurements, and when measuring near the bed (e.g., clogging of pitot tube). The data were averaged over the same depth type to compute different attributes, such as depth, SSC_V, PSD_V, mean size, velocity, optical transmission, and beam attenuation. Physical samples were analyzed and displayed at corresponding depths with the LISST-SL2 measurements for SSC and PSD. The effective density of the suspended particles was then calculated by

dividing the SSC_M (from the physical samples) by the associated SSC_V (from the LISST-SL2). The ADCP velocity measurements at the corresponding depths of the LISST-SL2 were interpolated from the average (stationary) ADCP velocity profile so that the velocity measurements were not biased from selecting a value at a higher or lower depth. All reported depths in the water column were normalized with respect to total depth, where a value of zero is at the water surface and a value of one is at the bed.

The particle sizes measured by the LISST-SL2 are limited to 1–500 µm (1.21–458 µm nominal size range). Collected physical samples were analyzed for the full PSD in the laboratory where all particle sizes (1-2000 µm at CVO; 0.04-2000 µm at VT) were measured. For many sites, the particle size range measured by the LISST-SL2 was narrower than the full PSD as measured in the lab. To compare both PSDs over the range measurable by the LISST-SL2, we adjusted the LISST-SL2 PSD as described in Czuba et al. (2015) and as summarized below. Even though the lower size range of the LISST-SL2 was 1 µm, for a number of samples, we noticed a plateau of zero values on the smallest size fractions. Therefore, we used 3.1 µm as the effective lower limit of our PSD comparison. The adjustment process essentially rescales the lower end of the PSD to be equivalent to the value at that size as measured by the physical sample PSD (Figure 2.2). This is described mathematically as follows:

$$\hat{F}_L(i) = F_L(i) + [F_p(3.1\mu m) - F_L(3.1\mu m)]\frac{3.1\ \mu m - 1.21\ \mu m}{(i) - 1.21\ \mu m} \tag{2.1}$$

where $\hat{F}_L\,(i)$ is the adjusted cumulative percent finer of the LISST-SL2 PSD at the i-th grain size, $F_L\,(i)$ is the measured cumulative percent finer of the LISST-SL2 PSD at the i-th grain size, $F_p\,(i)$ is the measured cumulative percent finer of the physical sampler PSD at the i-th grain size, and i is the grain size bin of the PSD. For example, if $F_L\,(3.1\ \mu m) = 10\%$ with a corresponding $F_p\,(3.1\ \mu m) = 30\%$, then for this 3.1 μm size class, $\hat{F}_L\,(3.1\ \mu m)\ =$

$10+(30-10)\times(3.1-1.21)/(3.1-1.21)=30\%$. For the next bin size, if $F_L\,(3.66\ \mu m)=15\%$, then $\hat{F}_L\,(3.66\ \mu m)\ =15+(30-10)\times(3.1-1.21)/(3.66-1.21)=30.43\%$, and so on. This adjustment process is important because the LISST-SL2 might not be measuring all sizes present in suspension and therefore affect the accuracy of any resulting grain size metrics such as the D_{50}.

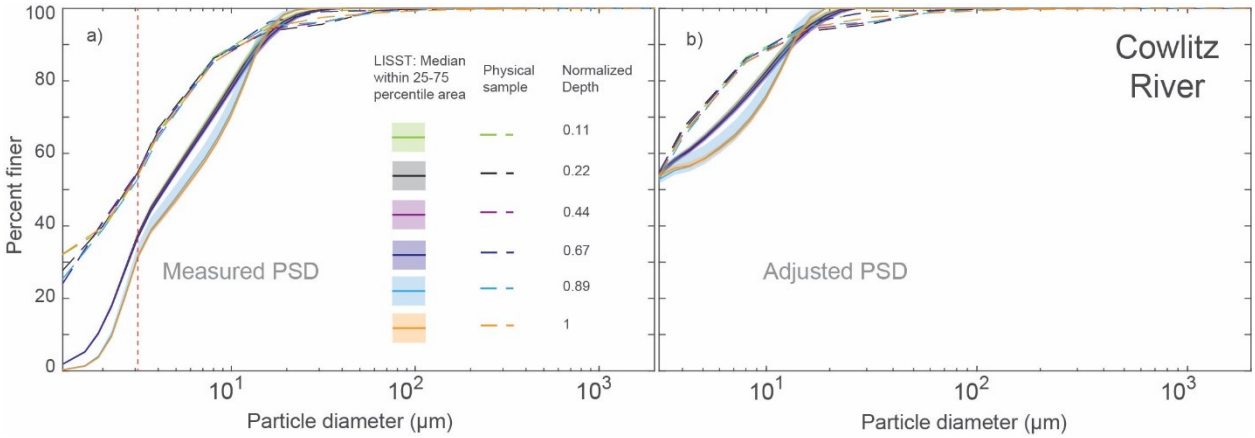

Figure 2.2: Adjustment of the LISST-SL2 particle size distribution (PSD) of Cowlitz River (Jul-20). (a) PSD measured by the LISST-SL2 (solid lines) and from physical samples (dashed lines), the orange vertical dashed line is placed at 3.1 m, (b) Adjusted LISST-SL2 PSD based on the physical sample PSD. Note the different starting points of x-axes in (a) and (b).

To quantitatively compare values measured by the LISST-SL2 and from physical samples or ADCP, we computed the statistic, Root Mean Square Relative Error (RMSRE; Despotovic et al., 2016). This statistic was calculated as,

$$RMSRE=\sqrt{\frac{1}{n}\sum_{i=1}^{n}\left(\frac{Physical\ sample-LISST\ value}{Physical\ sample}\right)^2}\times 100\% \tag{2.2}$$

The RMSRE indicates the average percentage difference of individual LISST-SL2 observations from physical sample measurements. We chose this statistic instead of the Root Mean Square Error (RMSE), or other error statistics with the same units as the input vari-

ables, because much of our data spans multiple orders of magnitude and an error value of 5 mg/L, for instance, has less relevance into an individual measurement error when the data span 10 to 5,000 mg/L.

2.5 RESULTS

We compared SSC_V (from the LISST-SL2) to SSC_M (from physical samples) for depth-integrated and point-integrated samples. We plotted SSC_M on the y-axis and SSC_V on the x-axis in log-log space with the expectation that data points will follow a linear trend, where the slope of the best-fit line through all points will give the average effective density (Figure 2.3). For the Virginia sites, because we had multiple SSC_M measurements at each depth, we plotted the range (solid rectangle) of SSC_M and SSC_V, along with mean (black dot), and 25 to 75 percentile (dashed rectangle) values. The slope of the best-fit line to the 2018-2020 data collected by the LISST-SL2 gives an average effective density of 1.99 g/mL (dashed line; Figure 2.3). However, there is a lot of variability in the effective densities measured across the sites (< 1 and > 2.65 g/mL), which we explore further below.

To investigate the potential source of variability in the computed effective densities, we plotted these values against SSC_V, SSC_M, mean size, beam attenuation, velocity, optical transmission, percent of suspended sediment finer than 62.5 µm and 10 µm (Figure 2.4). Although the data showed that effective density increased with the fraction finer than 10 µm (Figure 2.4h), we did not observe any other definitive patterns of variation of effective density with these parameters. This observation suggests that the LISST-SL2's limitation of measuring sediments in the size range 1-500 µm (Sequoia Scientific, Inc., 2017) can miss

the finest fraction of sediment in suspension (<1 µm), resulting in lower SSC_V, and thus, a higher effective density. This issue likely contributes, in part, to the high effective densities computed at the Cowlitz-Jul20 (effective density = 3.69 g/mL, percent finer than 10 µm = 77%) and Puyallup-Aug20 (effective density = 3.33 g/mL, percent finer than 10 µm = 54%; Figure 2.4h).

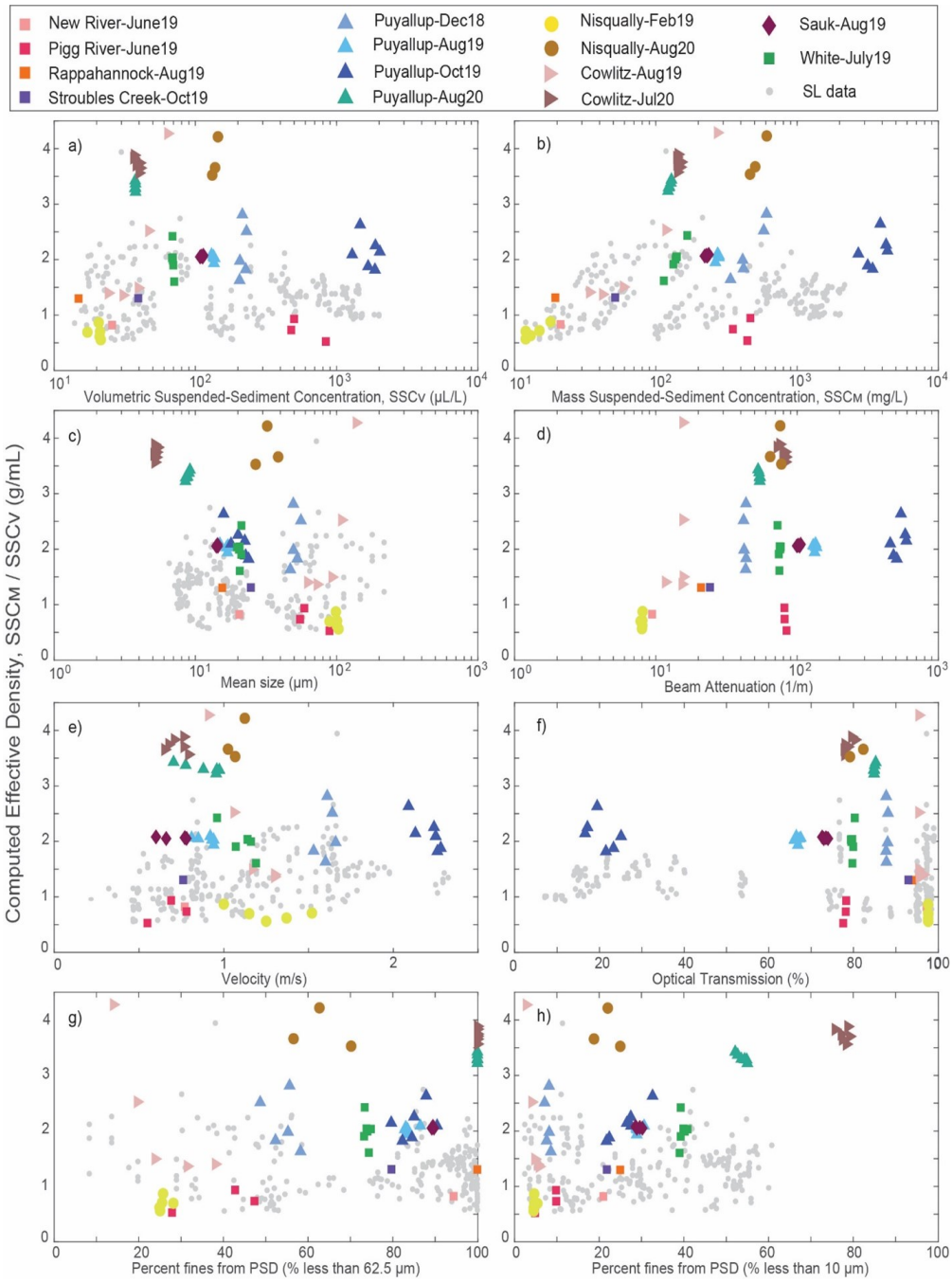

Figure 2.3: Plot of measured effective density against (a) volumetric SSC, (b) mass SSC, (c) mean size, (d) beam attenuation, (e) velocity, (f) optical transmission, (g) percent of suspended sediment finer than 62.5 µm, and (h) percent of suspended sediment finer than 10 µm. All the attributes on x-axes are from the LISST-SL2 (unadjusted), except for (b), where SSC_M is from physical samples. Available LISST-SL data from 2010-2012 (Czuba et al., 2015) are shown as gray points, except for (d) which was not reported by the LISST-SL.

Velocity measured by the LISST-SL2's differential pressure sensor (pitot tube; Sequoia Scientific, Inc., 2017) was almost always greater that the velocity measured by the ADCP (Figure 2.5). Although the two instruments are different, each with their own limitations, the data suggest that the LISST-SL2's intake velocity could be higher than the ambient water velocity, if the ADCP's velocities are accurate, which can lead to potential non-isokinetic sampling. For this case, SSC measured by the LISST-SL2 would be biased low (Edwards and Glysson, 1999; FISP, 1941). That means the computed effective density would have to be higher (than 2.65 g/mL, for instance) to account for the discrepancy. Therefore, this potential issue does not explain the low ($<$ 2.65 g/mL) computed effective densities. For our dataset, the RMSRE of the LISST-SL2's velocity measurement (relative to the ADCP measurement) was computed as 21%.

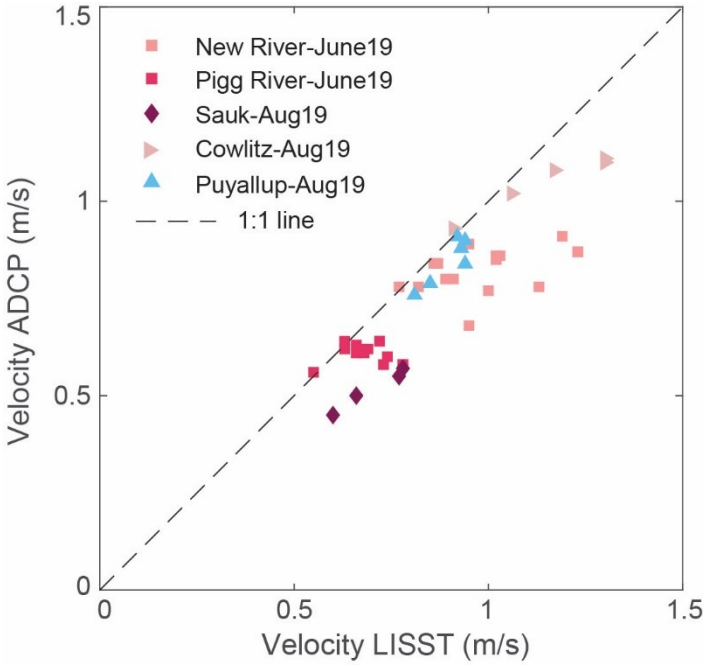

Figure 2.4: Velocity measured by the LISST-SL2 and ADCP

The optical transmission is a measure of laser power transmitted through the sample compared to clean water, and is used to compensate for the attenuation of scattered light in the LISST-SL2 (Sequoia Scientific, Inc., 2017). Whereas, the inversion of scattered light is used to compute SSC_V. These two measurements are independent and should be well correlated when particle sizes are unchanged. As data quality assurance, we plotted the logarithm of the inverse of the optical transmission as a function of SSC_V, where most data had a spread consistent with that observed from the LISST-SL and with an R^2=0.84 (Figure 2.6). This close correlation suggests that LISST-SL2 effectively measured particles in its measuring path, and did not measure more particles than were present (e.g., multiple scatting; Czuba et al., 2015; Pedocchi and García, 2006).

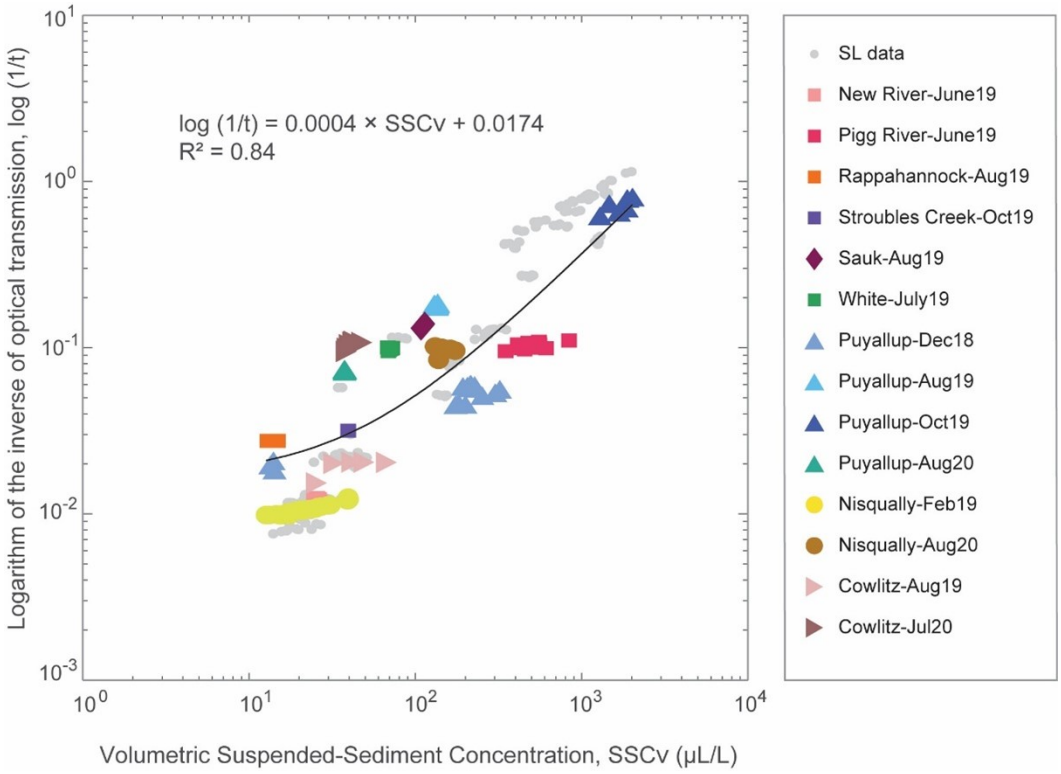

Figure 2.5: The logarithm of the inverse of the optical transmission against volumetric SSC. The black line represents a linear best-fit line through all the 2018-2020 data from the LISST-SL2. Available LISST-SL data from 2010-2012 (Czuba et al., 2015) are shown as gray points for context.

In general, we observed that the PSD coarsened as river depth increases (Figure 2.2, 2.7d-f). This was the case for both measurements from the LISST-SL2 and physical samples, and as expected because larger particles are suspended closer to the bed (Rouse, 1939; Garcia, 2008). The incinerated PSDs from the Pigg River (June) were coarser than the non-incinerated samples indicating that the suspended organic material was smaller than the suspended inorganic sediments (Figure 2.7d). However, the incinerated PSDs from Stroubles Creek (October) were finer than the non-incinerated samples indicating that the suspended organic material was larger than the suspended inorganic sediments (Figure 2.7c). Recent leaf fall and senesced plant material in October is likely responsible for the coarser particulate organic matter collected at Stroubles Creek compared to the summer measurements at the Pigg River (Jones Jr and Smock, 1991). Overall, the adjusted PSDs from the LISST-SL2 are comparable to physical samples except for the Nisqually River, where the LISST-SL2 measured much smaller particle sizes. The cause of this discrepancy was not apparent from field conditions, which were fairly shallow flows with sand boils present. Another important observation is that, sizes from the physical samples here exceeded the upper limit of LISST-SL2 particle measurement size. Physical samples had 0.2% to 8.1% of suspended materials greater than 500 µm at different depths (Figure 2.7f).

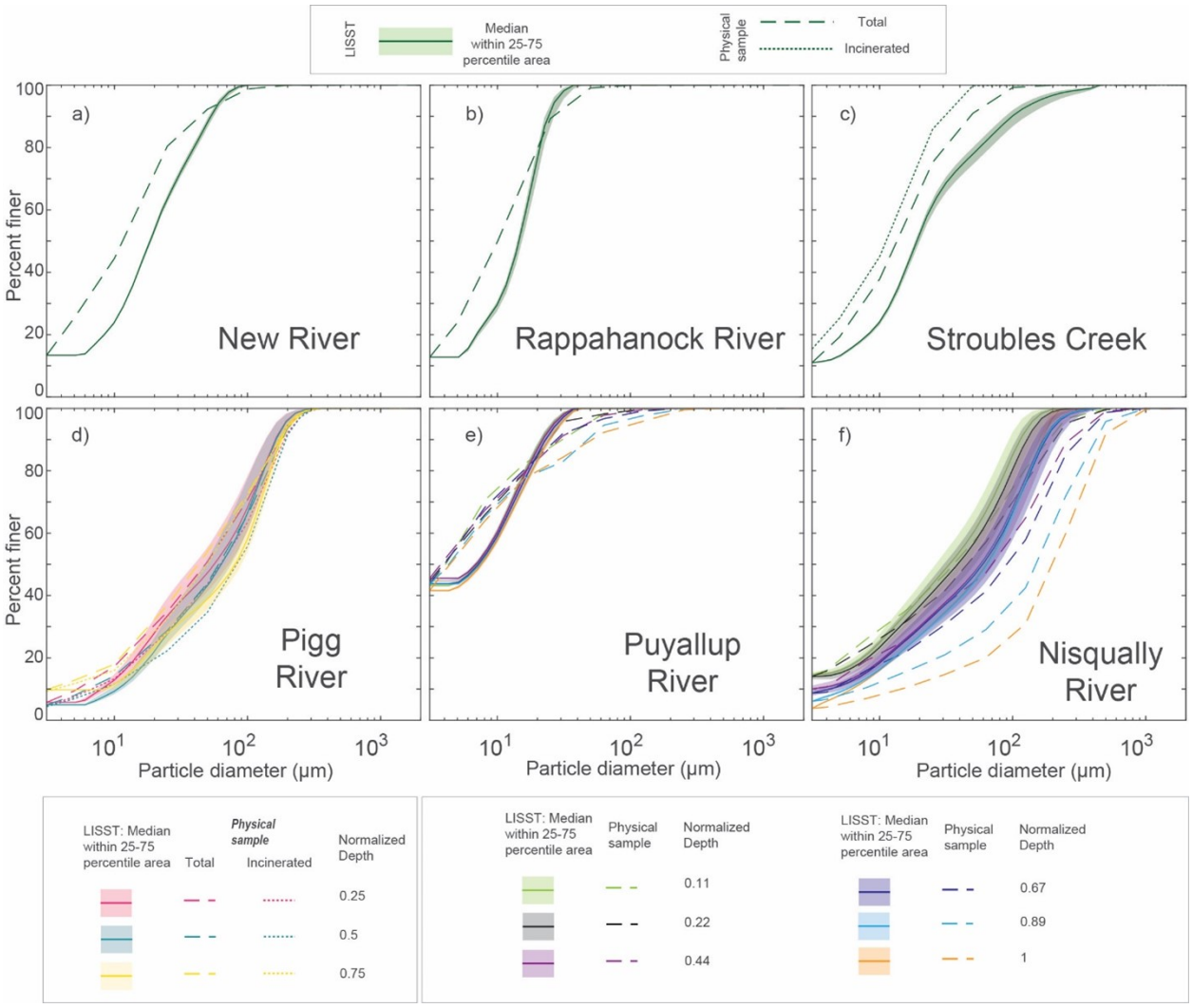

Figure 2.6: Particle-size distributions from physical samples (dashed lines; dotted lines when physical sample was incinerated), and the adjusted distributions measured by the LISST-SL2 (solid lines; shaded area represents 25-75 percentile area) measured at: (a) New River, (b) Rappahannock River, (c) Stroubles Creek, (d) Pigg River, (e) Puyallup River (Aug-20), and (f) Nisqually River (Aug-20). Note that the PSD of the Cowlitz River was shown in Figure 2.2.

We compared the median particle size from both the adjusted and unadjusted LISST-SL2 measurements against the physical samples (Figure 2.8). Because the adjustments have the most significant impact on the tails of the PSD, we selected D_{50} for comparison. In general, the LISST-SL2 reported slightly higher values than physical measurements (except

the Nisqually River). The adjustment of the particle size distributions resulted in a better comparison, with points closer to the 1:1 line compared to the raw measurement by LISST-SL2. The RMSRE for D_{50} was 78% for the measurements made directly by the LISST-SL2, whereas it was 49% after first adjusting the PSD as described above.

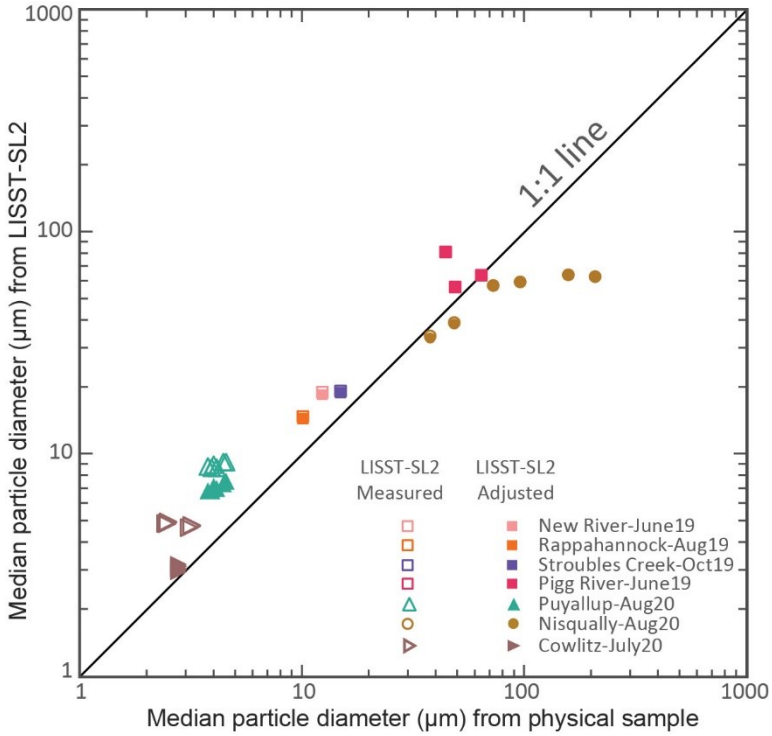

Figure 2.7: Median particle-size from PSD (measured and adjusted) of LISST-SL2, and from physical sample.

2.6 GUIDANCE FOR ADJUSTMENT OF LISST-SL2 DATA

The results from section 2.5 suggest that an adjustment of the LISST-SL2 measurements provide more accurate results for both SSC and PSD. The adjustment process included

determining and then applying a site and sampling-date specific effective density (for SSC) and also included rescaling the lower end of the PSD_V to be equivalent to the value at that size as measured by the physical sample PSD_M. The statistics (RMSRE) showed that as a result of this adjustment process the errors went down significantly (117% to 24% for SSC, and 78% to 49% for D_{50}). Therefore, we recommend LISST-SL2 users collect at least one physical sample during deployment to analyze for SSC_M and PSD_M. These data can be used to compute an effective density that should then be used to convert SSC_V to SSC_M of LISST-SL2 measurements. The physical sample PSD_M will indicate the smallest size fractions that are missed by the LISST-SL2 PSD_V measurements. It may be necessary to also rescale the PSD_V to account for missing data at the coarse end, such as where the PSD_M has some fraction over 500 µm. However, for most rivers the sizes in suspension are more likely to be finer than coarser in what the LISST-SL2 can measure. This occurred only for our Nisqually-Aug20 dataset, where 0.2% to 8.1% was coarser than 500 µm, but we did not adjust the PSD_V to account for the coarse tail of the distribution because doing so would not considerably change the D_{50}. During a LISST-SL2 deployment, collecting at least one physical sample for SSC_M and PSD_M seems to be an operationally feasible and minimal cost approach to improving data accuracy. If there is a lot of variation in PSD with depth or across the cross section, then we recommend collecting more than one physical sample.

2.7 DISCUSSION

In this study of testing the performance of the LISST-SL2, we mainly compared the LISST-SL2 measurements against physical measurements, which we treat as the "actual" conditions. However, physical measurements can also be subject to errors (both sampling and analytical),

which can be difficult to fully quantify as sampling errors arise from a variety of sources. Typically, physical measurements are considered good if the accuracy is around ±15% (Czuba et al., 2015; Gray and Landers, 2013), although errors increase as the percentage of sand in suspension increases due to the intermittent nature of sand suspension (Czuba et al., 2015; Edwards and Glysson, 1999; Topping et al., 2011). Analytical errors from USGS sediment laboratories are generally considered negligible (<1.5%; Czuba et al., 2015; USGS, 2014) compared to sampling errors (Edwards and Glysson, 1999). Therefore, some of the error that we are associating with the LISST-SL2, may arise from errors with the physical samples.

Laser diffraction instruments also have limitations due to the effects of particle shape, composition, size range, etc. (see Czuba et al., 2015). The most significant error likely arises due to the uncertainty in the apparent effective density used to convert the SSC_V to SSC_M, for which we found ranged from 0.4 to 5.8 g/mL and most often < 2.65 g/mL (Table 2.2 and Figure 2.3). Due to this issue, we investigated how different LISST-SL2 observations compare, and could explain discrepancies, with concurrent physical measurements (e.g., Figure 2.4). The only meaningful pattern we observed was that some datasets with a lot of fine sediment (large fraction finer than 10 µm) had high computed effective densities, such as the Cowlitz-Jul20 (effective density = 3.69 g/mL, percent finer than 10 µm = 77%) and Puyallup-Aug20 (effective density = 3.33 g/mL, percent finer than 10 µm = 54%; Figure 2.4h). Typically, we might think that abundance of fine sediment might equate to the potential for flocculated sediment and thus result in computed effective densities less than 2.65 g/mL (Czuba et al., 2015). However, because the LISST-SL2 can miss the finest fraction of sediment in suspension (<1 µm), and this inability to measure the same amount of sediment as captured in the physical samples can result in a lower SSC_V, and thus, a higher apparent effective density.

The LISST-SL2 uses the velocity measurement from an independent pitot tube to determine the ambient flow velocity and then pump water into the intake nozzle at the same rate to obtain an isokinetic sample that passes through the laser for measurement. The velocity measured by the LISST-SL2 was often higher than the velocity measured by ADCP (Figure 2.5), which would result in non-isokinetic sampling. When the velocity measured by the pitot tube of the LISST-SL2 is greater than the ambient stream velocity, there will be a decrease in the sample concentration relative to the actual concentration of the approaching flow (Edwards and Glysson, 1999; FISP, 1941). This type of non-isokinetic sampling alone would result in a computed effective density higher than 2.65 g/mL, and therefore, does not explain the low computed effective densities.

We do not generally recommend applying the best-fit effective density of 1.99 g/mL for LISST-SL2 datasets (see section 2.6 for guidance). A best-fit effective density for the LISST-SL was 1.24 g/mL (Czuba et al., 2015), but both of these values are highly dependent on the characteristics of the collected datasets. Other laser diffraction instruments also found low computed effective densities (1.2 – 1.75 g/mL; Williams et al., 2007; Guo and He, 2011; Andrews et al., 2010; Landers, 2012; Sassi et al., 2012), so this issue arises in the laser diffraction method in general. We did not see any evidence that the LISST-SL2 was measuring flocs (via the PSD, see Guo and He, 2011; Williams et al., 2007) and it is not clear whether flocs would even be able to remain together after being pumped into the LISST-SL2 (Czuba et al., 2015). The presence of elongated and flaky particles might be responsible to some extent for the low computed effective densities (as described by Felix et al., 2013), because the LISST-SL2 only makes adjustment for irregularly shaped, semi-rounded particles (Agrawal et al., 2008). For instance, in the Pigg River samples, it was visually apparent that flat, platy mica particles were present and the Pigg River had one of the lowest computed effective densities of 0.73 g/mL. However, it is difficult to delve any deeper into this issue

with our present data as a microscopic assessment of particle shape, surface characteristics, and/or mineralogy would be necessary. A laboratory analysis of laser diffraction, in general, or the LISST-SL2, specifically, to known sediment mineralogy and particle size of typical fluvially transported sediments could refute or support this thinking and perhaps result in a correction for fluvially transported sediment (such as Agrawal et al., 2008) that is more broadly applicable.

2.8 SUMMARY

Suspended sediment measurement by laser diffraction can offer more frequent and consistent data collection than traditional physical sampling. However, laser diffraction measures volumetric characteristics, and to convert to typical mass concentration requires knowing an effective particle density that we have rarely found to be 2.65 g/mL. We collected a comprehensive dataset of 136 LISST-SL2 samples along with 65 physical samples for SSC measurement and 24 physical samples for PSD measurement during 2018-2020 from 11 sites in Washington and Virginia, USA. These sites drain area of different physiographic settings, ranging from 57 to 7500 km^2, and provide suitable conditions for testing the LISST-SL2. The best-fit value for computed effective density was 1.99 g/mL and ranged from 0.4 to 5.8 g/mL, across a wide range of suspended sediment concentration (SSC_M: 12 - 4,364 mg/L). While the LISST-SL2 has an increased particle size range compared to the LISST-SL, we still encountered missing fractions of particles in the lowest bin sizes compared to the physical PSD measurement. This 'missing' volume is inconsistent with the low computed effective densities, because adding the 'missing' volume would decrease the effective densities further. Perhaps particle shape effects could be driving this disparity. Our results highlight the need

for a correction of the raw LISST-SL2 measurements to improve the estimation of effective density and PSD with the help of a physical sample. By doing so, we showed how this would increase the accuracy (via RMSRE) of SSC from 117% to 24% and D_{50} from 78% to 49%.

The guidance provided by this study will facilitate more reliable and effective data collection by the LISST-SL2 in the future. The laser diffraction method can continuously sample suspended sediment by grain size, and allows us to better understand the temporal characteristics of sediment transport in fluvial environments. Improving the accuracy and consistency of suspended sediment measurements by laser diffraction will help revolutionize fluvial sediment monitoring. The LISST-SL2, specifically, has great potential to study the spatial and temporal variation of suspended sediment concentration and grain-size distribution arising from turbulence and sediment supply.

Chapter 3

Simulated dynamics of mixed versus uniform grain size sediment pulses in a gravel-bedded river

3.1 ABSTRACT

Mountain rivers often receive sediment in the form of episodic, discrete pulses from a variety of natural and anthropogenic processes. Once emplaced in the river, the movement of this sediment depends on flow, grain size distribution, and channel and network geometry. Here, we simulate downstream bed elevation changes that result from discrete inputs of sediment ($\sim$10,000 m^3), differing in volume and grain size distribution, under medium and high flow conditions. We specifically focus on comparing bed responses between mixed and uniform grain-size sediment pulses. This work builds on a Lagrangian, bed-material sediment transport model and applies it to a 27-km reach of the mainstem Nisqually River, Washington, USA. We compare observed bed elevation change and accumulation rates in a downstream lake to simulation results. Then we investigate the magnitude, timing, and persistence of downstream changes due to the introduction of synthetic sediment pulses by comparing the results against a baseline condition (without pulse). Our findings suggest that bed response is primarily influenced by the sediment-pulse grain size and distribution.

Intermediate mixed-size pulses (∼50% of the median bed gravel size) are likely to have the largest downstream impact because finer sizes translate quickly and coarser sizes (median bed gravel size and larger) disperse slowly. Furthermore, a mixed-size pulse, with a smaller median grain size than the bed, increases bed mobility more than a uniform-size pulse. This work has important implications for river management, as it allows us to better understand fluvial geomorphic responses to variations in sediment supply.

3.2 INTRODUCTION

Sediments are delivered into river networks from the surrounding watershed, often as discrete pulses in space and time driven by precipitation or other perturbations (Benda & Dunne, 1997a; Gran & Czuba, 2017; Murphy et al., 2019). This stochastic supply of sediment may enter the river network from a variety of watershed sources such as uplands, ravines, banks, bluffs, landslides, and debris flows (Benda & Dunne, 1997a; Czuba et al., 2017; Murphy et al., 2019). In mountain streams, coarse sediment pulses are commonly supplied in large volumes from episodic mass movements like landslides and debris flows (Benda & Dunne, 1997a; Cui et al., 2003a, 2003b). Wildfire is a major effect of climate change and post-wildfire landscapes can deliver large quantities of sediment to streams (Benda et al., 2004a; Moody & Martin, 2004; Murphy et al., 2018, 2019; Sankey et al., 2017). Anthropogenic perturbations can also alter the frequency and magnitude of sediment supply, such as through dam removal (Cashman et al., 2021; Dow et al., 2020; East et al., 2015, 2018; Major et al., 2012; Ritchie et al., 2018) and gravel augmentation (Arnaud et al., 2017; Gaeuman et al., 2017; Welber et al., 2020). Once delivered into a river, a pulse of sediment moves downstream through some combination of translation, dispersion, and attrition of particles (An et al., 2017; Cashman

et al., 2021; Cui et al., 2003a, 2003b; Cui & Parker, 2005; East et al., 2015, 2018; Lisle, 2008; Lisle et al., 1997, 2001; Major et al., 2012; Ritchie et al., 2018; Sklar et al., 2009; Sutherland et al., 2002) or can be stored within the river and floodplain network (Cashman et al., 2021; Benda & Dunne, 1997b; Gran & Czuba, 2017).

When a sediment pulse is emplaced on the bed, the river adjusts to process the additional sediment (Cui et al., 2003a). The evolution of sediment pulses is influenced by river channel morphology and bed texture (Lisle, 2008), river network structure (Gran & Czuba, 2017), and watershed historical legacy (James, 2010). In gravel-bed rivers, sediment pulses evolve by translation when pulses are composed of fine-grained sediment, specifically finer than the underlying bed material, and when pulses have narrow grain-size distributions with small volumes (Cui et al., 2003a, 2003b; Cui & Parker, 2005; Lisle, 2008; Lisle et al., 1997, 2001; Sklar et al., 2009). In contrast, dispersion of sediment pulses occurs when the pulse has a wide grain-size distribution, sediment coarser than the preexisting bed, or a large volume relative to channel dimensions, or where the Froude number of the flow is high (>0.4) and conditions of the river promote differential transport of sediment (Cui et al., 2003a, 2003b; Cui & Parker, 2005; East et al., 2015; Lisle, 2008; Lisle et al., 1997, 2001; Sklar et al., 2009). At large spatial scales, the sediment pulse grain size distribution may fine downstream due to size-selective transport or attrition, especially when transport distances are long or particles are friable (Ashworth & Ferguson, 1989; Dingle et al., 2017; O'Connor et al., 2014; Paola et al., 1992; Parker, 1991). The gradual downstream progression of sediment pulse movement may be interrupted by sediment bottlenecks, which are locations in river networks with local deceases in transport capacity due to low channel slopes and/or wide channel widths (Czuba et al., 2017; Gran & Czuba, 2017; Schmitt et al., 2018).

The evolution of a sediment pulse is also dictated by pulse characteristics, streamflow

hydrology, and channel properties (Cui & Parker, 2005; Czuba et al., 2012a; Murphy et al., 2019; Sklar et al., 2009). River reaches with high slope or discharge relative to the bed surface grain size, i.e., high bedload transport capacity, can move sediment pulses quickly while reaches with low sediment-transport capacity and stream power are prone to sedimentation (Cui & Parker, 2005; Czuba et al., 2012a; Murphy et al., 2019). Bed texture response to a sediment pulse also depends on the grain-size of the preexisting bed, pulse size, pulse volume, and the spatial and temporal evolution of the pulse (Sklar et al., 2009). Sediment pulses with a grain size smaller than the preexisting bed move rapidly and thus, lead to a greater decrease in median bed material size, but for a shorter duration compared to a coarser sediment pulse undergoing more dispersion (Sklar et al., 2009). Large pulse volumes create longer lasting impacts on the channel bed with more dispersion compared to small-volume pulses (Czuba et al., 2012a; Sklar et al., 2009; Murphy et al., 2019). Sediment pulses are moved downstream more rapidly as the magnitude or frequency of streamflow increases (Czuba et al., 2012a). Thus, the interplay among sediment pulse characteristics of grain size, grain-size distribution, and volume along with channel and flow properties determine how the pulse evolves through a river network.

Along with flume experiments and model simulations with simple geometry, recent field studies describe how sediment pulses, particularly following dam removal, evolve over long reaches in actual rivers with downstream variations in bed sediment grain size, slope, and width (Cashman et al., 2021; East et al., 2015, 2018; Harrison et al., 2018; Major et al., 2012; Pace et al., 2017; Ritchie et al., 2018; Warrick et al., 2015). Following the removal of Simkins Dam on the Patapsco River in Maryland, Cashman et al. (2021) found weeks to months of translation and dispersion of the sediment pulse within in the channel, which aggraded the bed and affected local hydraulics. Dispersion and deposition on floodplains persisted for years. Following the removal of two dams on the Elwha River in Washington,

approximately 65% of the reservoir sediment was eroded, with 10% of this eroded sediment aggrading the channel up to 1 m in places (deeper in pools), and channel morphology changed from pool-riffle to braided (East et al., 2015, 2018; Ritchie et al., 2018; Warrick et al., 2015). Furthermore, most change occurred within the first two years following the dam removals (without any large flows) over the 20 km reach from the upstream-most dam to the coast. Following the removal of Marmot Dam on the Sandy River in Oregon, Major et al. (2012) found that sediment transport and deposition were strongly controlled by downstream changes in channel slope and valley morphology. Thus, variable transport capacity conditions present in the field strongly influence sediment pulse behavior. Such variability is rarely represented in network scale sediment routing models, which presents a potentially large gap in our ability to predict how such pulses may evolve during transport downstream through real river networks.

It is difficult to capture all the complex processes of sediment transport across a large-scale in a single modeling framework. There are one-dimensional models available that can be utilized to simulate sediment-pulse dynamics. The Unified Gravel-Sand (TUGS) model uses a surface-based bedload equation, with a sand and gravel transfer function, in linking grain-size distribution in the bed load, surface, and subsurface layer to simulate transport, erosion and deposition of sand and gravel (Cui, 2007). Specifically applied to dam removal pulses, the Dam Removal Express Assessment Models (DREAM) simulate aggradation and incision following dam removal for reservoir deposits composed primarily of non-cohesive sand and silt (DREAM-1) and gravel (DREAM-2; Cui et al., 2006a, b). The Morphodynamics and Sediment Tracers in one-dimension (MAST-1D) model also incorporates particle-size distributions to simulate morphodynamic evolution of a river bed and lateral exchange of sediment between the channel and floodplain (Lauer et al., 2016; Viparelli et al., 2013). The Lagrangian framework presented by Czuba (2018) and Pfeiffer et al. (2020) also uses

a surface-based bedload equation and considers mixed-size sediment transport. This model can be applied in gravel-bedded river networks as it is capable of incorporating additional complexities that arise from channel network structure. While these 1D models represent a promising avenue for study of sediment pulse dynamics, to date there are few examples of model application with field data over spatial scales of many kilometers (Castro-Bolinaga et al., 2020; Cui et al., 2014, 2019; De Rego et al., 2020).

We investigate the space-time evolution and downstream effects of simulated sediment pulses in the mainstem Nisqually River in Washington, USA. We simulate pulse behavior with downstream variations in slope, width, and bed-sediment grain size using a Lagrangian, bed-material sediment transport model (Czuba, 2018). Using this model, we explore how mixed-size sediment pulses, which are common in the field, affect downstream bed elevations, grain size, and sediment transport differently than uniform-sized sediment pulses, which have been commonly studied (as described above). We focus on sediment pulse volumes on the order of 10,000 m^3, typical of small dam removals and gravel augmentation (Arnaud et al., 2017; Bellmore et al., 2017; Foley et al., 2017; Major et al., 2017), which would be commonly encountered by river managers. Results of model simulations were compared to physical measurements, where available, to assess the efficacy of the model in predicting sediment transport and resulting changes. While we discuss limitations of our model in representing all the relevant complexities of the Nisqually River, we suggest that the model adequately represents an example gravel-bedded river, constrained in reality, and offers insight into how sediment pulses might move through real river systems. This study adds to our collective knowledge of how sediment supply perturbations, as discrete sediment pulses, may evolve in rivers and impact downstream locations.

3.3 STUDY AREA

Mount Rainier is a glaciated stratovolcano in the Cascade Range of western Washington with a summit elevation of approximately 4,393 m. The Nisqually River drains the southwestern slope of Mount Rainier and terminates in Puget Sound. This river system, and also the

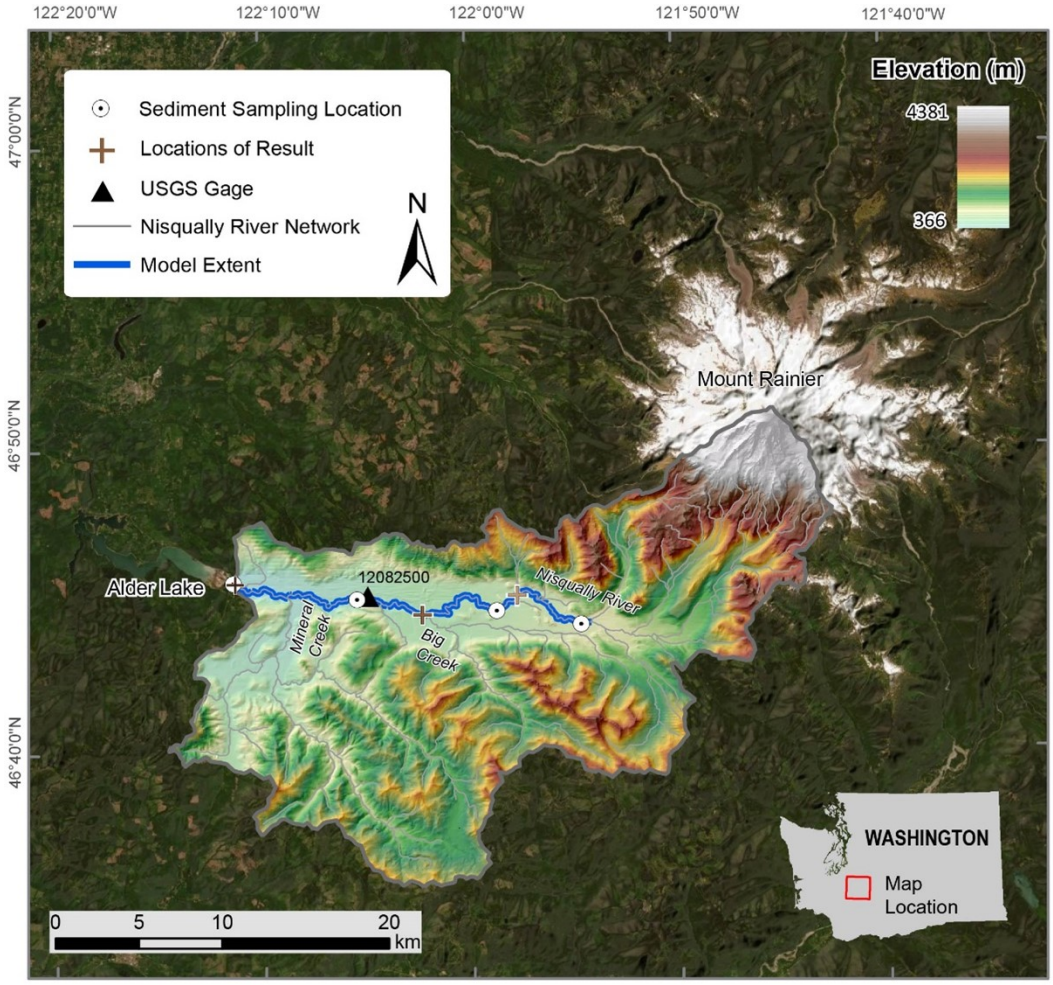

Figure 3.1: Study area map of the Nisqually River, Washington, USA. The USGS gage (black triangle) and locations of simulation results (brown plus signs) are marked within the modeled reach along with bed material sediment sampling locations (white circles).

White, Carbon, and Puyallup Rivers that drain Mount Rainier, receives large sediment loads

during large floods along with substantial debris flows (e.g., 40 million m^3 during a rainfall event in 1947) from Mount Rainier (Anderson & Pitlick, 2014; Czuba et al., 2012a; Legg et al., 2014). Large sediment loads delivered to these rivers contribute to river channel migration, bed aggradation, and subsequent reduction of flood-conveyance capacity (Czuba et al., 2010). The Nisqually River drains approximately 2000 km^2, but Alder Lake divides the river into an upper and lower section. Alder Lake is a reservoir, created behind Alder Dam in 1945, which reduces downstream sediment delivery (Czuba et al., 2012b). Herein, we focus on the upper Nisqually River draining Mount Rainier, which is most affected by large sediment supply. The upper Nisqually River (referred to as the Nisqually River hereafter) drains approximately 590 km^2 upstream of Alder Lake (Figure 3.1). Forest is the dominant land cover here and some upstream tributaries drain active glaciers. We apply our model here, because this is a reach commonly affected by large sediment pulse inputs and data are available to develop a model and assess the results (further described below).

3.4 METHODS

3.4.1 Model Framework and Development

3.4.1.1 Two-Layer River-Network Model

This work builds on a previous 1D Lagrangian, bed-material sediment transport model (Czuba, 2018), which we briefly summarize in this section. Here, sediment is conceptualized as a set of discrete individual parcels, where each parcel has a volume and grain size. The

river network is conceptualized as interconnected links, each with topologic (downstream connectivity), geometric (elevation, slope, channel segment length, average width), hydrodynamic (flow discharge), and bed sediment attributes (grain size distribution). Sediment in any link at any time is separated into two layers: active surface layer and inactive subsurface layer.

The maximum volume of sediment (χ) that can be moved in any link at any time is set by

$$\chi = \ell B L_a \tag{3.1}$$

where ℓ is the link length, B is the channel width, and L_a is the active layer thickness of that link. The total sediment parcel volume in any link at any time (V) is the sum of the volumes of all parcels within that link at that particular time. If the total sediment parcel volume in a link exceeds χ, then the excess sediment parcels are inactivated and placed into the subsurface layer, which consequently increases the slope of that link and decreases the slopes of any upstream links (Czuba et al., 2017).

The total sediment volume in the active surface layer of any link at any time (V_{act}) is dependent on χ as

$$V_{act} = \begin{cases} V, & V < \chi \\ \chi, & V \geq \chi \end{cases} \tag{3.2}$$

Each sediment parcel is tracked as it moves through the network. The arrival and departure of parcels from links follow a first-in, last-out rule, i.e., the most recent parcels to arrive in a link are positioned in the active surface layer, whereas the oldest parcels in

the link would be selected first for inactivation in the subsurface layer as described above. With this movement of sediment, bed elevation, and thereby slope, is updated accordingly (accounting for porosity) at each time step throughout the network. The transport time *(t)* of a sediment parcel to move through link length ℓ (Czuba & Foufoula-Georgiou, 2014; Czuba, 2018) is calculated as

$$t = \frac{\rho^{3/2} g R \ell L_a}{W^* \tau^{3/2} F} \tag{3.3}$$

where ρ is the density of water, g is the acceleration due to gravity, R is the submerged specific gravity of sediment, W^* is a dimensionless transport rate, τ is the bed shear stress, and F is a fraction describing the ratio of the parcel volume to the total sediment volume in the active surface layer, V_{act}, of that link at that time. The dimensionless transport rate, W^*, is calculated for each parcel and comes from the surface-based, mixed-size bedload transport equation of Wilcock & Crowe (2003). This formulation was chosen because it takes into consideration that the presence of sand increases the mobility of sediment.

The model requires flow data, channel/link data (segment length, width, initial elevation), and initial sediment data as inputs. The simulation procedure for every link at each time step can be summarized as:

(i) compute the maximum volume of sediment χ that can be moved (Equation 3.1),

(ii) compute bed elevations from sediment volume and update slope,

(iii) compute grain-size information of the active layer from all sediment parcels in the active layer for the Wilcock & Crowe (2003) equation,

(iv) compute transport time of each parcel (Equation 3.3), and

(v) update all parcel locations in their current link or move to a downstream link.

Thus, model outputs include spatially and temporally explicit characterization of sediment depth (accounting for porosity), bed elevation, grain size distribution, and volume in any link of the river network including fluxes past the downstream outlet. The Lagrangian nature of this formulation also allows specific sediment inputs to be tracked as they move through the river network.

3.4.1.2 Key Modeling Advancements

3.4.1.2.1 Initial median sediment size

The Nisqually River is gravel-bedded, and we are representing it as a single-thread channel whose median bed particle size varies systematically with local hydraulics. Specifically, the initial median bed particle size (D_{50}) was initialized throughout the network as a function of channel width (B) and slope (S) following a reduced form of the equation provided by Snyder et al. (2013) as

$$D_{50} = \frac{n^{3/5} Q_2^{3/5} S^{7/10}}{R \tau_c^* B^{3/5}} \tag{3.4}$$

where n is the Manning roughness coefficient, Q_2 is the 2-year recurrence interval flow, and $\tau_c{}^*$ is the critical Shields parameter to mobilize D_{50}. We implement Equation 3.4 using an assumed $\tau_c{}^*$ of 0.04 and n of 0.035, as in Snyder et al. (2013). Rather than validating these particular parameter values, we simply validate the resulting estimates of D_{50} with field measurements at several points along the study reach.

3.4.1.2.2 Flow depth

We consider river flows as hydraulically rough flows. Using the depth-average velocity, water depth in each link in the model is calculated as

$$H = \left(\frac{Q k_s^{1/6}}{8.1 B \sqrt{gS}} \right)^{3/5} \tag{3.5}$$

where k_s is an effective roughness height (later assigned as a function of bed grain size in section 3.4.2). This relation is approximated from Keulegan's resistance law for rough flow (Keulegan, 1938; Garcia, 2008) to incorporate grain-induced resistance in gravel-bed rivers. The formulation of Equation 3.5 allows water depth to change with variations in discharge (Q) and channel flow resistance (via k_s).

3.4.1.2.3 Upstream background sediment supply

Sediment can be supplied anywhere along any link within the network at any time step. We considered several different methods for supplying upstream background sediment to the model, each of which is described in the Appendix. The method that was the most numerically stable for this application and used throughout this study involved creating a sediment supply reservoir at the upstream end of the model. We did this by adding sediment parcels to the bed surface layer at the most upstream link in a sufficient volume as to not empty during the simulation. We also fixed the bed elevation at the upstream end of this link so that the added bed volume did not increase the channel slope. The streamflow continuously eroded this background sediment from this sediment supply link and transported it downstream.

3.4.2 Model Parameterization

This study modeled a 27.2 km reach of the mainstem Nisqually River discretized into 400-m long links, which is roughly twice the channel width, starting at Tahoma Creek (beginning of model stationing) and ending at Alder Lake (68 links total; Figure 3.1). We used the input channel geometry, streamflow, and sediment data from the model used by Czuba et al. (2012a). The channel geometry data included channel widths and bed elevations. The active channel, defined as the section of the river corridor relatively free of vegetation that conveys the majority of the water and sediment during high flow, was digitized from the 2009 National Agricultural Imagery Program (NAIP) imagery at 1:3000 scale (U.S. Department of Agriculture, 2011). A river centerline was then digitized through the center of the active channel, representing the dominant pathway of the river during high flow. Major tributaries include Big and Mineral Creeks (Figure 3.1). The active-channel width (Figure 3.2a) for each 400-m link was computed by dividing the total active-channel area for 400-m segments of the channel centerline by the length of that segment (400 m).

A longitudinal profile approximating the water-surface elevation was obtained by extracting lidar elevations of the river centerline. Elevation points were sampled from the underlying 1 m bare-Earth lidar data (PSLC, 2012) at 10-m increments along the river centerlines and averaged together every 400 m to determine an average elevation for that link. The final linear network in the model started just downstream of the confluence of the Nisqually River and Tahoma Creek, where the bed slope was roughly 2% (Figure 3.2a). A minimum slope of 0.1% was imposed for all links to account for any erroneously low-sloped sampling points.

A long-term streamflow record (water years 1946 – 2011) was compiled using time

series of daily streamflow (Figure 3.3a) from a USGS streamflow-gaging station (see location in Figure 3.1) on the Nisqually River (USGS 12082500, Nisqually River near National, WA; USGS, 2021). The streamflow data measured at this gage was scaled to upstream and downstream flow-change locations (Big and Mineral Creeks; Figure 3.1) using contributing drainage area. From the upstream end of the model to Big Creek (at 14.6 km), the gage discharge was decreased by 30%, and from Mineral Creek (at 23.6 km) to the downstream end of the model, the gage discharge was increased by 60%.

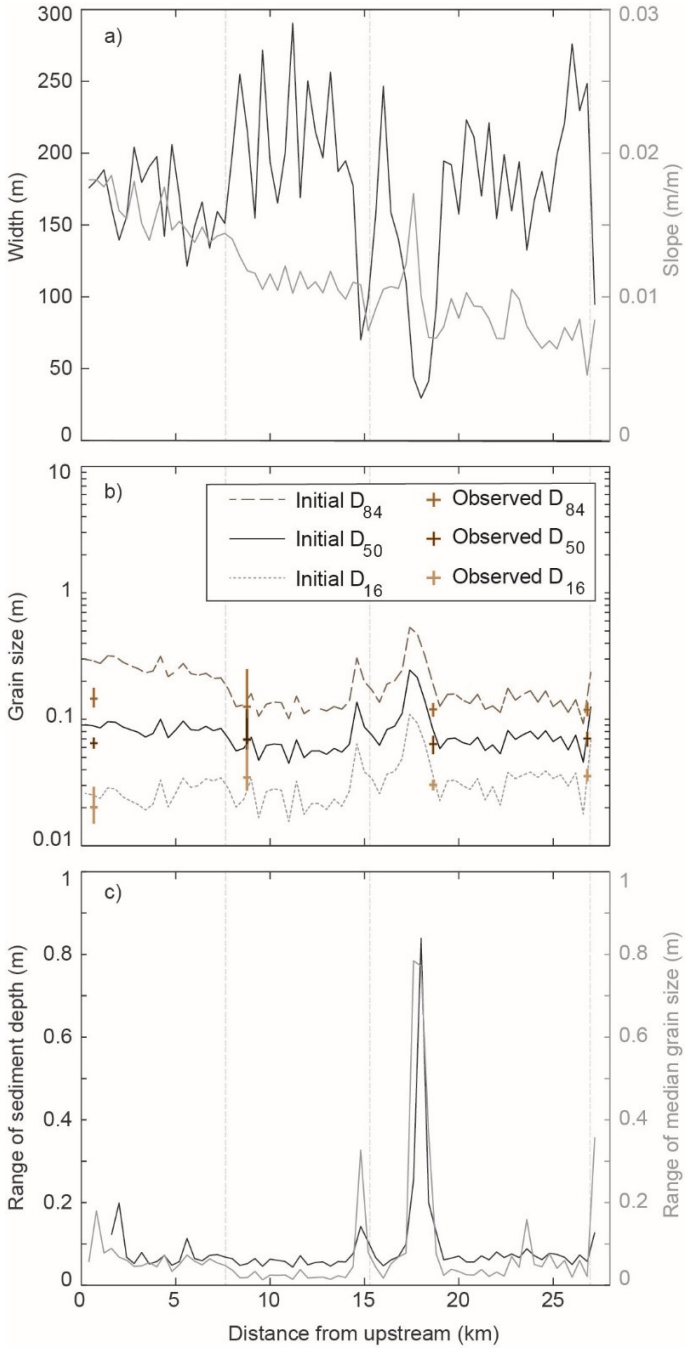

Figure 3.2: Fluvial geomorphic attributes along the mainstem Nisqually River. (a) Width and initial bed slope of the Nisqually River. (b) Observed (plus sign, where the vertical line of the plus represents the range) and modeled (solid and dashed lines) initial bed surface material grain size (excluding sand) from Equation 3.4. The observed D_{50} at roughly 9 km distance from upstream has a thicker symbol than the other observed grain sizes to show the extents of overlapping vertical lines. (c) Simulated range of sediment depth and median grain size (excluding sand) from 1946-2011. The three light gray vertical lines represent the locations where results are shown in Figure 3.3 (b, c).

All sediment parcels were assigned a maximum parcel volume of 50 m^3. Grain size of any parcel was given a discrete value among 0.4, 2.83, 5.66, 16.0, 45.3, 90.5, 181, 362, 724.1 and 1448.2 mm, which are the mean sizes for sand and of gravel (computed in log scale) within grain size bins bounded by 2, 4, 8, 32, 64, 128, 256, 512, 1024 and 2048 mm. There were four surface grain-size sampling locations (Figure 3.1; Czuba et al., 2012a), and multiple measurements were taken from gravel bars at each site using the Wolman pebble-count method (Wolman, 1954). These distributions had a median gravel size of roughly 70 mm and were composed of roughly 40% sand. The initial gravel distribution was approximated as log-normal with gravel sizes for each link calculated from Equation 3.4 (with Manning's n as 0.035 and τ_c^* as 0.04; Snyder et al., 2013) and standard deviation calculated from the observed distributions ($\sqrt{D_{84}/D_{16}}$ ~ 2-3 mm, Figure 3.2b; Garcia, 2008). This served as a close starting point for setting the initial bed sediment distribution that was further modified during a model conditioning run. In Figure 3.2b, the observed field measurements are shown as plus marks, the vertical lines of which extend to the range of the gravel size measurements and horizontal lines of the plus signs represent the median observed gravel size at that location. Due to the absence of subsurface data, it was initialized to be the same as the surface size distribution. Sediment load by grain size, was supplied to the model at the upstream boundary, and the determination of which was discussed in section 3.4.1.2.3.

The roughness height k_s (Equation 3.5) was assumed here as twice the median particle size (Garcia, 2008) and was updated at each time step in the model to translate flow discharge to flow depth. The active surface-layer thickness was selected as 0.25 m (close to D_{90}) throughout the model and bed sediment porosity was set as 0.25. Other specific parameter values were $\rho = 1000$ kg/m^3, $g = 9.81$ m/s^2, and $R = 1.65$.

The model was first run from 1 Oct. 1945 to 30 Sept. 2011 (water years 1946 – 2011)

for conditioning of input data. The model-conditioning process is a 1D river-morphodynamic adjustment process, which allows free or unconstrained parameters (e.g., bed sediment grain size distribution) to adjust to the fixed or constraining parameters in a way that allows the model to better simulate river processes given sparse topographic and sediment data (Cui et al., 2006a, 2006b; Cui & Wilcox, 2008; Lauer & Parker, 2008). The entire 65-year streamflow record was simulated and the model reached quasi-equilibrium after around 35 years, when the model simulated short-term fluctuations in bed elevation (mainly with flow fluctuations), but minimal long-term change. At the end of the model-conditioning process, the conditioned bed sediment grain size distribution was used at the start of all subsequent model simulations. Thus, only the bed sediment size distribution was updated while other inputs (e.g. slope, bed elevation etc.) were not updated following the model-conditioning process.

3.4.3 Model Verification

After model conditioning, the model was run again using daily streamflow data from water years 1946 – 2011. The simulated sediment depth and median grain size at three different locations are shown in Figures 3.3b, c. These locations are marked in Figure 3.1 (as brown plus signs): at an upstream location (7.6 km), in the middle of the reach (15.2 km), and at a downstream location near the basin outlet (26.8 km). The solid line in Figure 3.3d shows simulated bedload volume to Alder Lake. Changes is sediment depth, grain size, and volume were the greatest during high flows. The gradual decrease in equilibrium sediment depth ($\sim$3 cm over 65 years) in the baseline scenario simulated by the model suggests minor incision would occur during high flows given the minimal baseline sediment supply simulated.

Gradual coarsening of the median grain size suggests that this transport is mainly winnowing fine material. The model was only able to maintain a bed material composition at or below approximately 5% sand (much lower than the observed 40% on gravel bars). During the conditioning run, the model became stable when the bed material sand in excess of 5% was transported out of the model domain. The gravel bars from which the bed material was measured were very sandy, yet there was considerably less sand in the low-flow channel beds. We believe some of this discrepancy between our field observations and simulated sand fractions has to do with sorting and winnowing that occurs in the more complex field channel geometry than we are capturing in our essentially 1D model. We discuss this issue further in section 3.6.3 along with steps for potential model improvement. The abrupt changes in bed elevation during high flow events correspond to abrupt increases in simulated outlet volume. Figure 3.3c shows coarser bed material in the middle link compared to upstream and downstream locations, which is due to the initially coarser material at that location (middle light gray vertical line in Figure 3.2b). Results demonstrate relatively stable sediment characteristics with short-lived high flow fluctuations, while long-term trends in grain size and sediment depth were gradually adjusted primarily during high flow events.

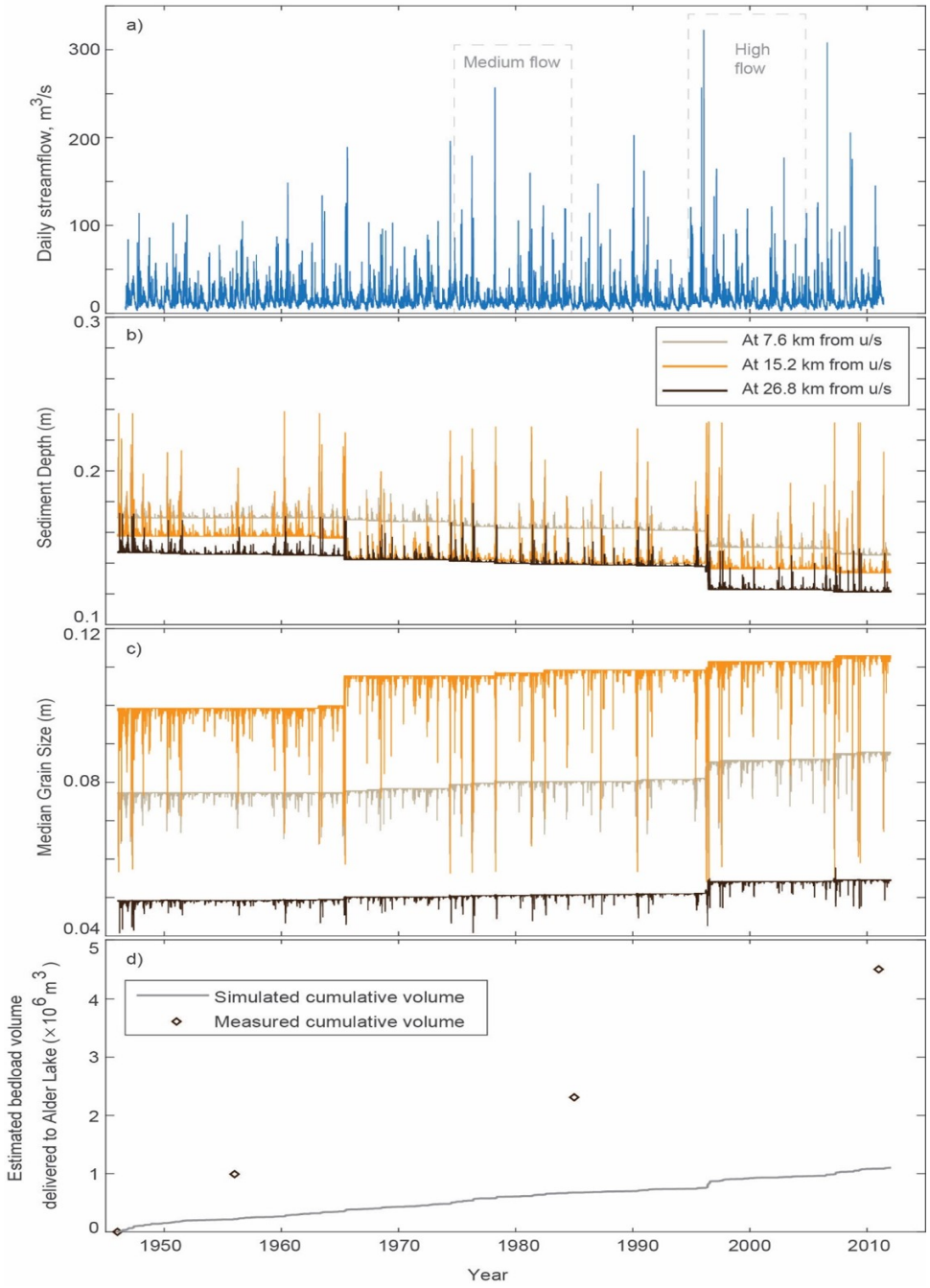

Figure 3.3: Time series of flow and sediment characteristics of three links and outlet. (a) Daily streamflow at the upstream end of the model. The high flow and medium flow periods (discussed in section 3.4.4) are shown in dashed rectangles. (b) Sediment depth and (c) median grain size in three links located in Figure 3.1 (brown plus signs). (d) Estimated (simulated and measured) bedload contribution to Alder Lake from 1946-2011.

We compared the model results to available measurements of bed grain size data, gage height fluctuations (at USGS 12082500, Nisqually River near National, WA), and deposition records in Alder Lake. We observed from Figure 3.2b that initial median gravel sizes (from Equation 3.4) exhibit strong agreement with median sizes of that collected at four locations in the network. Thus, this approach (via Snyder et al., 2013) allowed us to vary initial sediment size throughout the network as a function of channel geometry. The observed variance in bed elevations at the USGS gage location (at around 18 km) was ~1.5 m during 1985-2011 (Czuba et al., 2012a; Pfeiffer et al., 2019). The model predicted that bed elevations varied 0.9 m (peak of sediment depth in Figure 3.2c) from equilibrium during this same period. However, this was under a simulated background sediment supply that was transporting at-capacity, thus, not including sediment pulses that likely contributed to real variations observed in the gage data (Anderson & Pitlick, 2014; Legg et al., 2014). There were 48 debris-flow events recorded between 1926 and 2006 in tributaries of the Nisqually River within Mount Rainier, 28 of which occurred between 1967 and 2006 (Copeland, 2009; Walder & Driedger, 1993, 1994). We also know that a heavy rainfall event in 1947 alone delivered about 40 million cubic meters of sediment to a Nisqually River tributary (Crandell, 1971). Estimating bedload transport only, the model underpredicted the delta volume in Alder Lake (Czuba et al., 2012b) by approximately 4-fold (Figure 3.3d). In the White River (a comparable river draining Mount Rainier), the bedload contribution to the total load was low (around 11%; Czuba et al., 2012a), and most of the material in transport was in suspension (Czuba et al., 2012a). We used this percentage (11%) to convert the total volume of sediment accumulated in Alder Lake to an estimated fraction that was delivered by bedload (Figure 3.3d). We did not include fine suspended material in our simulation and could not adequately simulate the total amount of sand transported in this system. Given potential changes in delta depositional porosity and incomplete sediment input records (e.g., 48 debris-flow events not included), we fully expect our simulations to underestimate both

bed elevation changes and outlet volumes. For instance, even if only a small fraction of the 40 million cubic meters of sediment deposited in a Nisqually River tributary from a single debris flow event in 1947 (Crandell, 1971) eroded over time to deliver 3 million cubic meters of sediment to Alder Lake as bedload, this would make up for the underestimation in the model simulation. Altogether, these factors likely contributed to the low predictions of bed elevation fluctuations and volume delivered to Alder Lake as compared to observations of deposition in the delta of Alder Lake. However, we do think the model adequately represents an example gravel-bedded river, constrained in reality, and should offer insight into how sediment pulses might move through real river systems.

3.4.4 Model Simulations and Analysis Metrics

Model simulations investigated the spatial and temporal evolution and downstream effect of uniform-sized and mixed sediment pulses in a river with downstream variations in slope, width, and bed-sediment grain size. Model simulations included combinations of two hydrologic conditions, two sediment-pulse volumes, two sediment-pulse distribution types, and three sediment-pulse grain sizes. We constructed seven comparative analyses (See Table 3.1 in Section 3.5.1), from which three comparisons between uniform-sized and mixed sediment pulses are detailed in Section 3.5.2 (others are in Appendix). The set of model simulations varied hydrologic conditions (repeating 10-year periods for 30 years of daily streamflow for high (WY 1995-2004; highest two peak flows = 322 m^3/s and 257 m^3/s) and medium (WY 1975-1984; highest two peak flows = 257 m^3/s and 179 m^3/s) streamflow hydrology; see Figure 3.3a), sediment-pulse volume (reported as a depth; 0.4 m and 1.1 m supplied to the upstream-most link of the network), sediment-pulse distribution type (uniform-sized gravel

and mixed distribution), and sediment-pulse median grain size (10 mm, 30 mm and 70 mm; recall that the median gravel size of the bed was approximately 70 mm, so these pulse grain sizes are roughly 0.15, 0.5, and 1.0 times the median bed gravel size). Sediment-pulse depths (0.4 m and 1.1 m) were converted from sediment-pulse volumes (of roughly 19,000 m^3 and 57,000 m^3, respectively) by dividing by the average link length and width, and accounting for porosity. That is, if the pulses of above-mentioned volumes were emplaced in a single link of average width, these pulses would aggrade the bed (or increase the sediment depth) by 0.4 and 1.1 m, respectively. Thus, sediment-pulse depths represent pulses of different sediment volumes. These pulse volumes are roughly one and three times, respectively, the transport capacity volumes, χ, of the most upstream link. Additionally, these pulse volumes are representative of inputs from most dam removals (94% of removed dams impounded less than 10,000 m^3 of sediment; Bellmore et al., 2017; Foley et al., 2017; Major et al., 2017) and also from gravel augmentation (23,000 m^3 of sediment; Arnaud et al., 2017). The mixed-type sediment distribution was constructed assuming a log-normal sediment distribution with the specified median gravel size and standard deviation from field measurements, and then incorporating 5% sand fraction (estimated from the conditioning run). For each hydrologic condition, the simulation results of a baseline condition (without a sediment pulse) were subtracted from a sediment-pulse condition (with different pulse volumes, distribution types, and grain sizes) to isolate the morphodynamic response due to the individual sediment pulse. Each individual sediment pulse was added in total, instantaneously to the model at the beginning of the model run (time t = 0) and at the second link from the upstream end (to avoid adding the pulse in the background sediment supply link).

The metrics we used to describe the downstream effect of a sediment pulse were the maximum change in bed elevation and median bed-surface gravel size, timing of maximum accumulation, and average change in post-pulse sediment depth. We compared the maximum

changes and timing of maximum changes with different pulse arrival times. The arrival time of 50% of the pulse at a location is the time when half of a pulse's volume has been transported past that location. We were able to calculate this metric, because the Lagrangian model used allows us to "tag" the pulse sediment parcels and know where they are located at any given time. Similarly, an arrival time of 10% and 90% of the pulse at a location are the times when one-tenth and nine-tenths of the pulse volume had transported past that location, respectively. The spread of timing, as defined for this study, is the difference in the arrival times of 90% and 10% of the sediment pulse by volume. If the simulated flows did not transport 90% of the pulse volume through a stated location (e.g., the outlet) by the end of the simulation, then the spread of timing was calculated by subtracting the pulse arrival time for the 10% volume from the duration of the simulation (i.e., 30 years). The average change in post-pulse sediment depth was calculated as the time-averaged change of sediment depth from the baseline condition after the peak bed-elevation change due to the pulse had passed each location. Normalized change in simulated outlet volume was found by dividing the change in outlet volume from the baseline condition by the input pulse volume.

3.5 RESULTS

3.5.1 Overview of Pulse Dynamics and Movement

Nine sediment pulse runs were conducted to examine the impacts of median pulse grain size, volume (converted to a depth), and distribution type (uniform and mixed) along with two baseline runs (without pulse) under medium and high flow conditions. These simulations

resulted in a total of seven comparisons, which are listed in Table 3.1. We also highlight the key findings of each comparison, the details of which are discussed in the following sections and in the Appendix. We only present detailed comparisons between the uniform-sized and mixed pulses in the next section because these represent the most novel results. The other comparisons, which have been explored in previous literature, are detailed in the Appendix.

Table 3.1: Summary of the comparisons of model simulation results. * indicates that these findings can be found in the Appendix.

Difference in:	**Flow**	**Pulse depth (m)**	**Median pulse grain size (mm)**	**Highlight**
Median Gravel Size of Pulse	Medium	0.4	10	Finer pulse travels faster and causes more incision, while coarser pulse travels slower and causes more aggradation (especially at wider reaches with low slope).*
	Medium	0.4	30	
	High	0.4	30	Coarse pulse travels slower and leaves greater post-pulse incision. Complex pattern of bed-elevation change at intersection of pulse size, channel characteristics, and hydrology.*
	High	0.4	70	
Pulse Volume (Depth)	Medium	0.4	30	Nearly similar bed-elevation change for both pulse depths. Smaller volume took longer to move through system, likely due to more fully mixing with the bed material.*
	Medium	1.1	30	
Flow	Medium	0.4	30	Pulse travels faster during high flow. Pattern of bed-elevation change highly variable.*
	High	0.4	30	
Pulse Distribution Type	Medium	0.4	10	Arrival time of 50% of pulse is the same, but coarse tail of mixed pulse moves slower. Bed-elevation change (primarily incision) is greater for the uniform pulse. (section 3.5.2.1)
	Medium	0.4	10 (Mixed)	
	Medium	0.4	30	Arrival time of 50% of pulse is the same, but coarse tail of mixed pulse moves slower. Pattern of bed-elevation change highly variable. (section 3.5.2.2)
	Medium	0.4	30 (Mixed)	
	Medium	1.1	70	Mixed pulse dispersed slowly without a defined pulse manifestation. (section 3.5.2.3)
	Medium	1.1	70 (Mixed)	

Before describing the details of the runs and comparisons with differences in pulse distribution type, we provide an overview of simulated pulse movement as the fraction of the pulse that remains in the mainstem of the Nisqually River under different conditions (Figure 3.4). Compared with uniform pulses, mixed pulses moved more slowly through the system and were not completely delivered to the outlet by the end of the 30-year simulation (Figure 3.4; markers with an "×"). For example, under medium flow and for a 10-mm uniform pulse

(filled green square marker), 100% of the pulse traveled through the network within the first 2 years. But for a mixed pulse with a D_{50} of 10 mm, only 70% of the pulse traveled through the network within 2 years and 83% of it reached the outlet within 30 years. For 70-mm pulses (orange square marker), the mixed pulse was transported slowly (71% reached the outlet after 30 years), whereas all of the uniform pulses traveled through the network within 14 years. For 30-mm pulses (filled blue square marker), 90% of the uniform pulse and 74% of the mixed pulse traveled through the network after 30 years. However, the larger volume uniform pulse (hollow blue square marker) traveled more rapidly than the smaller pulse volume of either uniform or mixed grains (filled blue square markers) under medium flows; the smaller volume pulse was likely mixing more with the bed material than larger volume pulses (discussed further in Appendix S3). High flows (filled blue circular markers) transported the pulse much quicker compared to medium flows – 97% within 2 years and 100% within 12 years. When high flows act on the system with a 90-mm pulse (filled orange circular markers), model simulations indicate 53% of the uniform pulse travels to the outlet within 2 years and 100% of it within 12 years. Thus, movement of sediment pulses through this reach depends on the dynamics of size, volume, distribution type, and flow condition, which we describe further in subsequent subsections and in the Appendix.

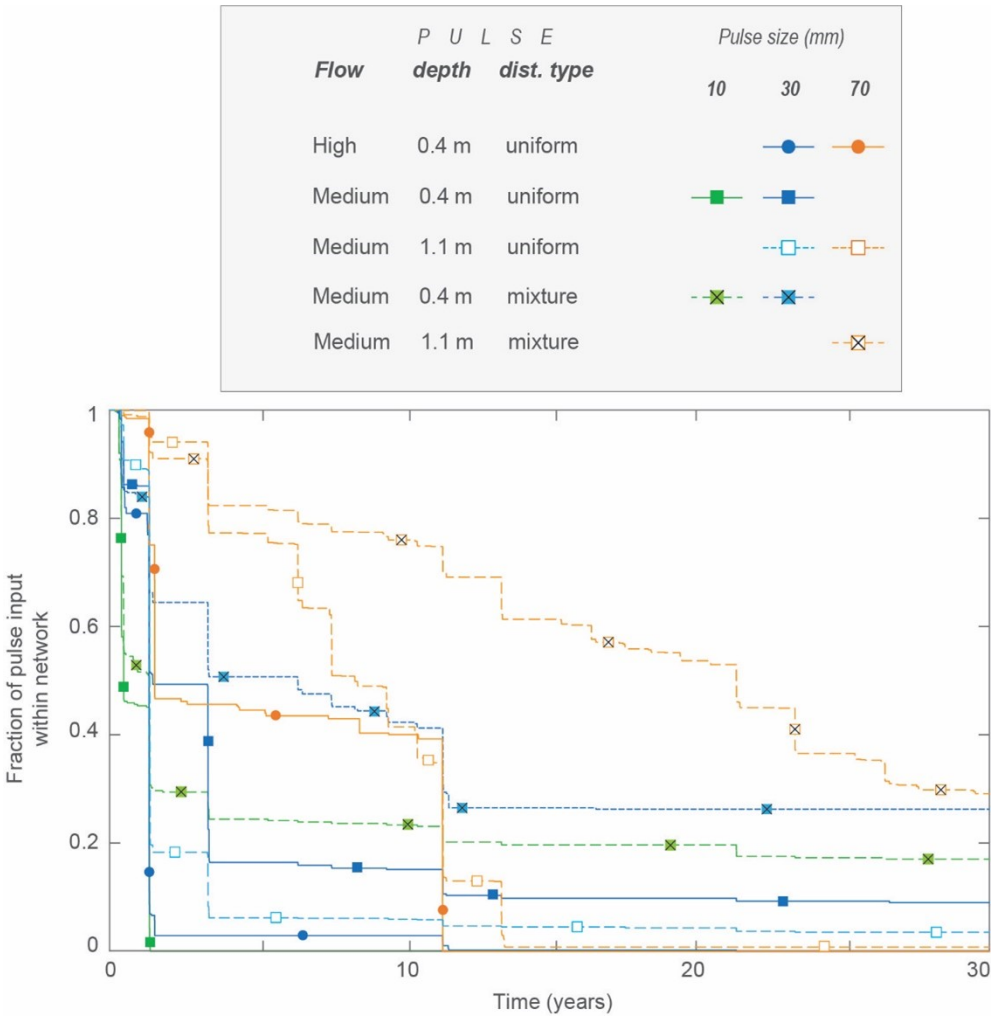

Figure 3.4: Movement of sediment pulses of different size (10, 30, and 70 mm), distribution type (uniform and mixed), and volume (0.4 m and 1.1 m depth) through the mainstem Nisqually River under high and medium flow conditions.

3.5.2 Comparison of Changes from Different Pulse Grain-Size Distributions

In this application, we systematically found that changes in median gravel size were inversely related to the changes in sediment depth (i.e., bed aggradation occurred with bed fining and

bed incision occurred with bed coarsening; see Appendix S2). Thus, from here on, we narrow down our analysis to sediment depth only, in order to simplify the comparisons.

3.5.2.1 Uniform and mixed 10 mm pulse

Changes in sediment depth from baseline (without pulse) are shown for uniform and mixed type pulses of 10 mm and 0.4 m depth under the medium flow condition (Figures 3.5a, b; and Figures 3.5e, f zoom in on Figures 3.5a, b, respectively). These model results show systemic initial incision (light brown colors generally before 1.2 years, Figures 3.5a, b), likely because the pulse is cutting off the background sediment supply that would have otherwise made it downstream. Then the pulse moves through the network, fairly coherently between 1.2 and 1.5 years (straight sloped dark blue lines in Figures 3.5e, f). This is the pulse itself causing aggradation and as a result of that pulse passing through (after 1.5 years), the bed sediment was mixed and mobilized in a way that results in longer term (but slight) incision (brown areas that dominate Figures 3.5a, b) compared to baseline. This pre-pulse incision and pulse aggradation were commonly observed in all of the following simulations as well. If we take horizontal slices through the zoomed space-time contours (e.g., dashed horizontal brown lines in Figures 3.5e, f at different times), we can see the location of the pulse along the model domain (Figures 3.5g, h).

To evaluate the dynamics more closely, we selected an example upstream reach (having approximately average width) at 7.6 km (brown dotted verticals in Figures 3.5a, b and plus sign in Figure 3.1). For both grain size distributions, the core of the pulse is marked in Figure 3.5d, before which (pre-pulse) the pulse reduces the baseline sediment supply.

Maximum change from baseline is slightly higher for the uniform pulse (Figure 3.5d). The flow hydrograph is included as well to highlight that most fluctuations in bed sediment occur at high flow events. The timing of these impacts is, however, different, which is related to pulse arrival time. Pulse arrival time again depends on the dynamics of the flow and pulse size.

Post-pulse change (after 1.5 years, Figures 3.5a, b) results in mostly incision (from baseline condition), which is greater for the uniform pulse, except for some aggradation in a low slope reach at 15.2 km. After passing through the narrow reaches (18 km), both pulses have little impact on the bed farther downstream. At location 7.6 km after 1.5 years, the mixing and mobilizing of the bed sediment results in slight long-term incision, and this incision is marginally greater with the mixed pulse than the uniform pulse (Figure 3.5d). Model results showed that 70% of the pulse arrives at the outlet at around 1.5 years for both the uniform and mixed pulse (Figure 3.4). However, the total pulse volume arrives within 2 years for the uniform pulse, while only 83% of the mixed pulse leaves the system by the end of the 30-year simulation period.

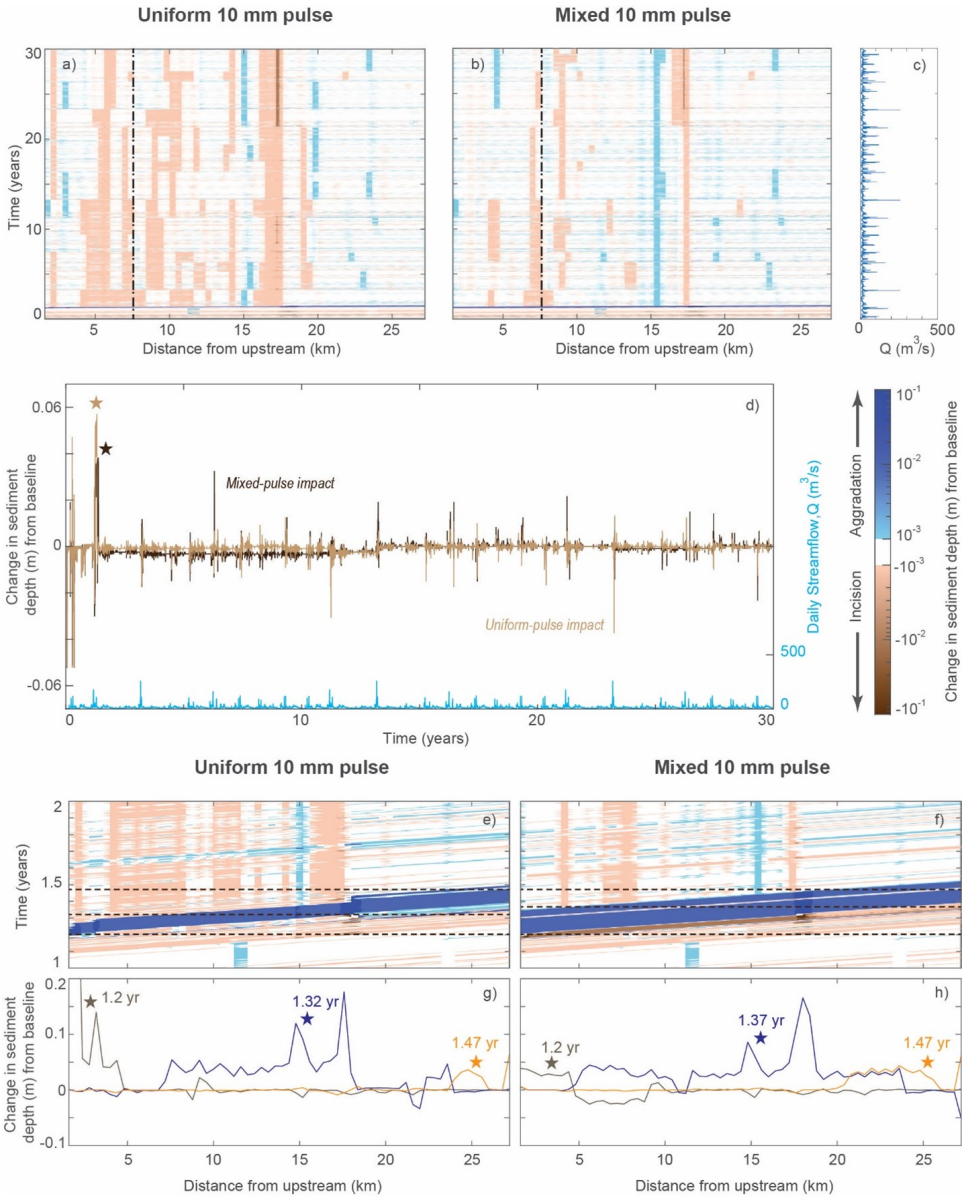

Figure 3.5: Comparison of the bed-elevation changes from uniform and mixed pulse of 10 mm median gravel size of 0.4 m depth for the medium flow condition. (a, b) Space-time contours of change in sediment depth from baseline due to uniform and mixed pulse. (c) Daily discharge at the upstream end of the model in medium flow condition. (d) Temporal changes in sediment depth from baseline at 7.6 km (location shown as dashed lines in (a) and (b)) due to uniform and mixed pulse. The star indicates the location of the pulse. (e, f) Space-time contours of change in sediment depth zoomed in on years 1-2 from (a) and (b), respectively. The narrow range in the y-axis helps to discern the movement of the pulse downstream. (g, h) Spatial changes in sediment depth from baseline at different times (horizontal dashed brown lines in (e, f)) also show the propagation of the pulse (indicated by star).

3.5.2.2 Uniform and mixed 30 mm pulse

Changes in sediment depth from baseline are shown for uniform and mixed type pulses of 30 mm and 0.4 m depth under medium flow condition (Figures 3.6a, b). Post-pulse change (after 3.5 years for the uniform pulse and at 11.5 years for the mixed pulse) results in mostly aggradation due to the uniform pulse (except in steep upstream reaches) and incision due to the mixed pulse (only up until 18.4 km; downstream of this narrow reach, there is aggradation in low sloped reaches). At location 7.6 km, there is post-pulse aggradation for the uniform pulse and incision for the mixed pulse (Figure 3.6d). Model results showed that 70% of the uniform pulse arrives at the outlet at 3.5 years and at 11.5 years for the mixed pulse (Figure 3.4). After the 30-year simulation, 75% of the mixed pulse and 90% of the uniform pulse was delivered to the outlet (Figure 3.4).

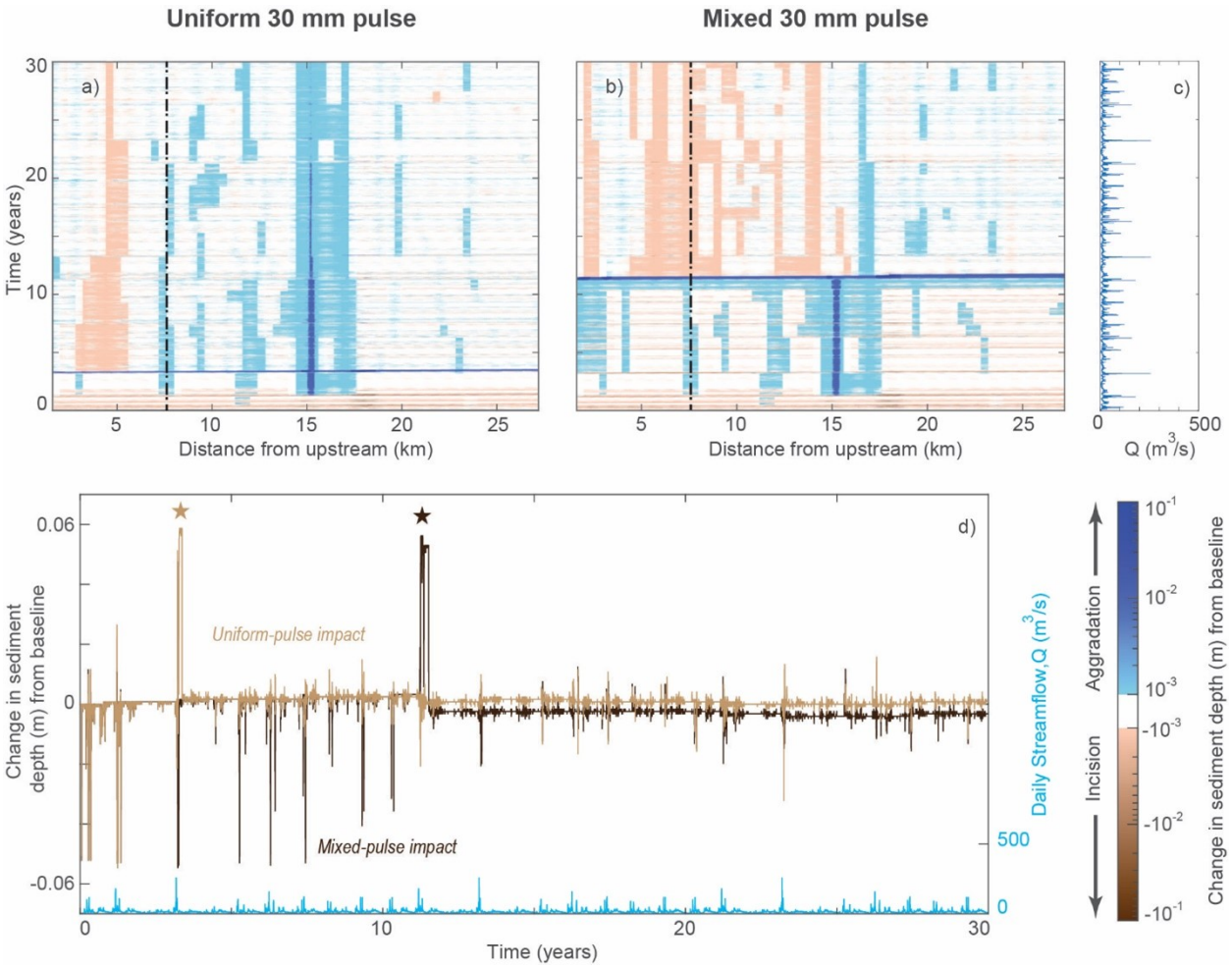

Figure 3.6: Comparison of the bed-elevation changes from uniform and mixed pulse of 30 mm median gravel size of 0.4 m depth for the medium flow condition. (a, b) Space-time contours of change in sediment depth from baseline due to uniform and mixed pulse. (c) Daily discharge at the upstream end of the model in medium flow condition. (d) Temporal changes in sediment depth from baseline at 7.6 km (location shown as dashed lines in (a) and (b)) due to uniform and mixed pulse, where the star indicates the location of the pulse.

3.5.2.3 Uniform and mixed 70 mm pulse

Changes in sediment depth from baseline were evaluated for uniform and mixed type pulses of 70 mm and 1.1 m depth under medium flow condition (Figure 3.7). Initial pre-pulse incision

is dominant in both cases (bottom brown nearly straight lines, Figures 3.7a, b; negative fluctuations, Figure 3.7d). The incision continues for the uniform pulse (except in low slope reaches) until the pulse itself arrives downstream and aggrades the bed at around 13.5 years (Figure 3.7a). As it propagated downstream, the uniform pulse aggraded low slope reaches and incised steep upstream reaches (Figure 3.7a). In contrast, the 70 mm mixed pulse responded differently with no apparent peak in aggradation (Figures 3.7b, d). Recall, the 70 mm mixed pulse grain size distribution closely resembles the existing bed, so this pulse was expected to disperse slowly without a major mode of translation (Cui & Parker, 2005; Lisle et al., 1997, 2001; Sklar et al., 2009). What we observed was a more diffuse impact (Figure 3.7b), with some accumulation in lower-sloped reaches and bed-elevation fluctuations at flow peaks. Figure 3.4 shows that 70% of the uniform pulse arrived at the outlet at 11.5 years and at 28 years for the mixed pulse. These results do not show any marked pulse aggradation at 7.6 km due to the mixed pulse, but rather only show accumulation of the uniform pulse (at around 13.5 years, Figure 3.7d).

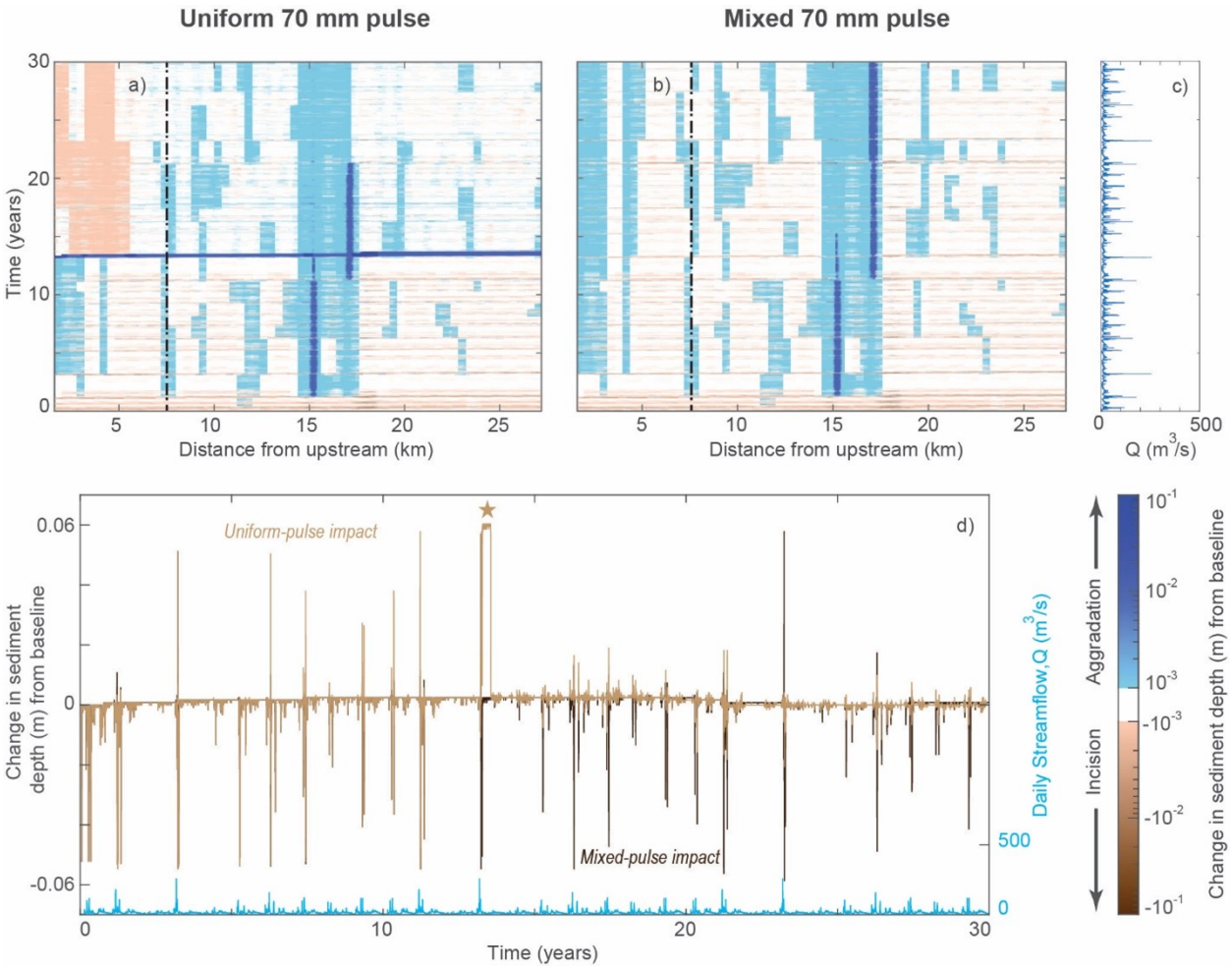

Figure 3.7: Comparison of the bed-elevation changes from uniform and mixed pulse with 70 mm median gravel size of 1.1 m depth for the medium flow condition. (a, b) Space-time contours of change in sediment depth from baseline due to uniform and mixed pulse. (c) Daily discharge at the upstream end of the model in medium flow condition. (d) Temporal changes in sediment depth from baseline at 7.6 km (location shown as dashed lines in (a) and (b)) due to uniform and mixed pulse, where the star indicates the location of the pulse.

3.5.3 Summary of Pulse Impact

The results above (sections 3.5.1-3.5.2, and in the Appendix) showed the dynamic relation among pulse grain size, distribution type, and volume (depth) and streamflow hydrology.

Here, we summarize the maximum accumulation of the pulse, the spread of timing (difference between arrival time of 90% versus 10% of the pulse), and arrival time of 50% of the pulse for all simulations at location 26.8 km (brown plus sign, Figure 3.1). We also present the average post-pulse impact (i.e., time-averaged change of sediment depth from baseline after pulse has passed a given location) for different sediment pulses along the river.

There are discernible patterns in the plot of 50% arrival time of the pulse versus the magnitude of change in sediment depth (Figure 3.8a). The cluster of points around 2.5 cm pulse accumulation and low arrival timing might be limited by how the pulse spreads out over the reach geometry (Figure 3.8a). We see that the maximum pulse accumulations are greater for high flows (filled circles). For mixed pulses, we found that the finest gravel size (10 mm; roughly 0.15 of median bed gravel size) and coarsest gravel size (70 mm; roughly the same size as median bed gravel size) have the lowest pulse accumulations, even though the 10 mm pulse travels quickly and the 70 mm pulse disperses slowly. However, the mixed pulse with intermediate gravel size (30 mm; roughly 0.5 of the median bed gravel size) causes the greatest accumulation and has an intermediate arrival time compared to the other mixed pulses. This suggests that this intermediate size (roughly 0.5 of the median bed gravel size) is likely to have the largest downstream impact over the timescales studied here because finer sizes move through quickly and without significant alteration of the bed and coarser sizes disperse over timescales much longer than the 30-year simulations conducted here.

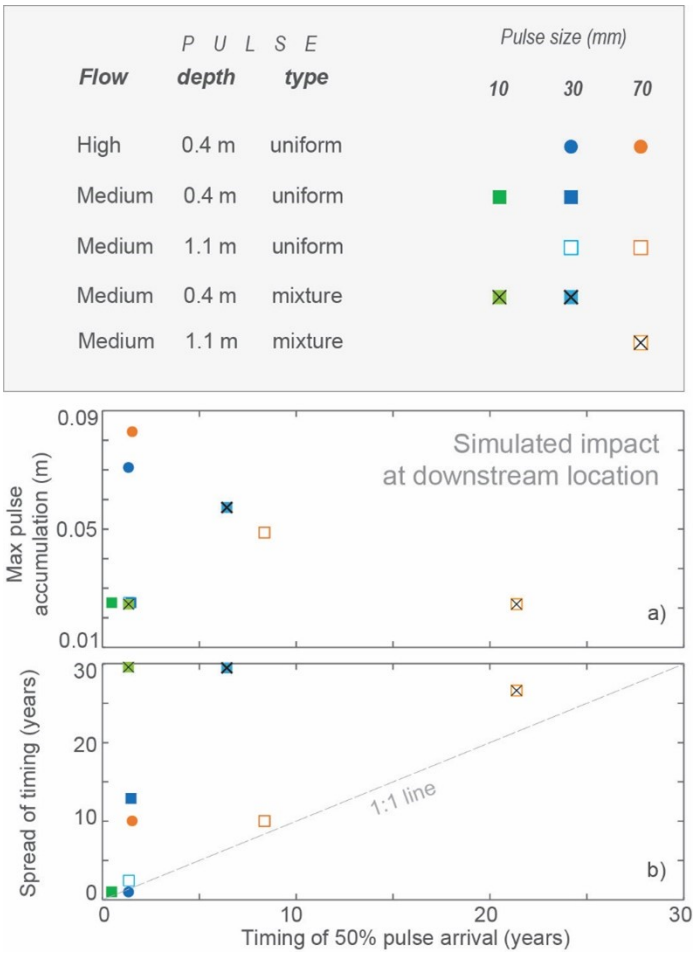

Figure 3.8: Simulated pulse impacts at downstream location (26.8 km; brown plus sign in Figure 3.1). (a) Maximum accumulation due to pulse and (b) spread of timing (difference in arrival time of 90% and 10% of the pulse) are plotted against the arrival time of 50% of the pulse.

We find that, in general, arrival time increases with pulse grain size and mixed pulses spread out more in timing than uniform pulses (Figure 3.8b). For many of our simulated pulses with an appreciable spread in timing, we found that the arrival time distribution had a positive skewness (Figure 3.4), attributed to either the pulse mixing with the preexisting bed or a coarser tail that travels more slowly. For nearly every simulation (except the 30 mm pulse under high flow), the arrival time of the center of the pulse was of a shorter duration than that of the spread of timing (Figure 3.8b). For pulses with a long spread in timing,

we found that timing of maximum change in bed elevation does not necessarily correspond to the timing of 50% pulse arrival (Figures 3.5d-3.7d). The contour plots of Figures 3.5-3.7 also showed that there was little difference in timing of the changes from upstream to downstream (because the brown and blue lines were nearly horizontal). This indicates that most of the pulses we have simulated were translation-dominated pulses for the mainstem of the Nisqually River (with the exception of the 70 mm mixed pulse, Figure 3.7). As our sediment pulses were mostly finer than the pre-pulse bed grain sizes, this translational behavior was expected (Sklar et al., 2009).

We present the time-averaged change in sediment depth from the baseline condition after the passage of the pulse through each location to summarize the complex post-pulse impact spatially (Figure 3.9). We also replot the river width and slope, and divide the network into distinct reaches to aid in interpretation. We qualitatively characterize 5 reaches: high slope-medium width, medium slope-high width, medium slope-low width, low slope-medium width, and low slope-high width (ordered from upstream to downstream). The flow change locations are at 14.4 km and 23.6 km (light blue vertical dashed lines, Figure 3.9). The resulting average changes were greater for high flow compared to medium flow (solid dark blue and orange lines, Figure 3.9). The smallest pulse grain size (10 mm) caused average incision in high to medium slope and medium to low width reaches (centered at 5.2 and 17.6 km, respectively; solid and dashed green lines in Figure 3.9). Overall, post-pulse aggradation occurred where the channels widen (i.e., at transition locations at 8 and 23.6 km in Figure 3.9) due to a decrease in transport capacity (Czuba et al., 2012a; Czuba et al., 2017; Gran & Czuba, 2017). This result highlights how the natural complexity of river structure (spatial distribution of channel width and slope) plays an important role in any resulting aggradation or incision that occurs at any location due to propagation of a sediment pulse.

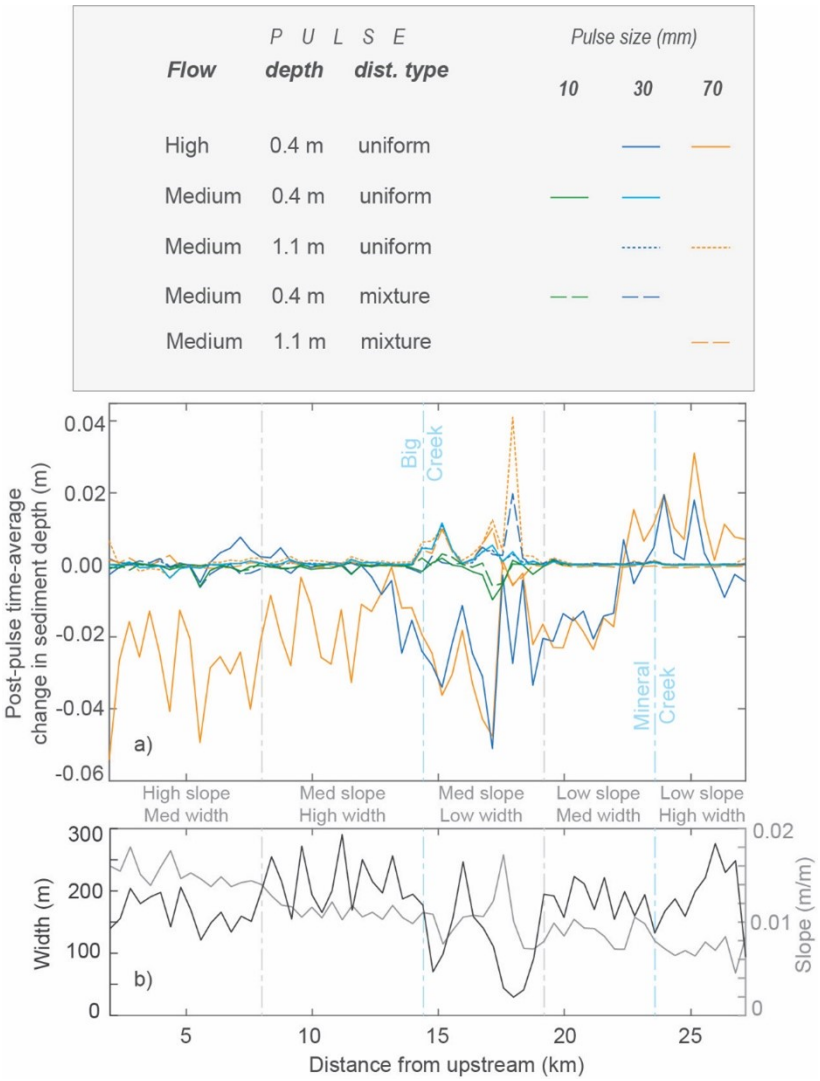

Figure 3.9: Simulated post-pulse time-average change in sediment depth (time-averaged change in sediment depth from the baseline condition after the pulse has passed each location) throughout the river network (a), along with variation in width and slope (b). The vertical dashed lines divide the network into 5 reaches; the light blue ones among them also indicate the locations of tributaries (Big Creek and Mineral Creek, in Figure 3.1).

We compared simulated outlet volumes after the 30-year simulation period for all model runs (Figure 3.10b) to see how much bed sediment was mobilized and delivered to the outlet due to the pulse introduction. The change in outlet volume from the baseline condition (without pulse) was divided by the input pulse volume to normalize the results (Figure

3.10a). A normalized value greater than one indicates that an additional volume greater than the added pulse passed the outlet compared to the baseline simulation and highlights that the added pulse increased bed mobility. All pulses under the high flow condition and the 10- and 30-mm mixed pulses increased the mobility of the bed sediment (i.e., an amount of sediment greater than the sediment pulse addition was delivered to the outlet; Figures 3.10a, b). The large volume (1.1 m) uniform pulse runs delivered nearly the same amount of sediment that was added (Figures 3.10a, b). Simulations of the 10- and 30-mm pulses of small volume (0.4 m) with medium flow condition and the 70 mm mixed distribution pulse delivered less sediment to the outlet compared to baseline (Figures 3.10a, b). For these small volume uniform pulses, this was likely due to a reduced delivery of background sediment because of the presence of the pulse. For the 70 mm mixed distribution pulse, this was because most of that sediment did not arrive to the outlet in the 30-year simulation period. The uniform pulses alone do not appear to greatly mobilize bed sediment, because they cover the existing bed in a nearly uniform grain size that decreases mobility in the Wilcock & Crowe (2003) equations. Whereas the finer mixed pulses add a range of finer sizes to the bed grain size distribution and that together increases the mobility of the larger sizes without completely blanketing them in a uniform size range of finer sediment.

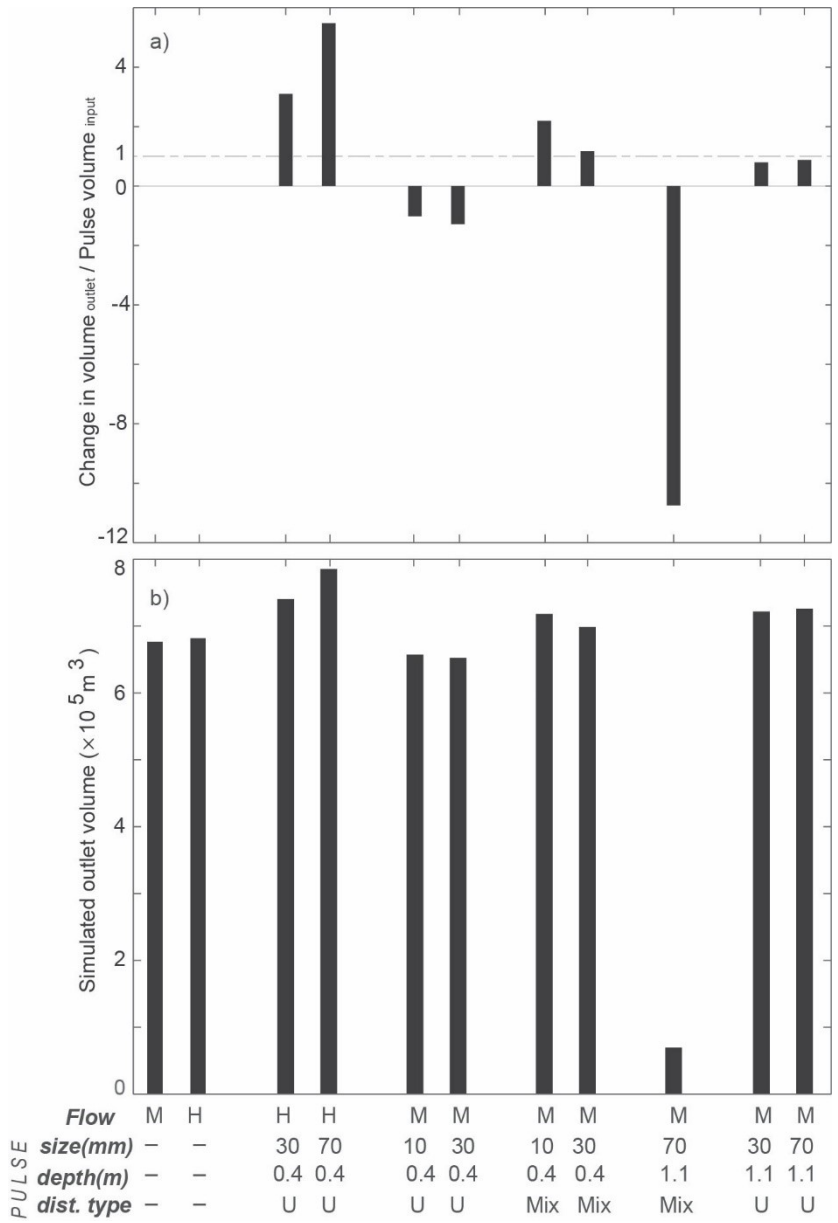

Figure 3.10: Simulated outlet volume for pulses of different size (10, 30 and 70 mm), depth (0.4 and 1.1 m), and distribution type (U and Mix, i.e., Uniform and Mixture) under medium and high flow (M and H) condition after the 30-year simulation period. (a) The change in outlet volume from baseline normalized by the input pulse volume. That is, a value of one would indicate that an additional volume equivalent to the added pulse passed the outlet compared to the baseline simulation. (b) The total outlet volume, where the first two columns are baseline conditions for medium and high flow scenarios.

3.6 DISCUSSION

3.6.1 Corroboration of Simulation Results with Previous Findings

Sediment pulses mix with bed sediment and affect bed-sediment composition and mobility in nonlinear ways (Humphries et al., 2012; Sklar et al., 2009; Venditti et al., 2010a, 2010b; Wooster et al., 2008). In general, our model results corroborated previous findings. Once emplaced, our model results showed that in all scenarios (Figures 3.5-3.7, Appendix S3) an initial pre-pulse incision occurs followed by sediment accumulation when the pulse arrives, consistent with Sklar et al. (2009). Post-pulse changes are more complex as they depend on nonlinear feedbacks among streamflow hydrology, channel structure, and mixing of pulse and bed sediment. We found that the maximum accumulation at any location occurred as a result of the pulse sediment, and after the passage of the pulse, the magnitude of changes in sediment depth was consistently small. General spatiotemporal patterns of long-term change in sediment depth suggest that sediment pulses tend to deposit in the wider and lower slope reaches (blue regions of the contour plots, Figures 3.5-3.7). Wider reaches, as well as reaches of transitional width (e.g., from a narrow to a wide channel), experience more average aggradation after the pulse has passed the reach compared to reaches with small to medium widths (Figure 3.9; Czuba et al, 2012a). As the pulse grain sizes were (in most cases) smaller than the median bed grain size, a corresponding fining of the bed also occurred at these locations. Our simulations show that downstream changes in channel slope and width are strong controlling factors in pulse deposition, which is consistent with the findings of Major et al. (2012).

Sediment pulses finer than the median bed surface are transported faster and arrive

downstream sooner than pulses that have a median grain size more similar to the bed surface (Figure 3.4; Cui et al., 2003a, 2003b; Cui & Parker, 2005; Sklar et al., 2009). An increase in the magnitude or frequency of sediment-transporting flows increases the sediment-transport capacity of rivers, resulting in sediment pulses that translate/disperse quicker (Cui & Parker, 2005) and arrive sooner (Figure 3.4). The 2-year recurrence interval flow, Q_2 (~105 m^3/s in the upstream end of modeled portion of the Nisqually), is often used as an approximation for the bankfull discharge (e.g. Snyder et al. 2013). The threshold for motion of D_{50} tends to occur at flows below the bankfull discharge (Parker, 1978). This is particularly true in high sediment supply channels such as the Nisqually (Pfeiffer & Finnegan, 2018; Pfeiffer et al., 2017). Thus, we expect Q_2 (and larger flows) should be sufficient to move a pulse grain size that is close to the median bed particle size (70 mm). In our models, we saw major changes occur when the flow was above Q_2 (Figures 3.4, 3.7). For the 70 mm pulse, we saw that major changes occurred (at 1.2 and 3.2 years) when flow was significantly higher (~170 and ~250 m^3/s, respectively) than Q_2 (Figure 3.7). Gran & Czuba (2017) concluded that storage and dispersion become important when background sediment load is high. We saw gradual incision during the baseline simulation (Figure 3.3b), which reflects our relatively small background sediment supply. Additionally, because our pulse grain sizes were finer than the bed sediment (except the 70 mm pulses), we expected and observed translation of the sediment pulses (nearly horizontal lines in contour plots, Figures 3.5-3.7; Cui et al., 2003a, 2003b; Cui & Parker, 2005; Lisle, 2008; Lisle et al., 1997, 2001; Sklar et al., 2009).

Our simulated model results showed that changes in sediment depth and bed grain size distributions were primarily influenced by sediment-pulse grain size and distribution type (Figures 3.5-3.7). The influence of streamflow hydrology was secondary and sediment-pulse volume (or depth) was tertiary, compared to the effects of pulse grain size (East et al., 2018; see Appendix). This finding is in contrast to modeling by Czuba et al. (2012a), who

increased pulse volume fivefold (compared to our lower threefold increase) and found higher impact of pulse volume on the river bed compared to streamflow. The relative impact of flow and pulse volume, thus, will depend on the specifics of each. As expected, aggradation mostly occurred in reaches with low bedload transport capacity (e.g., Figure 3.9; Cui & Parker, 2005; Czuba et al., 2012a). In general, our simulated pulses caused slight long-term aggradation from baseline, but when the median pulse grain size was small compared to the bed sediment (10 mm pulse, roughly 0.15 of the median bed gravel size; Figure 3.5 and Appendix S3), incision dominated. One possible reason is that the mixing of the finer pulse with the pre-existing bed sediment modifies the bed sediment size distribution in a way that leads to overall increased sediment transport (Wilcock & Crowe, 2003; Venditti et al., 2010b). Our larger volume pulses traveled faster through the system than our smaller volume pulses. This occurred because the smaller volume pulse more fully mixed with the bed material compared to the larger volume pulse and the larger volume pulse also further increased the local channel slope to increase the transport rate.

3.6.2 Differences Between Uniform and Mixed Grain-Size Pulse Behavior

Our model simulations demonstrated how mixed-size sediment pulses, which are common in natural and human-influenced riverscapes, may affect downstream bed elevations, grain size, and sediment transport differently than uniform-sized sediment pulses, which have been more commonly studied. The arrival time of 50% of the pulse was nearly the same for the uniform and mixed pulses (finer than the bed), but the coarse tail of the mixed pulse traveled slower (Figure 3.4). We also found that incision due to a finer pulse was more prevalent for a uniform pulse compared to a mixed pulse (Figure 3.5). This is likely because the mixed

pulse dispersed slowly compared to the uniform pulse that translated with less spread, which led to greater magnitude change. When the median grain size was close to that of the bed, the mixed pulse traveled very slowly in the system and resulted in a more diffuse impact compared to the uniform pulse (Figure 3.7). In general, the finer fraction of the mixed pulse traveled quickly and interacted with the bed in downstream locations first, while the coarser fraction traveled very slowly; thus, the pattern of bed-elevation change was more variable with a mixed pulse than a uniform pulse.

Model simulations included three different sized mixed pulses, where the mixed pulse with an intermediate gravel size (roughly 0.5 of the median bed gravel size) caused the largest downstream aggradation. As expected, the finer mixed pulse caused less aggradation, but when the median gravel size of the mixed pulse was roughly the same size as that of bed (70 mm), we found similarly low aggradation (Figure 3.8a; Czuba et al., 2012a; Sklar et al., 2009). The mixed pulse with 70 mm median grain size dispersed slowly (Figure 3.4), which allowed small and finer portions of the pulse to move through the system without much deposition. This novel finding suggests that there is an intermediate median grain size for mixed-size sediment pulses (here, roughly 0.5 of the median bed size) that may result in the largest downstream bed impacts, because finer sizes are transported through too quickly and coarser sizes disperse too slowly to exert influence over year to decadal timescales.

Another noteworthy result from the simulations is that mixed-size pulses with median grain sizes smaller than the bed increased bed mobility more than pulses of uniform-size distributions (Figure 3.10a). This is because finer mixed pulses incorporate a range of fine grain sizes into the bed and increase the mobility of larger grains without completely blanketing them in a uniformly fine layer of sediment. Whereas, mixed-size pulses with size and distribution equivalent to the preexisting bed, disperse very slowly, reduce background sediment

supply, and limit sediment export (70 mm mixed pulse, Figures 3.10a, b). Thus, to increase bed mobility downstream, rather than adding a relatively fine and uniformly distributed pulse (Arnaud et al., 2017; Gaeuman et al., 2017; Venditti et al., 2010), our model results suggest that bed mobility would be enhanced if the pulse has a wide grain size distribution.

3.6.3 Limitations and Future Improvements

While this study only focused on the one-dimensional aspects of sediment-pulse evolution, the spatial complexity of rivers can influence patterns of sediment-pulse evolution (Kasprak et al., 2015; Nelson & Dubé, 2016; Recking et al., 2016). Our simulated sediment depths are of a sediment volume deposited uniformly over the entire width of 400-m sections of river, so in reality, we would expect locally greater accumulations to occur. Local or reach-scale topography can affect how sediment pulses are transported through a reach and affect how well bedload equations developed from flume studies translate to field scale (Recking et al., 2016). Sediment pulses tend to accumulate on point bars and their growth can modify flow patterns and lead to more active channel migration (Humphries et al., 2012; Parker et al., 2011). Additionally, sediment can fill pools or locally deposit behind large woody debris, further complicating sediment-pulse evolution (Harrison et al., 2018; Major et al., 2012; Ryan et al., 2014; Wohl & Scott, 2017). The model used in this study does not currently consider time-varying channel width, and the interactions among bank supply, bed structure, and lateral sediment exchange, as does the MAST-1D model.

Another major limitation of the current work was that the model was not able to maintain a bed material with enough sand to match the measured grain size distributions

from gravel bars. This means that in reality, for the Nisqually River, bed sediment is probably more mobile and would transport downstream faster than we have predicted. When sand content was high (above 5%), the model flushed out most of the sand from the network. As a result, we noticed bed incision and corresponding bed coarsening at flow peaks (Figure 3.3). Without a separate transport equation for sand, as is done in the TUGS model, our present model was unable to effectively characterize sand transport. While our model was able to route a gravel mixture, the inclusion of a sand transport equation would make it more robust in simulating the transport of combined gravel and sand mixtures, particularly in the challenging case of the Nisqually River.

Our model results are applicable to sediment pulses on the order of 10,000 m^3, such as from small dam removals (<10 m high, delivering less than 10,000 m^3; Bellmore et al., 2017; Foley et al., 2017; Major et al., 2017) and gravel augmentation (23,000 m^3; Arnaud et al., 2017). These are the sediment-pulse volumes typically encountered by river managers. In the past few years, more datasets of larger sediment inputs, primarily from larger dam removals (Cashman et al., 2021; East et al., 2015, 2018; Harrison et al., 2018; Major et al., 2012; Pace et al., 2017; Ritchie et al., 2018; Warrick et al., 2015) and modeling studies using these datasets (Cui et al., 2014, 2019; De Rego et al., 2020) have appeared in the literature. In the future, more directly testing an updated model against these datasets would provide a robust validation of large sediment-pulse movement in rivers.

3.7 SUMMARY

This study utilized existing physical measurements of the Nisqually River for applying a previous Lagrangian, bed-material sediment transport model. We sought to investigate how

perturbations in sediment supply, modeled as sediment pulses in this river system, dictate the bed response. Specifically, we were interested in showing how mixed-size sediment pulses, which are common in natural and human-influenced river systems, affect downstream bed elevations, grain size, and sediment transport differently than uniform-sized sediment pulses, which have been commonly studied. Our model results are applicable to sediment inputs on the order of 10,000 m^3. Simulation results pointed to an initial pre-pulse incision followed by sediment accumulation at the time of pulse arrival, and then, complex post-pulse changes. Sediment pulses were strongly translational when pulses were finer than the existing bed material. Introduced pulses caused slight long-term accumulation (especially at downstream reaches with low transport capacity) in general, but if the pulse grain size was much finer than the bed sediment (roughly 0.15 of the median bed gravel size), incision may occur due to increased bed-sediment mobility. We saw that the flow hydrograph had a strong control over the timing of these sedimentologic changes.

We found that pulse distribution type (uniform or mixture) was an important influence on the channel bed. Results of model simulations indicated that a mixed pulse with an intermediate gravel size (roughly 0.5 of the median bed gravel size) may cause higher downstream accumulations compared to a mixed pulse with a median gravel size much finer than or equivalent to that of the bed because either finer sizes move through quickly or coarser sizes disperse slowly. Furthermore, mixed-distribution pulses with smaller median grain size than the bed increase bed mobility more than uniform-distribution pulses. This is because finer mixed pulses add a range of fine grain sizes to the bed, thereby increasing the mobility of the larger sizes without covering them in a uniformly fine layer of sediment.

This research furthers our understanding of the space-time evolution and downstream effects of sediment pulses in gravel-bedded rivers, and contributes to river management by

assessing potential fluvial geomorphic response due to discrete inputs of sediment that could be from natural or anthropogenic sources. Finally, this work revealed that incorporating a sand transport equation into our model in the future will be necessary in order to make it more robust for simulating the transport of combined gravel and sand mixtures. Future model improvements could also include channel-floodplain exchange of water and sediment and future validation should take advantage of recent datasets describing river response to dam removal.

Chapter 4

Control of flow sequence and spatial distribution of debris flow input on river network modeling

4.1 Abstract

Debris flows can have long-term effects on a watershed as deposited sediment at the upstream end of a river network can act as a sediment supply source for decades to centuries. Therefore, long-term simulation is critical to predict the combined effects of flow magnitude, duration, sequence, and intermittency for debris flow sediment routing. While such modeling scope in large spatial and temporal scale is often restricted by computational capacity, simplifying the flow hydrograph can help make the modeling tractable. Along with a 30-year daily flow simulation, this study explores the control of flow sequence and constant flow on debris flow transport through a river network at different time horizons. Additionally, this work also investigates the effect of differences in spatial distribution of debris flow sediment input to the network by analyzing corresponding tributary and mainstem characteristics. Simulation results from the reduced hydrographs (of constant flow and different sequences) show that these can produce long-term transport comparable to the original flow record. Although the initial (1-5 years) discrepancy is high, these differences decrease over time (after 10

years). The effect of flow sequences was less important for sand than gravel, as both high and low flow would move sand initially. This eventually results in high total transport when the low flow years are followed by high flow years, because later high flows can move the coarse gravel after the early sand removal by low flows. Because the simple compressed hydrograph approximated long-term transport, we employed a constant flow hydrograph to investigate the network characteristic controls on debris flow sediment transport. Model results showed the importance of drainage area ratio between the tributary and mainstem on storage (in mainstem and reservoir), similar to previous studies. When mainstem slope was similar to the tributary slope, the resulting overall transport was more efficient. This study also suggests that the extent of mainstem aggradation depends mainly on mainstem slope properties. Such a network-scale modeling study quantitatively identifies geomorphically significant tributaries, which are important for river biodiversity. Besides, this study focuses on how the results from a reduced hydrograph vary from long-term records at different timescales. With the expected future increase of magnitude and frequency of high floods, and the potential of increased severity and frequency of extreme events due to climate change, the long-term simulation of flow sequences can inform river managers about how to better prepare to reduce loss from debris flows, and to improve overall river and watershed management.

4.2 Introduction

Debris flows are often generated in bedrock hollows at heads of first-order basins (Benda, 1990). This debris flow pulse of sediment, saturated with water, gains momentum due to gravity and surges down steep mountain slopes (Iverson, 1997). Final debris flow volumes can be several times larger than its initial volume as it accumulates material (older accumulated

sediment and organic debris) from headwater, first- and second-order channels along the way (Benda, 1990; Iverson et al., 2011; Medina et al., 2008; Pirulli & Pastor, 2012; Scott, 1988; Takahashi, 1981; Wang et al., 2003). These debris flow sediments deposit in valley bottom fans, gravel bars, or narrow floodplains, or can travel long distances downstream with fluvial reworking (Lancaster & Casebeer, 2007; Lancaster, 2008; Lyon and O'Connor, 2008; Murphy et al., 2019; Pierce et al., 2011). When triggered by intense rainfall, especially in areas influenced by wildfires, a debris flow can cause intense and devastating effects. The damages to lives, infrastructures, aquatic wildlife can be catastrophic in such cases, but still often are underestimated due to disregard for long term and indirect effects of debris flows (Chen et al., 2013; Cui et al., 2011; Murphy et al., 2019; Tang et al., 2011; Xu et al., 2012).

Increased wildfire risk is a major effect of climate change and post-wildfire landscapes can deliver large quantities of sediment to streams (Jia et al., 2019; Nyman et al., 2020). Beyond direct watershed risks from fires, post-wildfire erosion also presents threats of increased erosion and subsequent delivery of sediment to stream channels (Benda et al., 2004a; Moody & Martin, 2004; Murphy et al., 2018, 2019; Sankey et al., 2017). The spatial and temporal distribution of sediments in alluvial channels is not only influenced by debris flow deposits, but also their role as a source for accelerated transport of sediment farther downstream (Benda, 1990). Excessive sediment loading can increase flood risk, alter aquatic habitat, and/or be transported downstream to impact water supply reservoirs (Moody & Martin, 2001; Smith et al., 2011; Reneau et al., 2007; Robinne et al., 2016). Therefore, research on the dynamics of debris flow sediment transport through river networks, including sediment entrainment and deposition, is becoming extremely indispensable to enhance efficient river and watershed management, and reduce loss from debris flows.

With the growing capability of predicting post-wildfire erosion (location, probability,

and magnitudes) and advancement of river network modeling, we can now utilize a modeling framework that combines all components from source to sink to investigate debris flows at watershed scales (Ahammad et al., 2021; Czuba, 2018; Gartner et al., 2014; Murphy et al., 2019; Staley et al., 2017). In particular, the modified Czuba (2018) model had been applied at the watershed-scale to explore sediment pulses (finer than the bed) and debris flow sediment transport dynamics (Ahammad et al., 2021; Murphy et al., 2019). The model can track debris flow sediment inputs through river networks and thus, allows us to investigate the influence of different controls (e.g., hydrology, network structure) over debris flow sediment transport by capturing complex transport and network processes. In the absence of ample field studies, specifically long-term monitoring of debris-flow sediment input location, the downstream river, and its outlet (perhaps to a downstream reservoir), modeling studies can be very useful for investigating debris flow transport, in particular from post-wildfire landscapes.

After a debris flow event, deposited sediment at the upstream end of a river network can remain in storage for decades to centuries, and may become a major and sudden source of upstream sediment supply to the network later (Montgomery & Buffington, 1998; Harris et al., 2015). Thus, long time-scales can be very important to simulate the full effects of debris flows in river networks. While even under constant flow, bedload transport itself is a highly fluctuating temporal phenomenon (Recking et al., 2012). Although high flows move the most sediment, the relation between flow and the amount of sediment transported is highly nonlinear, often with hysteresis, i.e., the peak of sediment transport may not occur at the time of peak of flow discharge (Mao, 2018; Lee et al., 2004; Humphries et al., 2012; Reid et al., 1985; Kuhnle, 1992). There are limited experimental and numerical studies that simulate the effects of different hydrographs (Mao 2018; Gunsolus & Binns, 2018; Phillips et al., 2018; Hassan et al., 2006; Bombar et al., 2011; Humphries et al., 2012; Guney et

al., 2013; Ferrer-Boix & Hassan, 2015; Masteller & Finnegan, 2017), but still the ability of long-term flow simulation combining the effects of flow magnitude, duration, sequence and intermittency on sediment transport in river networks is relatively unexplored (Murphy et al., 2019; Nyman et al., 2020). Moreover, if simulations can adequately condense the sediment transporting effects of a long-term daily hydrograph to a simpler constant flow that can yield similar long-term transport and other geomorphic characteristics, that would significantly improve computational efforts (Czuba & Foufoula-Georgiou, 2014; Paola, 1992; Parker, 2004).

Additionally, with long-term debris flow simulations, there is an opportunity to investigate the movement of debris flow deposits from various tributaries to the mainstem river and eventually to downstream reservoirs. Benda et al. (2004a) documented tributary confluence effects in 19 nonregulated streams and rivers across the western United States and Canada, where debris flows were the dominant type of sediment supply in seven of them. Using conceptual models, other studies (Benda et al., 2004b; Rice et al., 2001) presented the discontinuity concept and network dynamics hypothesis, but issues like the extent of aggradation, proportion of aggradation compared to supply, etc. were not possible to systematically evaluate. Rice (2017) proposed an automated method for predicting tributary-driven aggradation in large drainage networks mainly from field observations. Sediment supply from steep headwaters and its storage in fluvial channel networks and reservoirs has been explored theoretically as well (Benda & Dunne, 1997a, 1997b). Studies combining field observations and simple models are helpful for examining debris flow sediment transport processes, linking catchment morphometry and geomorphic processes (Nyman et al., 2020). But recent concepts of connectivity and sediment cascades provide the most robust way of considering spatially explicit, time-dependent adjustment of bed material grain size and bed elevation with the use of distributed numerical models for river networks (Czuba, 2018; Gran

& Czuba, 2017; Cavalli et al., 2013; Heckmann & Schwanghart, 2013; Bracken et al., 2015; Parsons et al., 2015; Lisenby et al., 2017; Schmitt et al., 2016; Wohl, 2017). Thus, river network modeling can be used to detect the potential for large geomorphic changes around confluences, and also identify basin-scale controls on debris flow aggradation in the network.

This study is motivated by the need to constrain some of the uncertainties and unknowns surrounding modeling debris flow sediment impacts in river networks with appropriate temporal and spatial scales such as the choice of hydrograph and the importance of network structure. An updated river network model based on Czuba (2018) and Murphy et al. (2019) (described herein), capable of tracking debris flows over an erodible bed, was applied to the Jordanelle Reservoir watershed of the Wasatch Range above Salt Lake City, Utah, USA. The objectives of this study were twofold – first, to explore the role of hydrograph sequences and constant flow compared to the long-term (30-year daily) hydrograph, and how the results vary in terms of debris flow transport and impacts at different timescales. The second objective was to examine network properties that control debris flow sediment delivery from first-order upstream sources to a downstream reservoir, and subsequent aggradation along the river network. Model simulations were designed to test the hypothesis that hydrograph sequencing matters at short timescales (e.g., Humphries et al., 2012; Guney et al., 2013; Phillips et al., 2018; Waters & Curran 2015), but at longer timescales this sequencing becomes less important. We wanted to determine at what timescale this shift might occur relative to important timescales in assessing post-wildfire debris flow sediment transport and impacts at watershed scales. The hypothesis for the second aim was that, debris flows with the same properties will travel though and aggrade the river network differently based on their location on the network. This is important because knowing how the same input might affect a river network differently depending on its spatial input location in the network could help better inform management of post-wildfire landscapes. With improved understanding

of debris flow sediment transport and deposition in river networks under different hydrologic conditions and spatial distributions of inputs, this study adds to the knowledge of how to most efficiently model how debris flows affect downstream water resources.

4.3 Study Area

Our study site is the Provo River network upstream of the Jordanelle Reservoir that drains 650 km^2 area of northern Utah in the Intermountain West (Figure 4.1), characterized by a mid-continental mountain climate, high average elevations, and complex mountain topography. Influenced by these factors, temperature and precipitation vary widely with elevation changes, with the majority of precipitation falling as snow during winter months (WWA, 2021). Over the next few decades, wildfires are expected to increase in size, frequency, and burn severity throughout the western U.S. due to artificially high fuel loads, climate warming, and increased duration and severity of drought (Moody & Martin, 2009; Flannigan et al., 2009; Liu et al., 2010; Pechony & Shindell, 2010; Miller et al., 2012; Westerling et al., 2011). Along with decreases in snowpack and earlier snowmelt timing, post-wildfire debris flow sediment delivery to downstream reservoirs will contribute to declining reservoir storage capacity as well. Reservoir sedimentation is now a leading concern for water security and management throughout Utah as these reservoirs are critical water supplies (Goharian et al., 2017).

We simulated this river network with a total river network length of 212 km, the eastern and southern tributaries of which initiate from very steep slopes (∼5%; Figure 4.1). We applied our model here, because this network has some large steep tributaries that are

prone to act as sediment supply sources. Moreover, available data from three USGS gages (especially USGS 10155000, just upstream of the reservoir; shown in Figure 4.1) allows us to reliably estimate roughness, peak flow, and translate the discharge throughout the network, which are important for constraining our model to test our hypotheses.

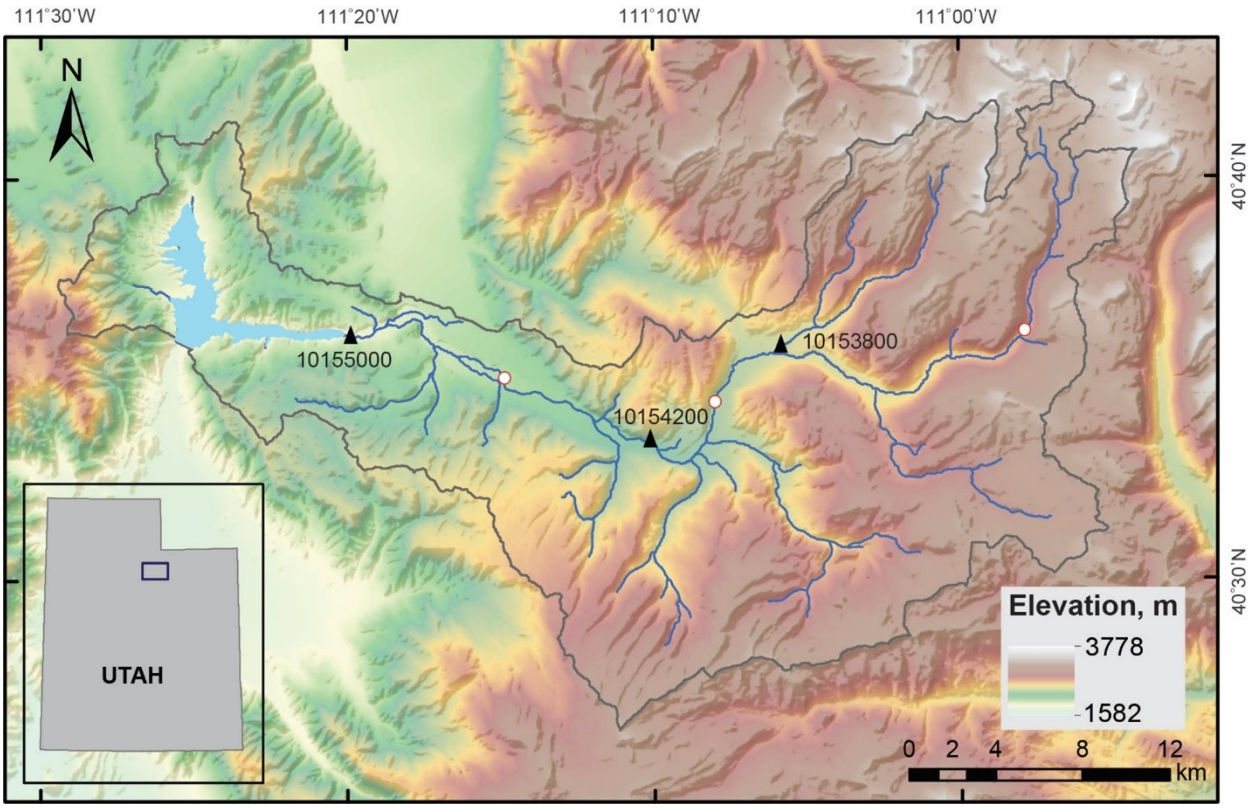

Figure 4.1: Study area map of the Provo River watershed upstream of the Jordanelle Reservoir, Utah, USA. The three USGS gage (black triangle) and three locations of simulation results (of Figure 4.10 - 4.12; white circles) are marked within the modeled extent.

4.4 Methods

4.4.1 Debris Flow Inputs

A novel framework developed by Murphy et al. (2019) was used in this work to predict post-wildfire sediment generation and sediment impacts downstream from burned areas by linking debris flow generation and network-scale sediment routing models (Figure 4.2a). The input sand fraction from hillslope erosion (Figure 4.2c) is also considered here from the Revised Universal Soil Loss Equation, RUSLE (Ganasri & Ramesh, 2016). Post-wildfire debris flow generation was predicted using a probabilistic model for the western U.S. (Staley et al., 2017), coupled with an empirical model to predict debris flow volumes (Gartner et al., 2014). Debris flow sediment delivery to the stream network was estimated using a geometric model (Murphy et al., 2019). Grain size distributions (GSDs) of post-fire debris flows were based on data (Figure 4.2b) compiled from the literature and recent field surveys conducted across Utah (Wall, 2021).

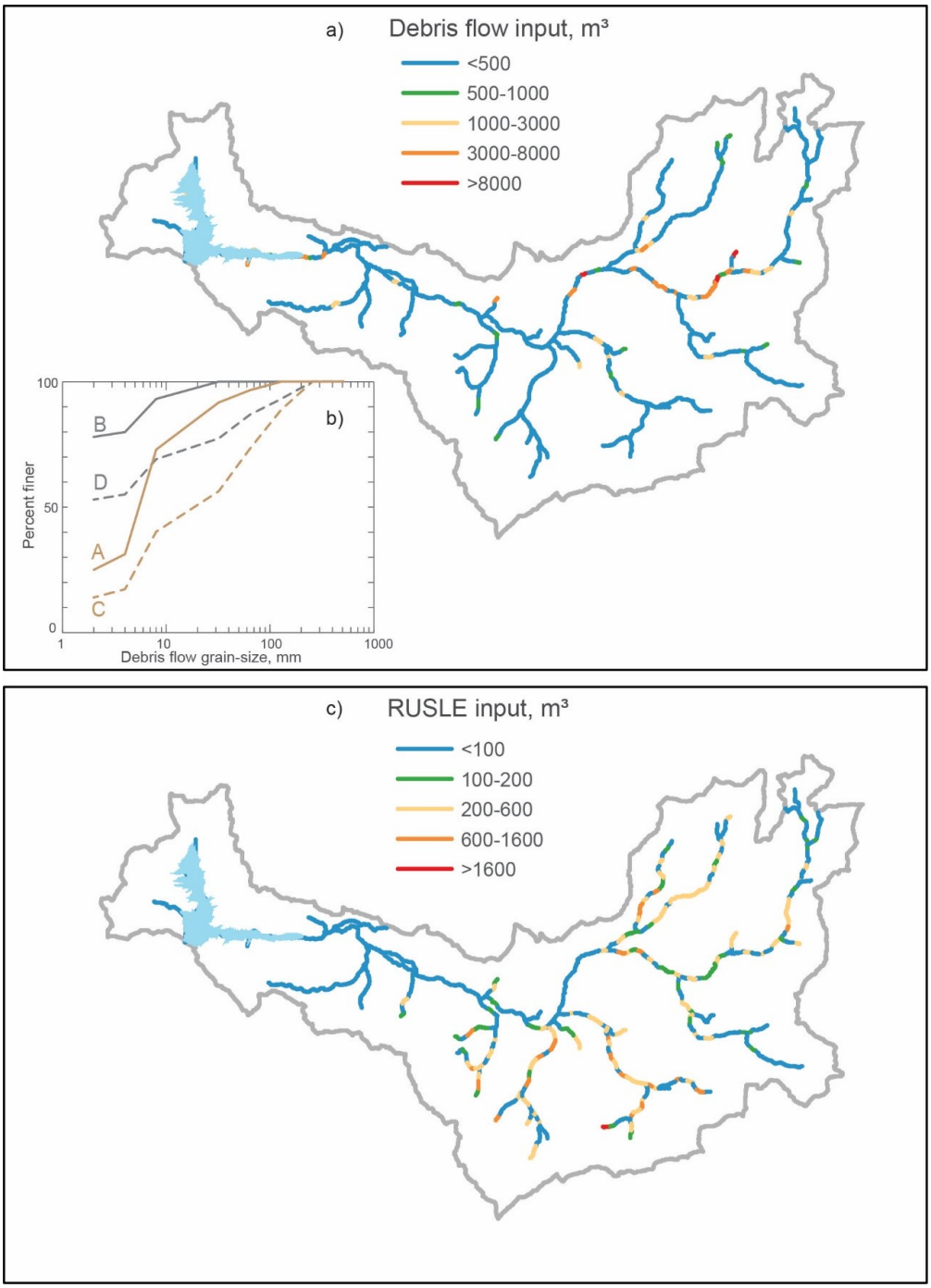

Figure 4.2: Sediment inputs from debris flows and hillslopes (RUSLE) as the initial condition in model simulations. a) location and volume (total 165,000 m^3) of debris flow input; used as an initial condition for section 4.4.3, b) observed grain size distribution of debris flows (Wall, 2021); Distribution A (25% sand) and B (78% sand) will be used later for coarse and fine debris flow simulations, c) location and volume (total 65,000 m^3) of RUSLE input; used as initial condition for sections 4.4.3 & 4.4.4.

These sediment inputs (Figure 4.2) provide a consistent initial condition for the next simulations. This work is focused on routing this input and additional sediments through the Provo River network to the Jordanelle Reservoir.

4.4.2 Sediment Routing Modeling

We used a network-based 1D Lagrangian sediment routing model (Czuba, 2018) for this gravel bedded river network that utilizes the surface-based, mixed-size bedload transport equation of Wilcock and Crowe (2003). Details of the model were discussed in the previous chapter and related works (Ahammad et al., 2021; Czuba, 2018). We are focusing here only on the modeling aspects that are different from the previous chapter.

The river network was delineated from a 10 m DEM (USGS, 2022). The total 212 km-long Provo River network upstream of the Jordanelle Reservoir was modeled in this study by discretizing it into links all less than or equal to 500 m or at locations in between tributaries. This resulted in a total of 462 links, where 350 links had an equal length of 500 m. Because river bed elevations were extracted from a 10 m DEM, some unusual flat links were identified in the network. Therefore, we smoothed the slopes of the network links under the following conditions (similar to the smoothing steps inherent in the National Hydrography Dataset; Moore et al., 2019). Going from downstream to upstream, we iterated this process through the network several times until these conditions were met everywhere. A minimum slope of 0.1% was also imposed for all links to account for any erroneously low-sloped sampling points.

$$Slope_{d/s\ link} \geq 0.7 \times Slope_{u/s\ link} \tag{4.1}$$

And,

$$Slope_{d/s\ link} \leq 2 \times Slope_{u/s\ link} \tag{4.2}$$

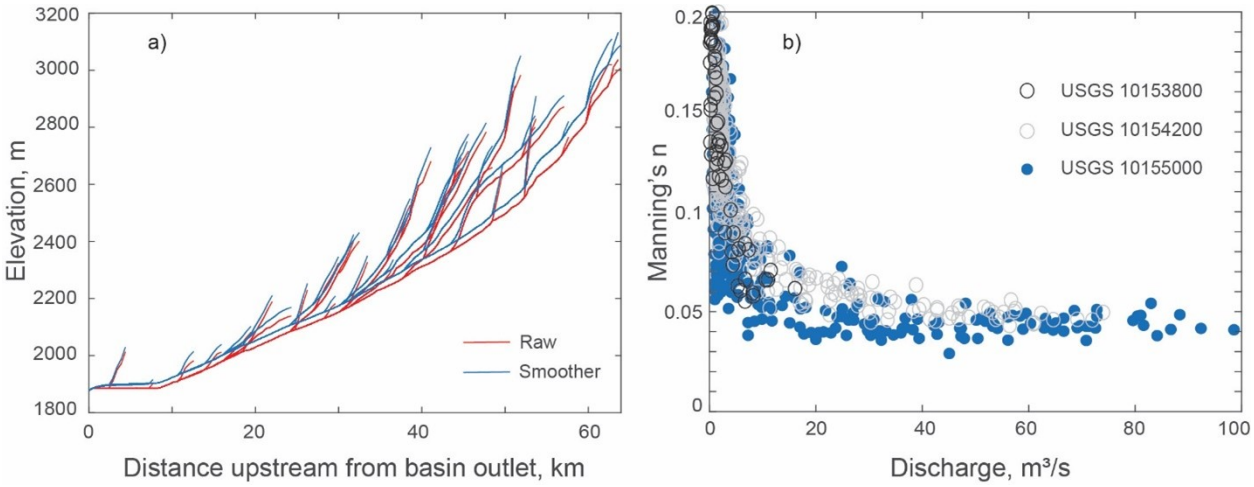

Figure 4.3: Slope smoothening and Manning's roughness for the Provo River network upstream of the Jordanelle Reservoir. a) Raw (red) and smoothed (blue) elevations. The lower 9.1 km of the network is the flat reservoir accounting for the most vertical change between the two profiles. Sediment immediately entering the reservoir was removed from network transport. b) Calculated Manning's n values for three USGS gages from field measurements. The 2-year flow at USGS 10155000 is 66.4 m^3/s, with a corresponding n value of nearly 0.045.

The resulting elevations are shown in Figure 4.3a, where relative steepness of the network was well preserved. We calculated Manning's n values for different flows at USGS gage stations from field measurements using the following relation

$$\mathrm{n} = \frac{AR^{2/3}S^{1/2}}{\mathrm{Q}} \tag{4.3}$$

where channel cross-sectional area A, hydraulic radius R, and flow discharge Q were calculated in SI units, and S is the channel slope from the network at the location of the gage.

We used a constant n-value of 0.045 for our simulations to set the flow depths, because it was the typical value during high sediment-transporting flows (Figure 4.3b). We demarcated the maximum flow depth as bankfull depth (assuming the depth corresponding 2-year flow) to limit the increase of shear stress infinitely when flow starts inundating the floodplain.

The maximum volume of sediment (χ) that can be moved in any link, or capacity of the link at any time is set by

$$\chi = \ell B L_a \tag{4.4}$$

where ℓ is the link length, B is the channel width, and L_a is the active layer thickness of that link. Because all the links are not of the exact same length, shorter links that occurred specifically at the confluences, may cause artificial bottlenecking due to lack of capacity. We adjusted the link capacity as follows to overcome this issue, along with ensuring a high enough capacity at the most upstream narrow links to move debris flow pulses.

$$Capacity_{d/s\ link} \geq 0.7 \times Capacity_{u/s\ link} \tag{4.5}$$

And,

$$Capacity_{most\ u/s\ link} \geq Mean\ Capacity \tag{4.6}$$

The initial median bed particle size (D_{50}) was set throughout the network as a function of channel width (B) and slope (S) following a reduced form of the equation provided by Snyder et al. (2013) as

$$D_{50} = \frac{n^{3/5} Q_2^{3/5} S^{7/10}}{R \tau_c^* B^{3/5}} \tag{4.7}$$

where n is the Manning roughness coefficient, Q_2 is the 2-year recurrence interval flow, and τ_c^* is the critical Shields parameter to mobilize D_{50}. This equation assumes that the D_{50} is mobilized (and set) by a the 2-year recurrence interval flow. We implemented Equation 4.7

using an assumed τ_c^* of 0.05 and calculated n of 0.045. We imposed the condition that the D_{50} in any link was greater than half of the mean D_{50} of the network to avoid any very small D_{50} in links with very low slopes.

We started the model with 4.6% sand in the bed (observed from Clear Creek watershed in Utah; Murphy et al., 2019), with the initial gravel distribution approximated as log-normal with median gravel sizes for each link calculated from Equation 4.7, and standard deviation of $\sim$1.5 mm calculated from the observed distribution in an adjacent watershed (draining to the Rockport Reservoir; not shown here). Due to the absence of subsurface data, it was initialized to be the same as the surface size distribution. Sediment load by grain size, was supplied to the model at all upstream boundaries by creating a sediment supply reservoir at the upstream end of the model (same as in Ahammad et al., 2021). We did this by adding sediment parcels to the bed surface layer at the most upstream links in a sufficient volume as to not empty during the simulation. We also fixed the bed elevation at the upstream end of this link so that the added bed volume did not increase the channel slope. The streamflow continuously eroded this background sediment from this sediment supply link and transported it downstream. The grain sizes and distribution of background sediment was kept coarser than the debris flow inputs (distribution D when debris flow grain size distribution (GSD) was B, and distribution C when debris flow GSD was A; Figure 4.2b). We assigned a maximum parcel volume of 10 m^3 for all sediment parcels. Grain size of any parcel was given a discrete value among 0.5, 2.83, 5.66, 16.0, 45.3, 90.5, 181, and 362 mm, which are the mean sizes for sand and of gravel (computed in log scale) within grain size bins bounded by 2, 4, 8, 32, 64, 128, 256, and 512 mm. We did not have field observations of bed sediment grain-size distributions to accurately validate this initial condition, but these sizes were similar to those in reasonable the adjacent river network draining to the Rockport Reservoir. More importantly, this initial condition allowed us to numerically route the debris

flow sediment without degrading the existing river bed, and thus test synthetic scenarios of flow sequences and spatial distributions of debris flow sediment input.

Apart from the above model parameterizations, two key modeling aspects were advanced in this work. First, we slightly modified the first-in, last-out rule for how sediment parcels are selected to be in transport versus subsurface storage (detailed in Ahammad et al., 2021; Czuba, 2018). Here we subdivided each link in two equal parts, and distributed the total capacity in a 7:3 ratio between the upstream half and downstream half of the link length, respectively. The most recent parcels to arrive in the upstream half of a link were positioned in the active surface layer whose cumulative volume was $\leq 0.7\chi$, while the most recent parcels in the downstream half of the link whose cumulative volume was $\leq 0.3\chi$ were also placed in the active layer. As a result, there was more continuity of sediment moving through a link rather than that sediment becoming buried by incoming sediments that were entering at a rate greater than could transport out of the link. This change was most important when link length was long compared to the simulation timestep.

The second major advancement was the consideration of stress partitioning in this gravel-bedded river network. The presence of large immobile grains reduces flow energy and the shear stress available to move sediment in gravel-bed streams. This effect is considered here with stress partitioning from Rickenmann (2012). This method uses a reduced energy slope S_0, instead of actual S. In this study, S_0 was calculated by relating S to the Darcy–Weisbach friction coefficient f (Equation 4.8). With the partitioning between base level, f_0 (defined by Manning–Strickler-type approach, Equation 4.9) and total resistance, f_{tot} (from the variable power equation of Ferguson (2007) wherein the coefficients a_1=6.5 and a_2=2.5;

Equation 4.10) and exponent $e \approx 1.5$ (Rickemann, 2012), it then can be expressed as

$$\frac{S_0}{S} = \left(\sqrt{\frac{f_0}{f_{tot}}}\right)^e \tag{4.8}$$

where f_0 and f_{tot} are calculated as

$$\sqrt{\frac{8}{f_0}} = 6.5\left(\frac{H}{D_{84}}\right)^{1/6} \tag{4.9}$$

$$\sqrt{\frac{8}{f_{tot}}} = \frac{a_1 a_2 \left(\frac{H}{D_{84}}\right)}{\sqrt{a_1^2 + a_2^2 \left(\frac{H}{D_{84}}\right)^{5/3}}} \tag{4.10}$$

4.4.3 Hydrograph Structures and Flow Sequences

We utilized the daily streamflow record of the USGS gage near the basin outlet (USGS 10155000; Figure 4.1). This gage flow (Q_{gage}) was scaled throughout the network according to drainage area (DA), following the relation of Equation 4.11.

$$Q_{ungaged} = Q_{gage}\left(\frac{DA_{ungaged}}{DA_{gage}}\right)^{0.84} \tag{4.11}$$

The exponent 0.84 was set for this watershed according to its location in geohydrologic regions of Utah (Kenney et al., 2007). We compared the resulting streamflow to the available gage records at the other two gages (USGS 10154200 and USGS 10153800; see locations in Figure 4.1) within the watershed. The comparison between modeled discharge and observed discharge is shown in Figure 4.4, with a close agreement (Nash–Sutcliffe model efficiency coefficient, NSE=0.954 and 0.894 for USGS gage 10154200 and 10153800 respectively; Nash & Sutcliffe, 1970), supporting the use of above relation (Equation 4.11).

To investigate the effect of hydrograph structure and sequencing on debris flow sediment transport, we assembled several different hydrographs. The first was a 30-year daily hydrograph (H1, Figure 4.5). The second (H2) assumed that the 2-year flow alone was important for transporting debris flow sediment volumes (Czuba & Foufoula-Georgiou, 2014; Paola, 1992; Parker, 2004). Since the simulated debris flow grain size (5.5 mm median size for coarser GSD A; Figure 4.2b) was finer than the bed (median size $\sim$ 150 mm in mainstem), we also constructed a hydrograph that kept all the flows greater than half of the 2-year flow (H3). Thus, the 30-year daily hydrograph was reduced to 688 days by excluding all the

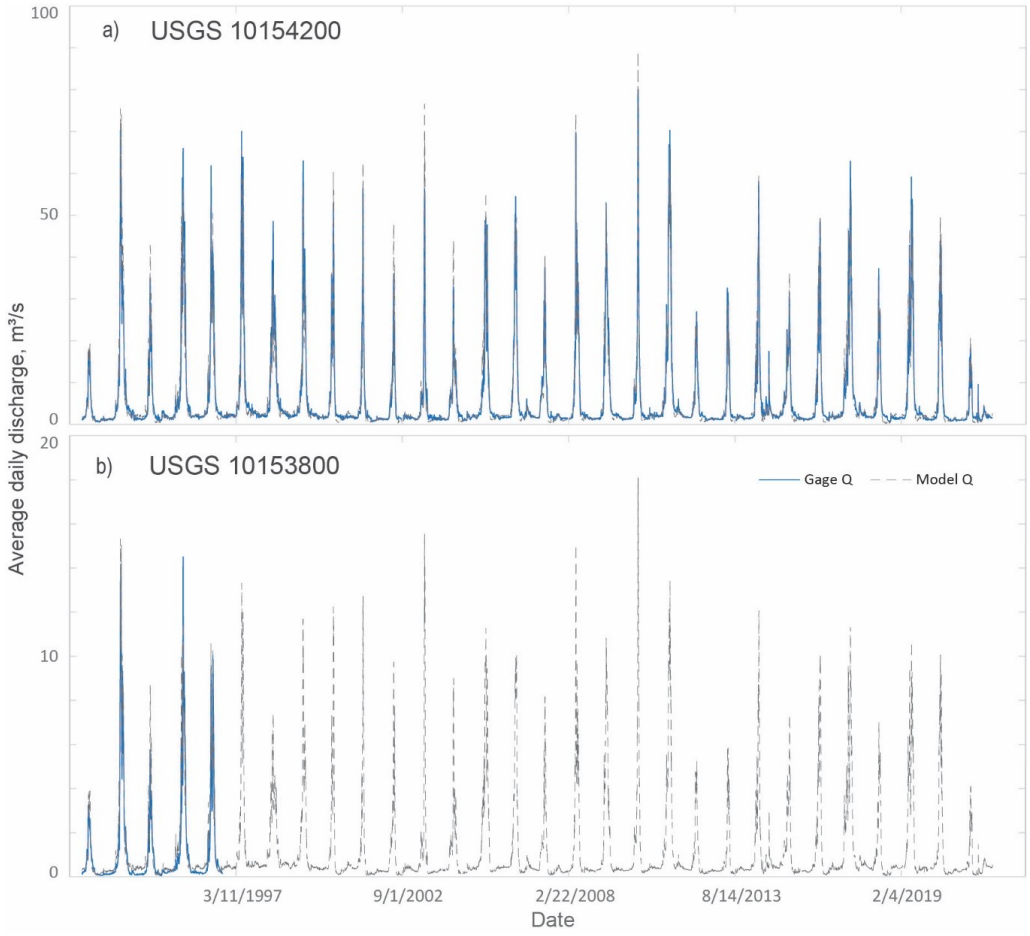

Figure 4.4: Comparison between scaled (from Equation 4.11) and observed streamflow at a) USGS 10154200 (NSE = 0.954), and b) USGS 10153800 gage (NSE = 0.894). The gage locations are shown in Figure 4.1.

low flows (lower than half of the 2-year flow). Different sequencing by average one-year sections of this reduced hydrograph (low year to high year: H4; high year to low year: H5; and randomizing years: H6) was tested for debris flow simulation, along with completely randomizing the 688 days of flow (H7; complete loss of any hydrograph sequencing). For the constant 2-year flow, we simulated for 344 days, i.e., half of that of the reduced hydrograph which had flows over and below 2-year flow.

Although these hydrographs have different length of time (i.e., H1 30 years, H2 344 days, and H3 to H7 688 days), all were generated from the 30-year original flow record (Figure 4.5). We translated all the results (in Section 4.5.1) from the compressed hydrographs to a corresponding time of the original 30-years by simply calculating the average number of days in the compressed hydrograph to represent each year in the original 30-year hydrograph. Therefore, hydrograph H2 represents each year by 11.5 days (30 years in 344 days), and hydrographs H3 to H7 represent each year by 23 days (688 days above half of the 2-year flow in 30 years). In all, we tested 7 hydrographs (Figure 4.5), all of which were simulated with same debris flow sediment initial conditions, and with 2 different grain size distributions of the debris flow sediment inputs (B(finer) and A(coarser) of Figure 4.2b).

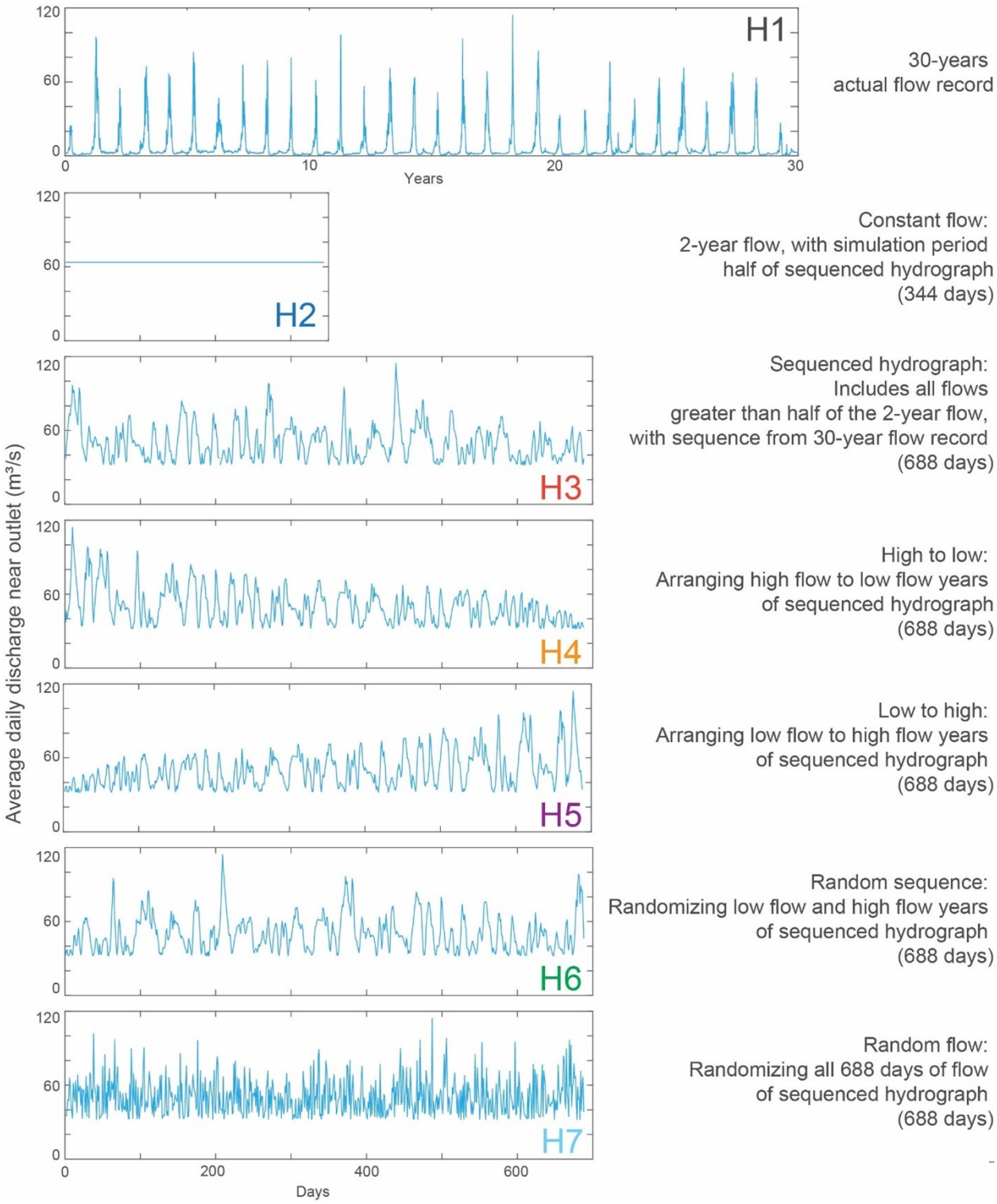

Figure 4.5: Construction of different hydrographs: H1 to H7. The discharge values are shown for USGS gage 10155000. The arranging of H4-H6 take average one-year segments of H3 when reordering/rearranging.

4.4.4 Spatial Debris Flow Input Distribution to the Network

This modeling opportunity was utilized to explore the effects of the spatial distribution of debris flow inputs on its transport through the network and downstream impacts. In order to do so, we introduced 30,000 m^3 of debris flow sediment volume each in 6 major tributaries, one at a time. This 30,000 m^3 debris flow sediment volume was equally distributed among 3 upstream links within each major tributary. Each input was added in total, instantaneously to the model at the beginning of the model run (time t = 0) and at the second link from the upstream end (to avoid adding the debris flow sediment in the background sediment supply link). These 18 debris flow links are shown in Figure 4.6, from where 3 nearby links are used at a time to create 6 sets of comparable scenarios under the 2-year constant flow hydrograph scenario (H2, Figure 4.5). The constant 2-year flow was run for 344 days, which is comparable to 30-years of actual flow record (discussed in Section 4.4.3). Additionally, the RUSLE inputs were kept the same as described previously (Section 4.4.1; Figure 4.2c), and the coarser of the two previous debris flow grain sizes was used for all scenarios (GSD A of Figure 4.2b).

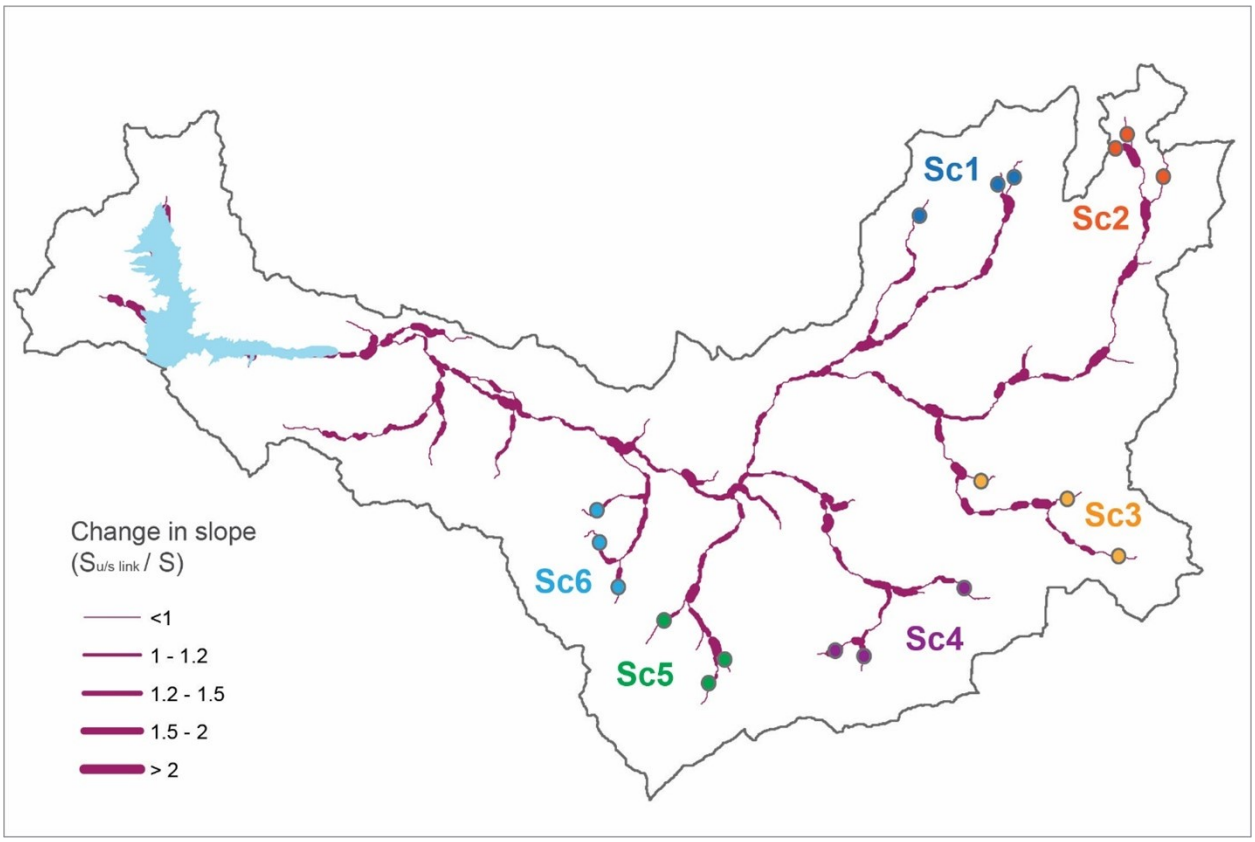

Figure 4.6: Spatial distribution of debris flows inputs under different scenarios: Sc1 to Sc6, input locations are marked by circles. The debris flow volume at each link is 10,000 m^3, and the grain size distribution of the input sediment follows distribution A (from Figure 4.2b). The thickness of each link is showing the ratio: $S_{u/slink}/S$; i.e. relative steepness of immediate upstream link compared to that link.

4.5 Results

4.5.1 Debris Flow Transport under Different Flow Hydrographs

We introduced the same amount of debris flow sediment (with 2 different grain size distributions B (finer) and A (coarser); Figure 4.2) under 7 different comparable flow hydrographs

(H1 to H7; Figure 4.5), and tracked the transport of debris flow sediment input though the network and to the reservoir. We described (in Section 4.4.3) how these flow hydrographs are comparable to 30-year original flow record. That way, we present and compare results in equivalent 30-year period of time.

Total debris flow sediment transport through the network was described as a fraction of the total debris flow sediment input that reached the reservoir. First, the total transport (fraction of the total debris flow sediment volume in reservoir) under different hydrographs (H1 to H7) are shown for 2 different debris flow grain sizes (78% sand and 25% sand; GSDs B and A in Figure 4.2b, respectively) in Figure 4.7. The result from the original 30-year daily flow record (H1) is shown with a dotted black line, and errors are calculated from the results of the H1 simulation (the 30-year daily hydrograph). The general pattern of total transport shows that most (>60%) of the material was transported to reservoir within 5 years (Figure 4.7a & 4.7c).

For the finer debris flow, the debris flow sediment transport by the constant 2-year flow (H2) approaches H1 at around 10 years, but for the coarser debris flow, it did not fully converge to H1 after 30 years (Figure 4.7a & 4.7c). Although the transport (from H2) was nearly the same at around 10 years for the coarser debris flow (Figure 4.7c, d), H1 resulted in increased transport during the high flow period (15-20 years in H1 hydrograph of Figure 4.5). The interesting finding is that in both cases (fine and coarse debris flow) the highest transport occurred from H5, where the yearly flow segments were arranged from low to high flow. The early low flows were enough to rework the finest fraction of the debris flow sediment volume, whereas later high flows were able to more efficiently move the coarse material. The H6 (randomized years) and H7 (randomized days) hydrographs also transported more debris

flow sediment than the 30-year daily hydrograph (H1). These two hydrographs also had more of the low flows early on and more high flows after 2-5 years (Figure 4.5). Movement

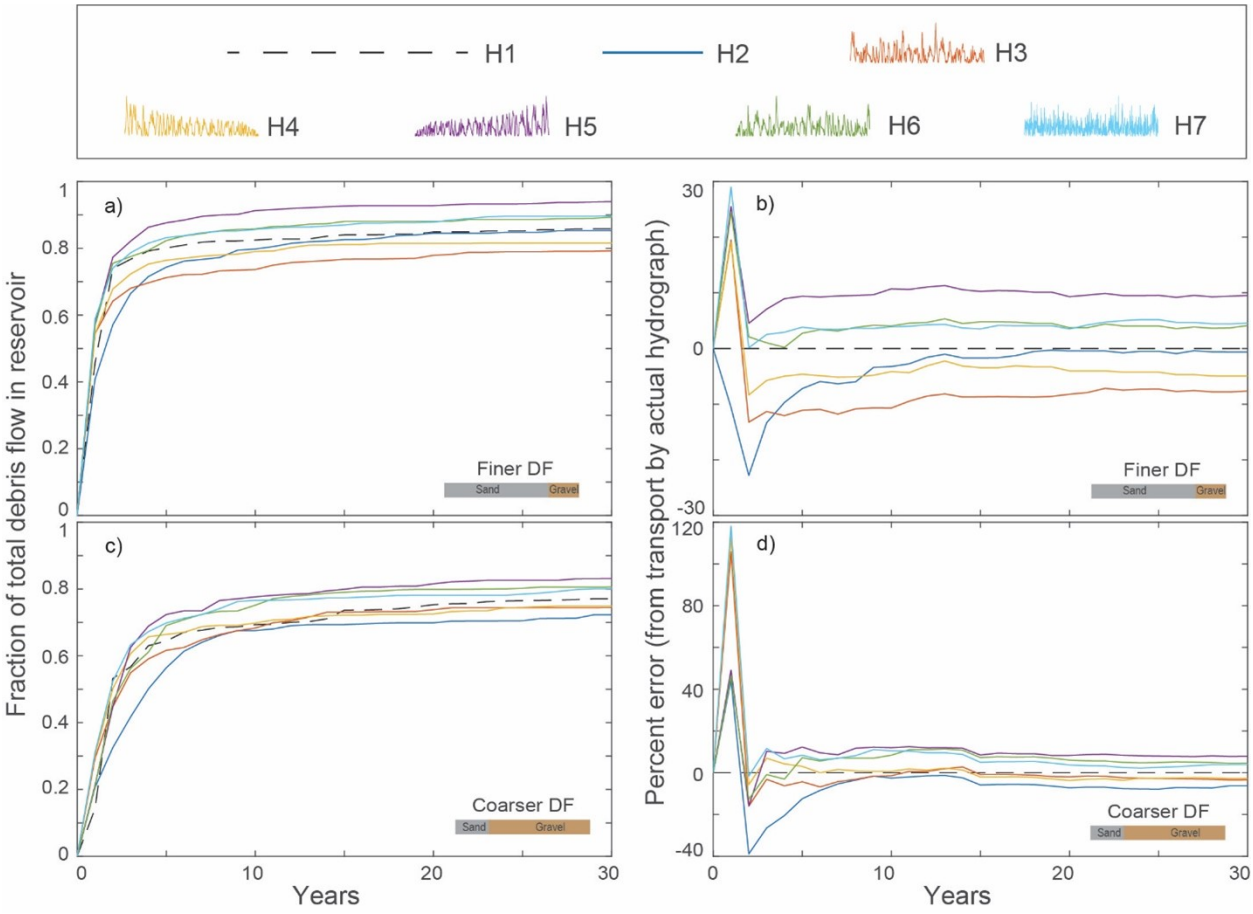

Figure 4.7: Debris flow sediment transported by all hydrographs (H1 to H7) and corresponding error from transport by H1. a) & b) Transport and error for finer debris flow input (grain size distribution B, Figure 4.2b), c) & d) Transport and error for coarser debris flow input (grain size distribution A, Figure 4.2b)

of finer debris flow sediment by H3 and H4 were lower than H1 (Figure 4.7a). The H3 hydrograph preserved the sequence of the original hydrograph (H1), and started with a comparatively high flow and without the initial low flows of H1. The H4 hydrograph was arranged from high to low flow years, with almost all of the transport occurring during the

early high flows and very little transport after 12 years (Figure 4.7a). The calculated error for the total finer debris flow sediment transport for all hydrographs was within ±10% from 30-year daily hydrograph H1 at the end of the 30 years (even after around 10 years; Figure 4.7b). The percentage errors were high in the first 5 years, and highest in the first two years, although the magnitude of the error in volume was under 30% for the finer debris flows. The main difference was due to the specific flows in the first few years of the simulation because they can be quite variable from simulation to simulation.

For the coarser debris flows, early high flows (H3 and H4) transported debris flow sediment more similarly to H1, in contrast to the simulated results from the fine debris flows (Figure 4.7c, d). The error within the first few years was also much higher (up to 120%) than for the finer debris flows because fewer of the lower flows could adequately transport this sediment (Figure 4.7c, d). The constant 2-year flow (H2) transported the least amount of the coarse debris flow sediment in 30 years, but overall the calculated error for total transport for all hydrographs was still within ±10% from the 30-year daily hydrograph H1 after 10 years (Figure 4.7d).

We disaggregated the results of Figure 4.7 into 2 size classes: sand (< 2 mm, Figure 4.8) and gravel (> 2 mm, Figure 4.9). The sand fraction of the debris flow sediment volume transported followed a similar pattern as the total debris flow sediment transported. All hydrographs except H2 transported more than the 30-year daily hydrograph H1 when the debris flow input was coarse and sand volume was low (Figure 4.8c, d). This highlights that the sequence of flows (initial high/low flow) was less important for sand transport in small quantities because any of the flows of the reduced hydrographs ($>0.5Q_2$) were capable of transporting this sand.

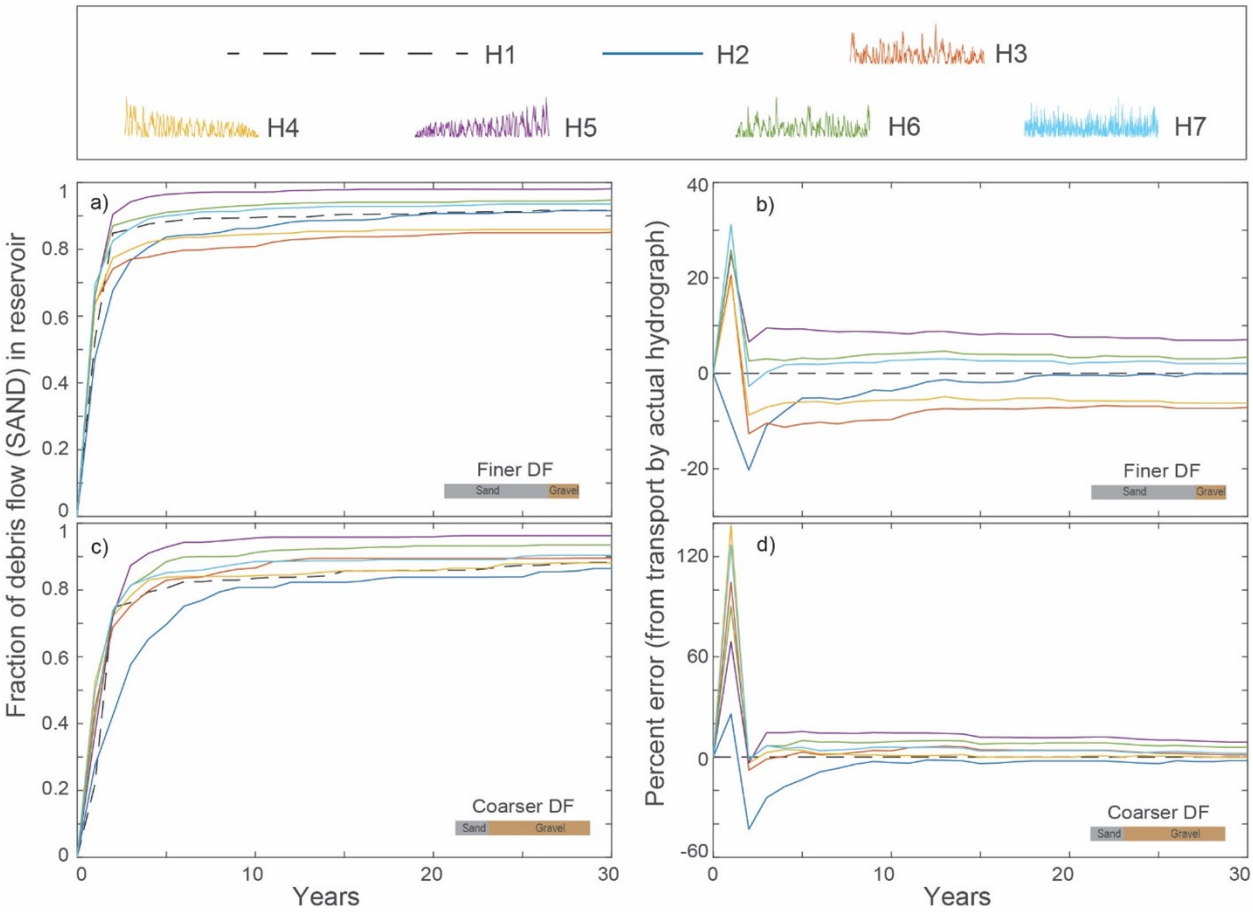

Figure 4.8: Sand fraction of the debris flow sediment transported by all hydrographs (H1 to H7) and the corresponding error from transport by H1. a) & b) Transport and error for finer debris flow input (grain size distribution B, Figure 4.2b), c) & d) Transport and error for coarser debris flow input (grain size distribution A, Figure 4.2b).

The gravel fraction of the debris flow sediment volume transported, however, shows more variability as the transport curves (of Figure 4.9) were comparatively less smooth than of the total or the sand fraction (Figure 4.7 and 4.8, respectively). This highlights the sensitivity of gravel transport to high flows, which are critical to move this coarse material. For the low to high flow hydrograph (H5), the early low flows moved more of the sand while the high flows were preserved for gravels later on. As a result, the rate of change of sediment arrival to the reservoir was greatest for H5 from 10 to 30 years, compared to

other hydrographs (Figure 4.9 a, c). This effect, however, was less with the coarser debris flow inputs. Figure 4.9c shows that largest amount of gravel transport following the coarser debris flow sediment input was accomplished by the H6 hydrograph, where high flows were well distributed (Figure 4.5). The highest flow occurred at around 10 years in this case (H6) after early sand transport out of the network (Figure 4.9c), and the remaining gravel fraction of the debris flow sediment acted as a finer tail in the existing bed that could be translated easily by subsequent high flows.

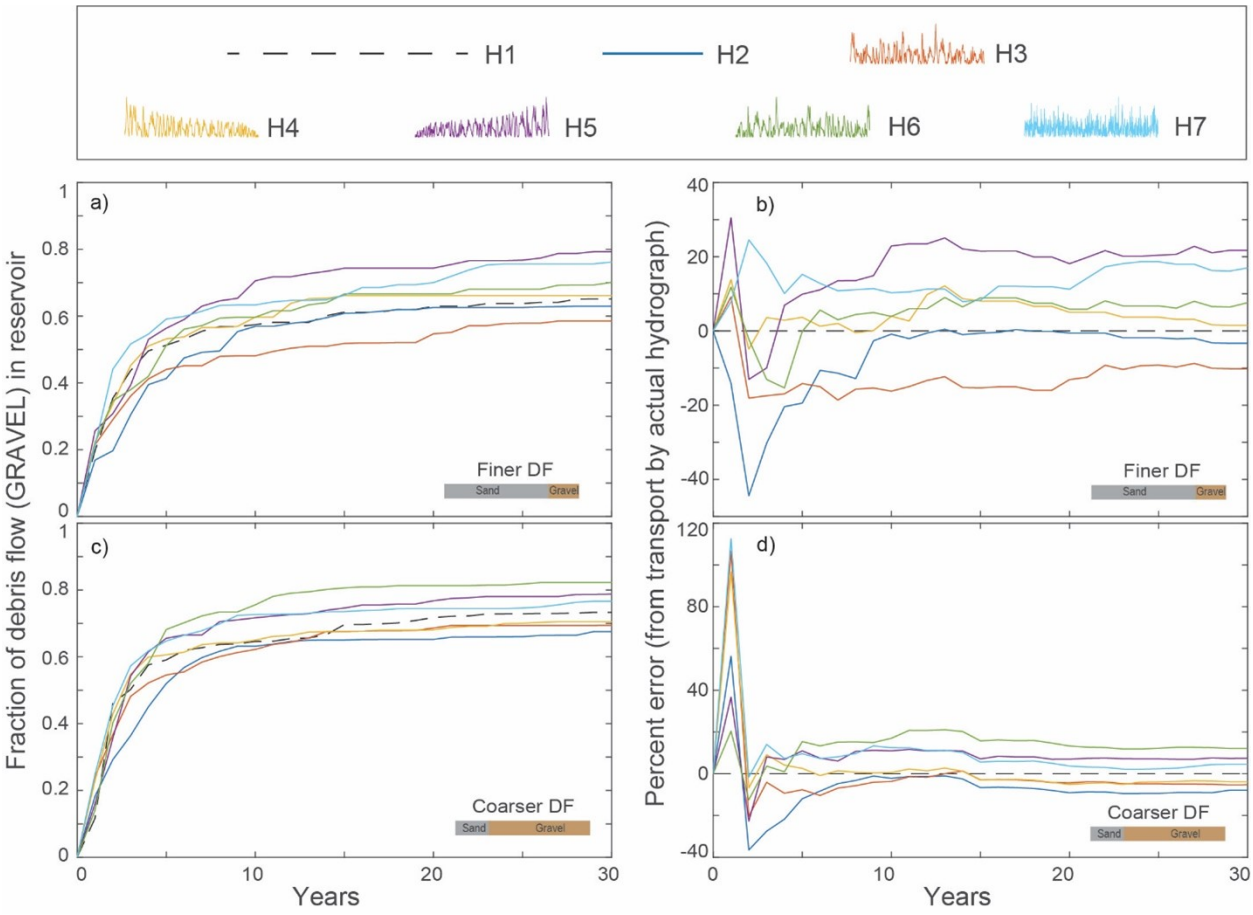

Figure 4.9: Gravel fraction of debris flow sediment transported by all hydrographs (H1 to H7) and corresponding error from transport by H1. a) & b) Transport and error for finer debris flow input (grain size distribution B, Figure 4.2b), c) & d) Transport and error for coarser debris flow input (grain size distribution A, Figure 4.2b).

Another important point of comparison is how each of these hydrographs alter the bed grain size distribution. We focus on the overall bed at three different locations in the network (shown in Figure 4.1), that integrates the background sediment in addition to the debris flow sediment inputs under different hydrographs of H1 to H7. As an example of the time-series data summarized in subsequent figures, we first show the fluctuations of median bed grain size over the simulation period at three locations for two of the seven hydrographs (Figure 4.10). Since the hydrographs do not have the same simulation timesteps, it is difficult to intercompare the resulting timeseries among these hydrographs (H1 to H7) to explore the variation over time. Therefore, we instead report the 20^{th}, 50^{th} and 80^{th} percentile values of any metric over time.

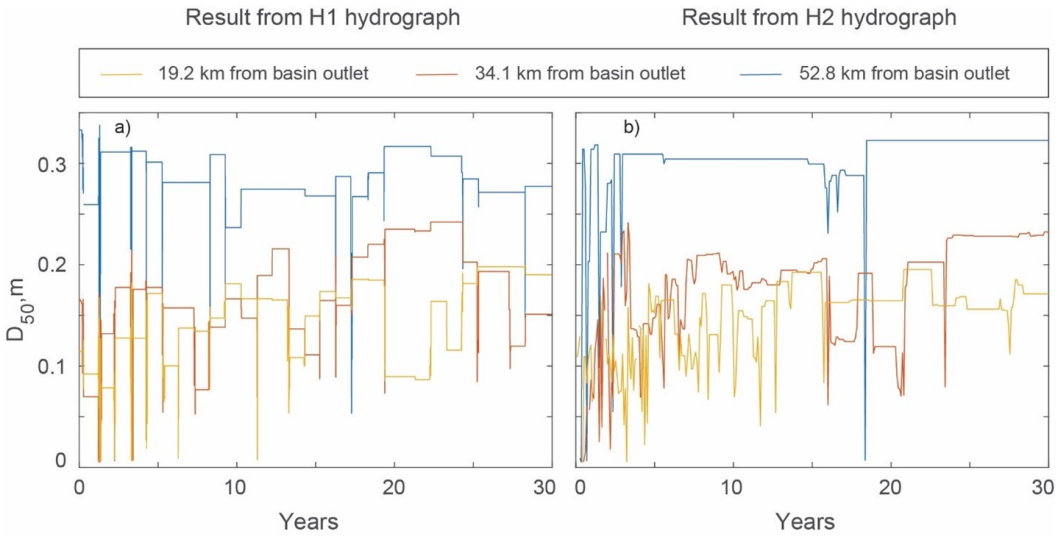

Figure 4.10: Example timeseries of median bed grain size over the simulation period for H1 and H2 hydrographs (with finer debris flow).

To explore the bed response in three different locations (upstream, middle, downstream; Figure 4.1), we looked at bed grain sizes (D_{16}, D_{50}, D_{84}), sand fraction, and sediment depth. We do not compare across locations as because there may be some local effects (of their nearby links) that interact with the effect of different hydrographs. For the finer debris

flow sediment input, bed grain sizes and their variation are comparable for all hydrographs (Figure 4.11g, h, i). Note that the time series shown in Figure 4.10 are represented as the D_{50} points and associated vertical lines of H1 and H2 in panels g, h, and i of Figure 4.11. The resulting D_{16} values from different hydrographs at the upstream location (Figure 4.11i) vary in different ranges. This is likely the result of the sensitivity of this link to the initial sand load at the immediately upstream link from the RUSLE input (Figure 4.2a). The sand fraction goes to zero at the upstream link when the hydrographs had early high flows (H1, H3, H4, H7 in Figure 4.11f). Since this debris flow sediment input contained 78% sand, the sand fraction is closely related to the sediment depth as well (Figure 4.11a-f).

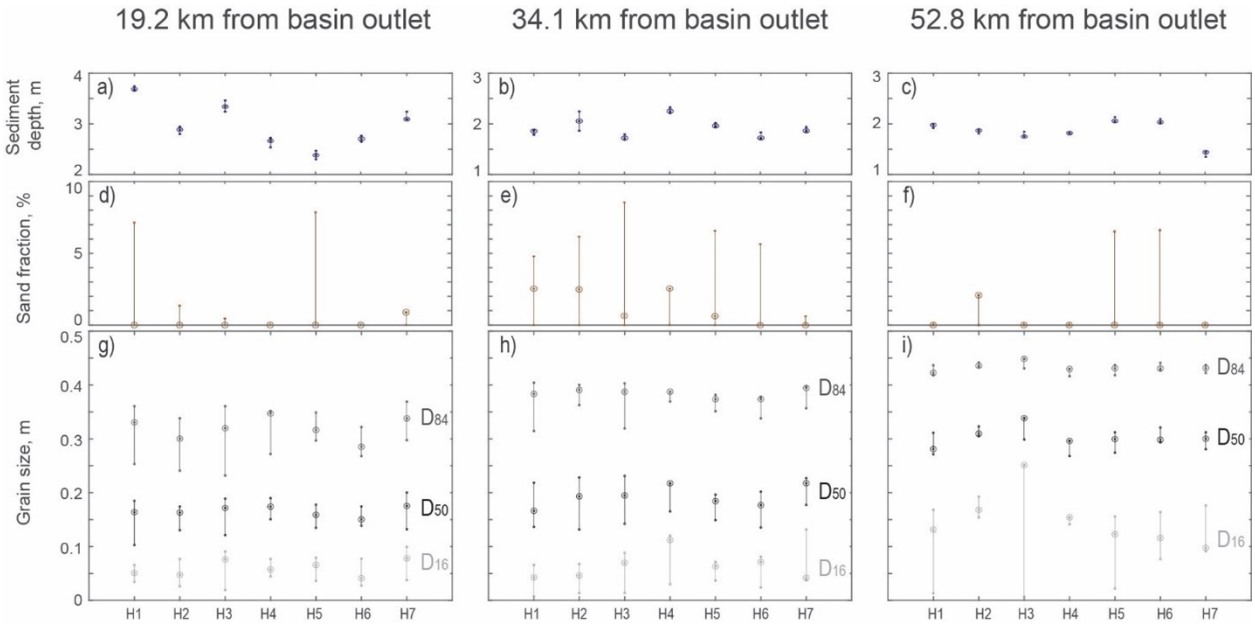

Figure 4.11: Variation in bed grain size (D_{16}(light gray), D_{50}(black), D_{84}(dark gray); in bottom row), sand fraction (middle row), and bed depth (top row) over the simulation period by all hydrographs at three different locations in the network (locations in Figure 4.1) with the finer (GSD B, Figure 4.2b) debris flow sediment input. The vertical lines connect the 80-percentile and 20-percentile values, while the 50-percentile values over time are shown by a circle.

Similar to the finer debris flow, there were some discrepancies among the resulting D_{16} values at the upstream location by different hydrographs (Figure 4.12i). Otherwise, all grain sizes were comparable and varied within a similar range (Figure 4.2g, h, i). Hydrograph H4 (high to low) and H5 (low to high) always produced inverse (to one another) results in terms of sediment depth (Figure 4.11a-c & 4.12a-c). Thus, it seems that the overall bed depth was sensitive to the sequence of flow.

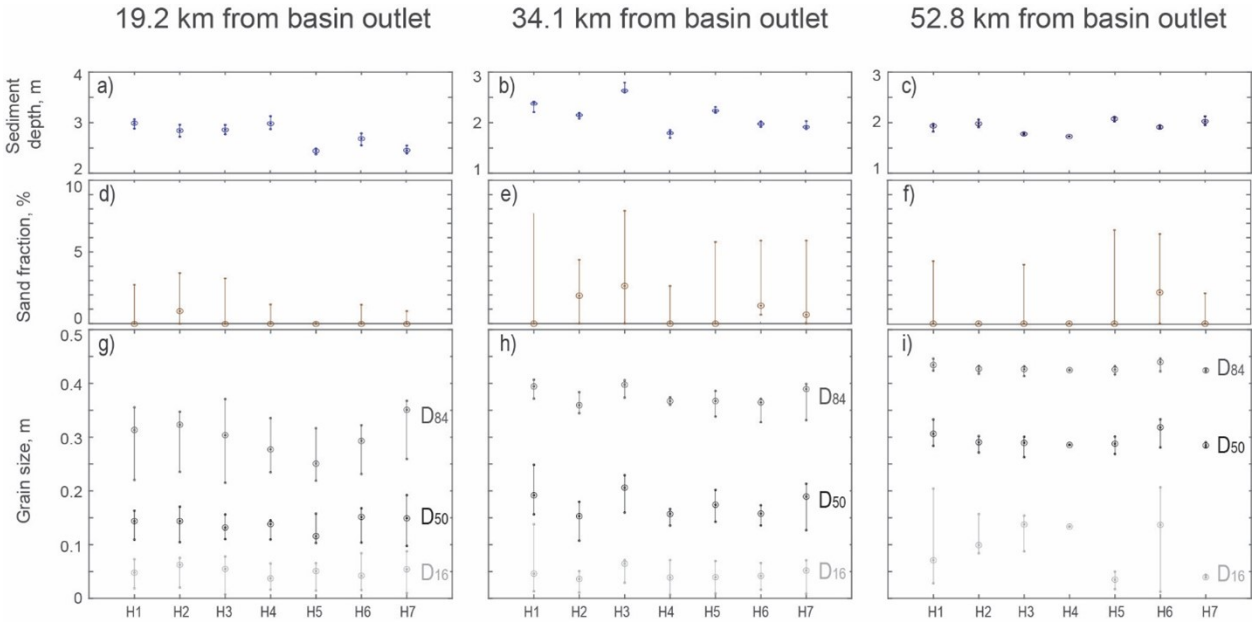

Figure 4.12: Variation of bed grain size (D_{16}(light gray), D_{50}(black), D_{84}(dark gray); in bottom row), sand fraction (middle row), and bed depth (top row) over the simulation period by all hydrographs at three different locations in the network (locations in Figure 4.1) with the coarser (GSD A, Figure 4.2b) debris flow sediment input. The vertical lines connect the 80-percentile and 20-percentile values, while the 50-percentile values over time are shown by a circle.

4.5.2 Debris Flow Transport under Different Spatial Distributions

The same volume of coarse debris flow sediment input was systematically provided to six

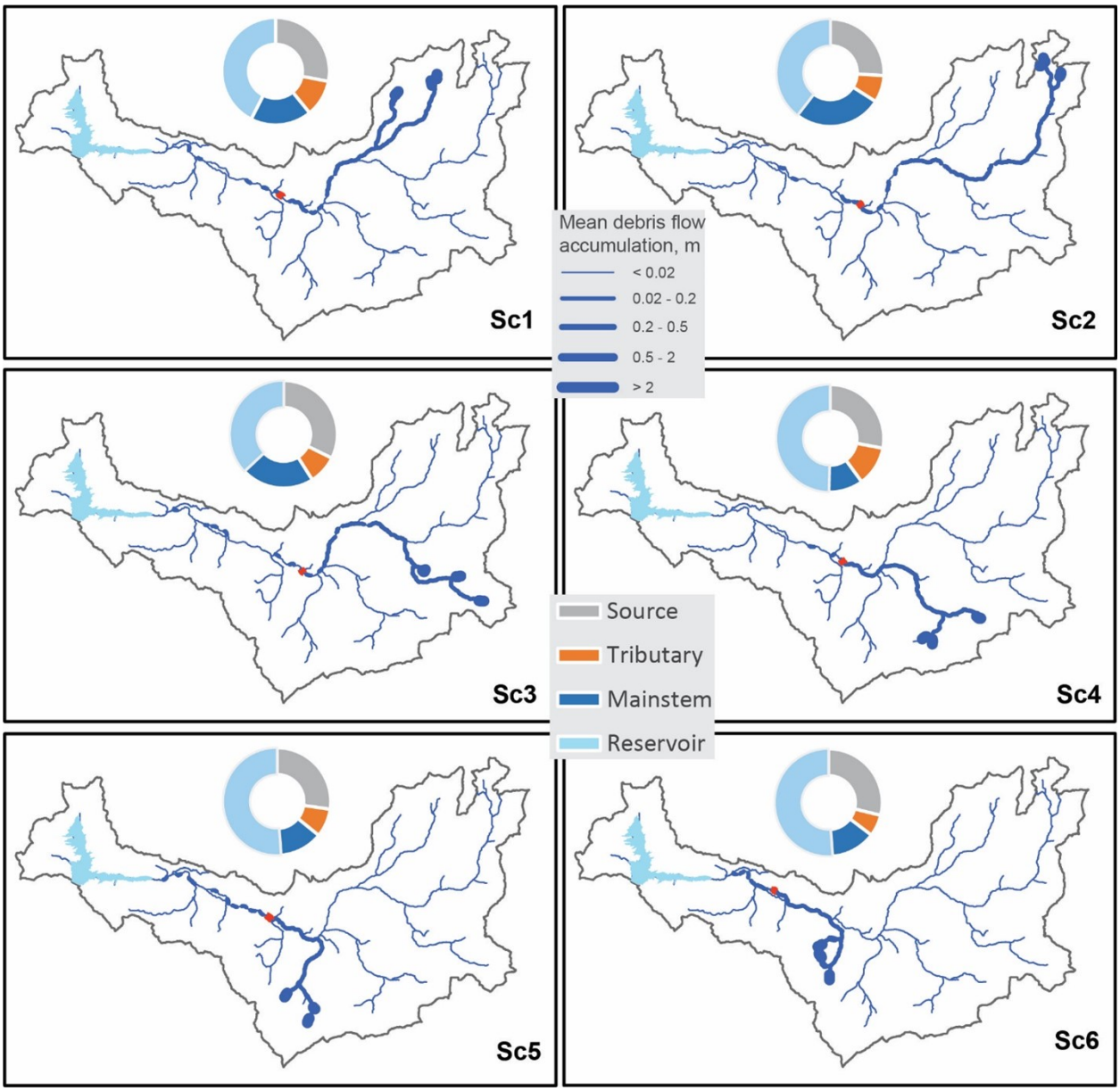

Figure 4.13: Debris flow accumulation in network after the equivalent 30-yr flow simulation under different spatial input distributions (Sc1 to Sc6; Figure 4.6). The proportions of storage in the source location, tributary, mainstem and reservoir are shown by different colors in the circle. The downstream extent of 50% mainstem accumulation is showed by red mark in mainstem for each case.

major tributaries, and the resulting debris flow sediment accumulation after the equivalent

30-yr flow simulation in the Provo River network upstream of the Jordanelle Reservoir is shown in figure 4.13. These spatial plots show that significant portions of the input were not dislodged from their initial links for all scenarios (thickest blue line; Figure 4.13). Another major portion was deposited within the tributary, which was true for all scenarios as well. Overall, 37% (Sc3) to 51% (Sc6) of the initial 30,000 m^3 of debris flow sediment input was transported to the reservoir after the 30-year simulation (Figure 4.14a). Conversely, Figure 4.14b shows the arrival time of different percentages of the input volume to the reservoir. Because the arrival time is inversely related to the total transported volume arriving in the reservoir, we found that Sc3 had the longest arrival time, and Sc6 has the shortest. Further insight can be gain by comparing these results to the network characteristics.

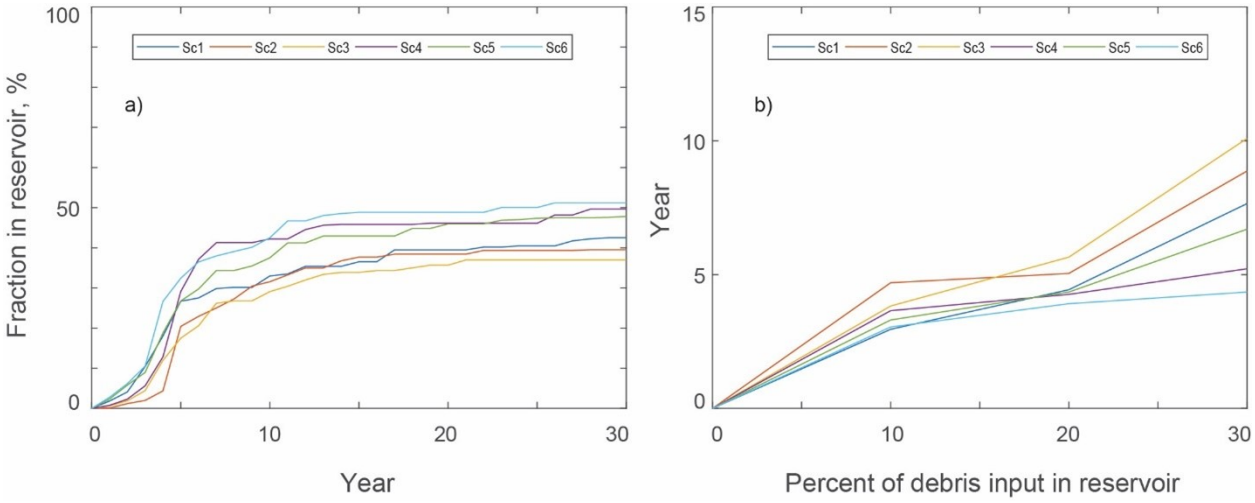

Figure 4.14: Debris flow sediment transport under six different spatial distributions of input volume. a) Fraction of input in reservoir over time, b) Time required to accumulate different percentages (10%, 20% and 30%) of the input debris flow sediment volume within the reservoir.

We investigated different network characteristics to explore which ones had the most control over debris flow sediment transport through the network. These network properties

included the ratio of the tributary basin area and the mainstem basin area at the confluence (symmetry ratio, A_R), average mainstem slope (mean slope of all links from the confluence of that tributary with the mainstem, downstream along the mainstem to the reservoir), ratio of average tributary slope and average mainstem slope (slope ratio= $S_{tributary}/S_{mainstem}$), mainstem length (sum of all link lengths from the confluence of that tributary with the mainstem, downstream along the mainstem to the reservoir), normalized average change in mainstem slope ($S_{upstream\ link}/S_{link}$, normalized by mainstem length), normalized (by mainstem length) inverse slope ratio ($S_{mainstem}/S_{tributary}$), product of symmetry ratio and average tributary slope ($A_R \times S_{tributary}$), and ratio of the product of the average slope and basin area of tributary and mainstem ($(DA \times S)_{tributary}/ (DA \times S)_{mainstem}$), which is the normalized product of the symmetry ratio and average tributary slope ($A_R \times S_{tributary}$) where normalizing was done by average mainstem slope. These network characteristics were selected to isolate individual tributary impacts on transport, some of which had been explored in previous studies (Rice, 2017).

To identify the role of any particular tributary, previous studies discussed tributary-driven aggradation that mainly causes significant change in the slope, morphology, and bed sediment characteristics in the mainstem (Benda et al., 2004a; Rice, 2017). We investigated this mainstem aggradation from two approaches, stored sediment volume and spatial length of deposition. We excluded the stored sediment volume at the input location (at the most upstream) after 30 years, and calculated the delivery to the mainstem (i.e., stored in the network and reservoir) from the rest of the volume. Again, to quantify the extent of any tributary impact on the mainstem, we took the length from the confluence downstream along the mainstem to the reservoir up to the location where 50% of the mainstem storage occurred.

We plotted this tributary delivery and extent of tributary impact against network properties in Figure 4.15 and 4.16, respectively. The normalized inverse slope ratio shows the most definite pattern as tributary delivery increases with this ratio (Figure 4.15e). That is, where the mainstem slope is more similar in slope to its tributaries, the tributary delivers sediment to the mainstem more efficiently. Sc-3, which is an intermediate location (in terms of mainstem length) among the six scenarios, deviates slightly from this trend. It may be caused by the two-consecutive bends in the network immediately after this confluence (Figure 4.13). There is strong control of symmetry ratio (drainage area ratio of tributary and mainstem) over the tributary delivery as well if we set aside scenario Sc-2. Sc-2 is a unique case here as it constitutes almost a straight linear network, where tributary and mainstem drainage area is nearly the same at the confluence (Figure 4.13). Delivery from tributaries decreases with increase of symmetry ratio for the other five tributaries (Figure 4.15a, f, g) because of the increase of tributary sizes (length and width) that yield more tributary storage rather than delivery.

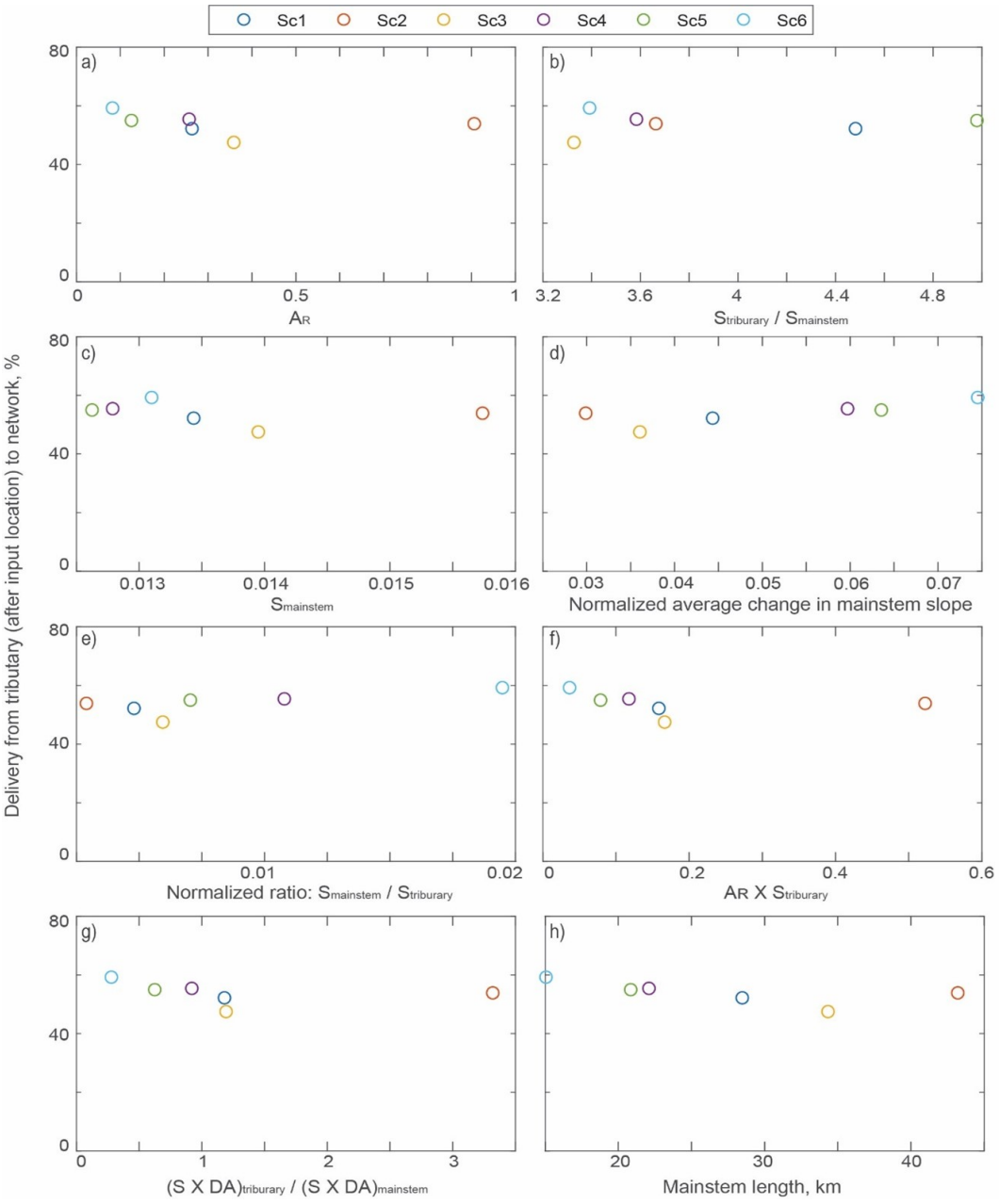

Figure 4.15: Comparison of the tributary delivery (inputs from six different tributaries, Sc1 to Sc6, one at a time) with network properties. Percentage of input sediment (excluding the input location, gray area in Figure 4.13) delivered to mainstem after the 30-year simulation against a) symmetry ratio (A_R= $DA_{tributary}$ /$DA_{mainstem}$), b) slope ratio ($S_{tributary}/S_{mainstem}$), c) mainstem slope, d) average change in mainstem slope normalized by mainstem length., e) inverse slope ratio normalized by mainstem length., f) product of symmetry ratio and tributary slope, g) normalized (by mainstem slope) product of symmetry ratio and tributary slope, and h) mainstem length.

While in terms of mainstem extent of 50% aggradation (i.e., from confluence up to the location where majority of the mainstem aggradation occur), the dominant controlling factor in the mainstem slope property (Figure 4.16c, d). The aggradation extent increases with an increase in average mainstem slope (Figure 4.16c) as the channel can then transport easily, and distribute the sediment more evenly in the network. But the effect of average change in mainstem slope (relative steepness of immediate upstream link to any link) is inverse (Figure 4.16d). The increase in normalized average change in mainstem slope indicates flatness of each link relative to its upstream link as the mainstem progresses to the outlet. As a result, with increased reduction of slope, the mainstem tends to aggrade near the supply (i.e., the confluence here). Although the extent is less, but the depth of accumulation would not be necessarily lower in such cases (Figure 4.6, 4.13).

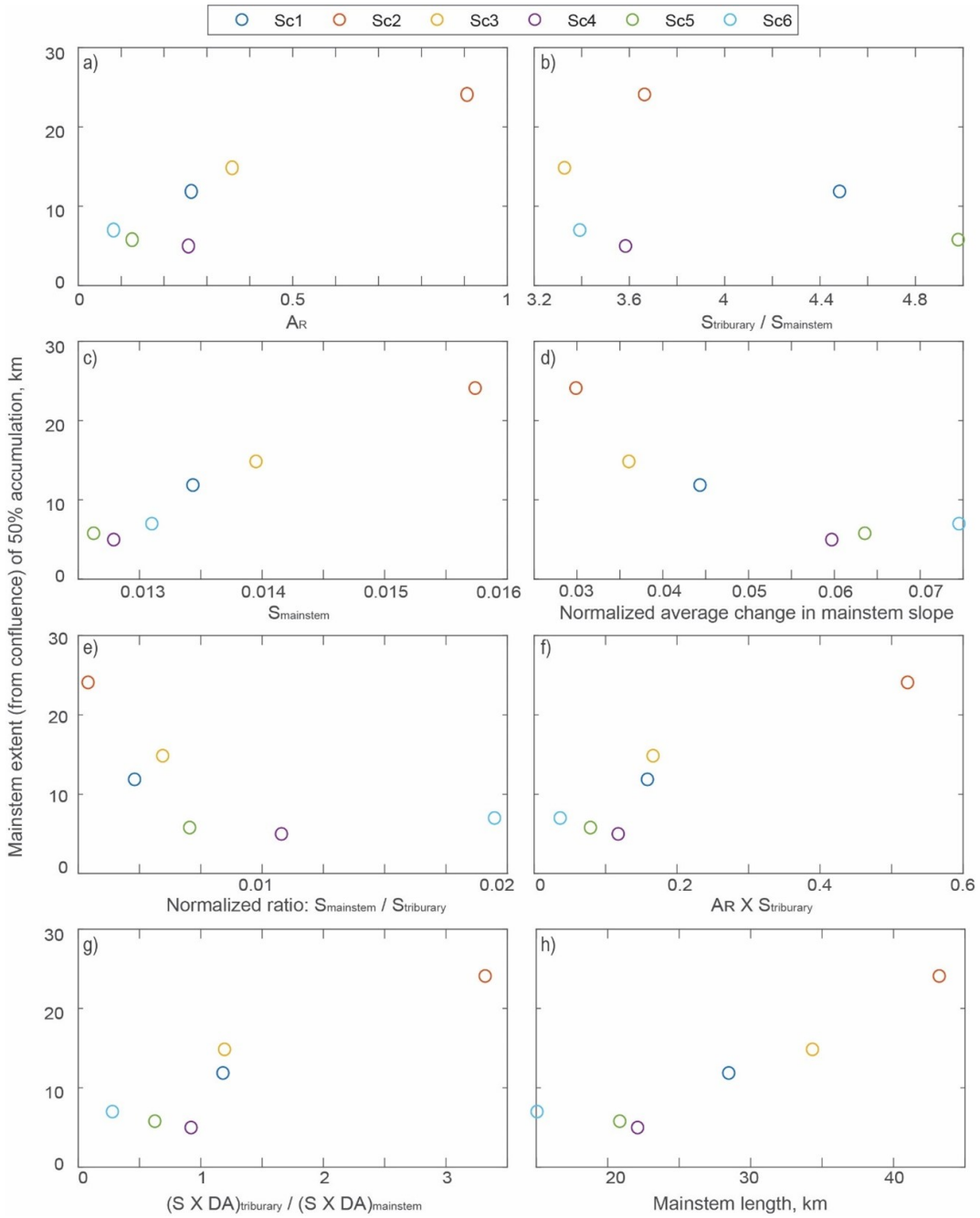

Figure 4.16: Comparison of the aggradation extent in mainstem (inputs from six different tributaries, Sc1 to Sc6, one at a time) with network properties. Length along the mainstem from confluence where 50% of mainstem storage occurred (downstream extent is shown in Figure 4.13) after the 30-year simulation against a) symmetry ratio (A_R= $DA_{tributary}$ /$DA_{mainstem}$), b) slope ratio ($S_{tributary}/S_{mainstem}$), c) mainstem slope, d) average change in mainstem slope normalized by mainstem length., e) inverse slope ratio normalized by mainstem length., f) product of symmetry ratio and tributary slope, g) normalized (by mainstem slope) product of symmetry ratio and tributary slope, and h) mainstem length.

The total debris flow sediment volume transported to the reservoir as a percentage of its input is plotted against these network properties in figure 4.17. The scatter plots show pattern similar to Figure 4.15, with stronger control of normalized average change in mainstem slope on total transport (Figure 4.17d). Thus, the total delivery to the reservoir is governed by the combined effects of slope and drainage area of mainstem and tributary. Although our expectation was that the slope ratio would be a critical parameter as discontinuity of slope can facilitate aggradation. Instead, distance from the reservoir showed a more defined pattern (Figure 4.17h), where more sediment arrived when the debris flow sediment had to travel a shorter distance. Again, since this distance has obvious correlation with the amount transported (shorter distances cause higher transport in Sc-4 & 6; Figure 4.17b), we plotted total transport against the normalized inverse slope ratio (Figure 4.17d). This normalization was physically meaningful since the inverse slope ratio ($S_{mainstem}$ /$S_{tributary}$) reduces as it nears the reservoir.

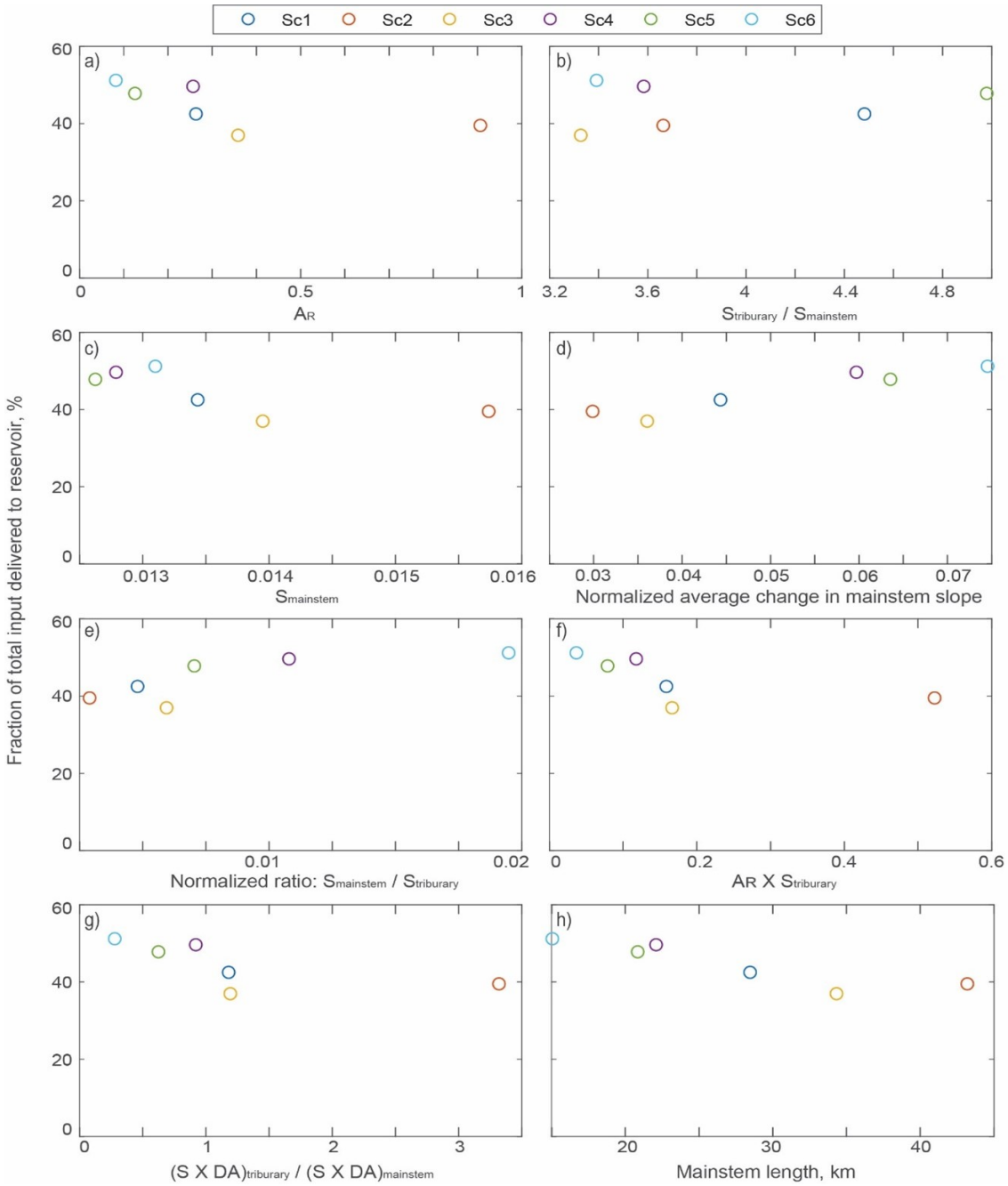

Figure 4.17: Comparison of the total debris flow sediment transported (inputs from six different tributaries, Sc1 to Sc6, one at a time) with network properties. Percentage of input to reservoir after the 30-year simulation against a) symmetry ratio (A_R= $DA_{tributary}$ /$DA_{mainstem}$), b) slope ratio ($S_{tributary}/S_{mainstem}$), c) mainstem slope, d) average change in mainstem slope normalized by mainstem length., e) inverse slope ratio normalized by mainstem length., f) product of symmetry ratio and tributary slope, g) normalized (by mainstem slope) product of symmetry ratio and tributary slope, and h) mainstem length.

However, the plot (Figure 4.17d) of normalized inverse slope ratio showed the pattern that the amount transported increases with the comparative steepness of mainstem slope to tributary slope. That is, where the mainstem slope is more similar in slope to its tributaries, transport is more efficient and more sediment is transported to the reservoir. Again, due to local effects, Sc-3 shows slight discrepancy from this trend. Conversely, Figure 4.18 shows plots of the travel time of 30% of the input debris flow sediment volume against all these attributes, which is essentially an inverse plot of Figure 4.17, but provides insight into the time for debris flow sediment to reach the reservoir.

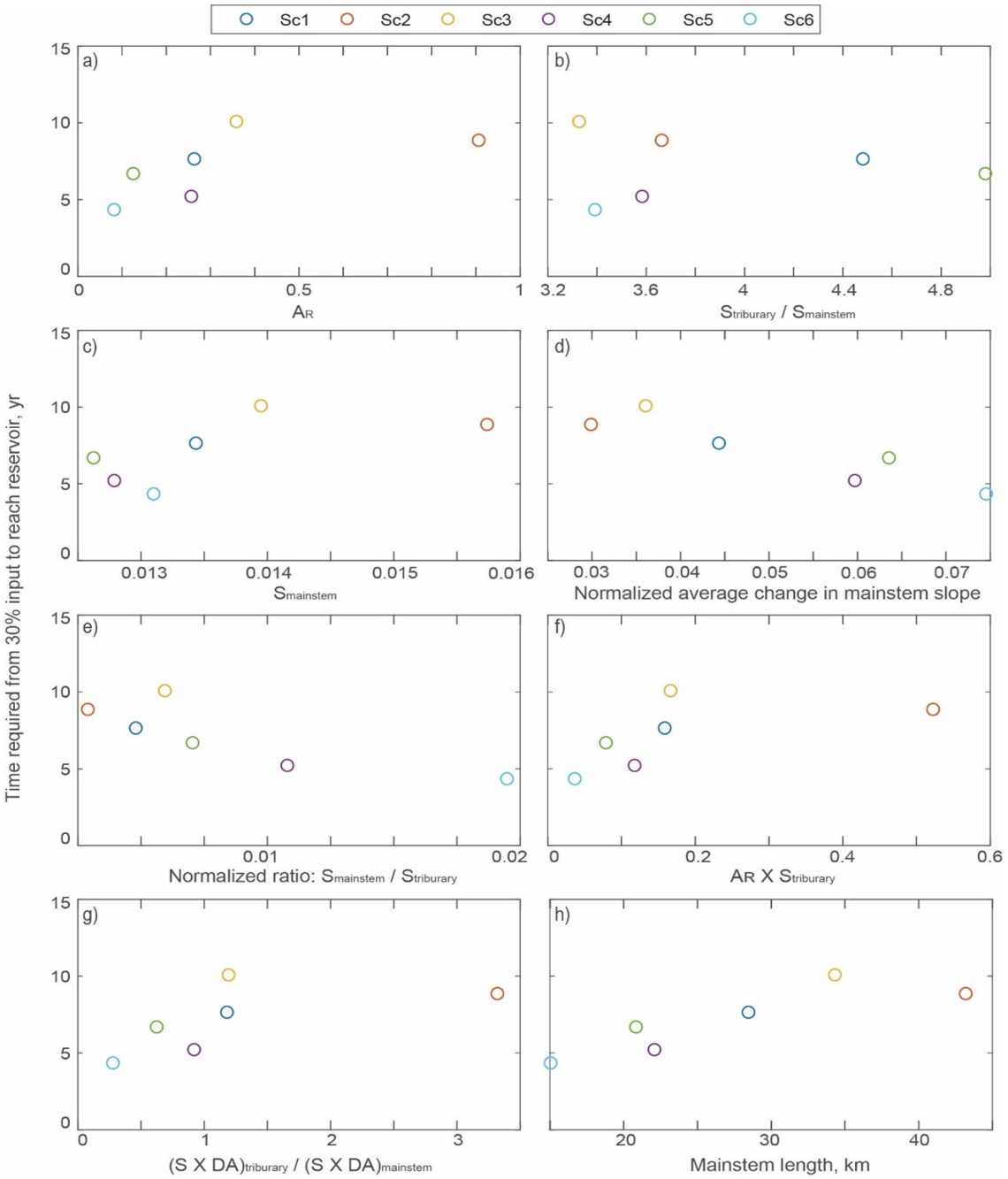

Figure 4.18: Comparison of the required time for 30% of the input debris flow sediment volume to arrive at the reservoir (inputs from six different tributaries, Sc1 to Sc6, one at a time) with network properties. Travel time of 30% of the input debris flow sediment volume to arrive at the reservoir against a) symmetry ratio (A_R= $DA_{tributary}$ /$DA_{mainstem}$), b) slope ratio ($S_{tributary}/S_{mainstem}$), c) mainstem slope, d) average change in mainstem slope normalized by mainstem length., e) inverse slope ratio normalized by mainstem length., f) product of symmetry ratio and tributary slope, g) normalized (by mainstem slope) product of symmetry ratio and tributary slope, and h) mainstem length.

4.6 Discussion

4.6.1 Hydrologic Control

The 2-year recurrence interval flow is often used as an approximation for the bankfull discharge, but the threshold for motion of mean bed sediment size tends to occur at flows below the bankfull discharge (Parker, 1978). We expect half of the 2-year flow magnitude should be sufficient to move deposits of debris flow sediment that have grain-sizes much smaller than that of bed. Thus, we synthesized our hydrographs from the long-term flow record based on a threshold of half of the 2-year flow (Figure 4.5). The duration of reduced hydrographs (H3-H7) equals the number of days flow exceeded this threshold in the 30-year daily flow record. The reduced hydrographs (H3-H7) have flows above and below the 2-year flow, so we assumed that sediment transporting flows would be available, on average half of its (H3-H7) duration. Again, with the absence of exact magnitude of sediment transporting flow, we ran the constant 2-year flow for half of the duration of reduced hydrographs (H3-H7). As a result, 1 year of actual record was translated in 11.5 and 23 days by H2 and H3-H7, respectively. This type of simplified approach is not uncommon to understand long-term sediment transport by reducing computational efforts (intermittency factor; Czuba & Foufoula-Georgiou, 2014; Paola, 1992; Parker, 2004), but the effect of simplifying the hydrograph in this way has not been suitably analyzed (as we have done here).

The comparison between the 30-year daily and reduced hydrographs suggest that the results (in terms of debris flow sediment transport) are comparable in long-term simulations for both sand and gravel-dominated pulses (error within $\pm 10\%$; Figure 4.7). The initial error

is larger for the gravel-dominated pulse, while the error reduces after 10 years for both types of pulses. The actual number of flows in the reduced hydrographs (H3-H7) was less than the original flow record of equivalent years. As a result, H2 with the shortest duration had a corresponding error that took the longest to converge. Moreover, the magnitude of the final error after an equivalent 30-year period was much less for sand-dominated pulses compared to gravel-dominated pulses (0.6% vs. 6%; Figure 4.7 b, d). This shows the importance of high flow events (higher than 2-year flow) to move coarse gravels from the system, and efficiency of comparatively lower flows for sand removal (Church & Gilbert, 1975; Bogen, 1980; Walling & Webb, 1987; Asselman, 1999).

Flow sequences matter at short timescales (e.g., Humphries et al., 2012; Guney et al., 2013; Phillips et al., 2018; Waters & Curran 2015), but at longer timescales this sequencing becomes less important. However, going from high flow years to low flow years, the H4 hydrograph consistently produced low long-term transport (similar effect from H3 as well that starts with high flow). This demonstrates that an early high-magnitude event can strongly affect the transport of a subsequent low-magnitude flood (Mao, 2018; Dudill et al., 2017). The H5 hydrograph caused maximum transport (except where the pulse was coarse gravel, Figure 4.9c) and as the sediment-transporting flows increased in magnitude and frequency, the sediment-transport capacity of the rivers also increased, and moved more debris flow sediment (Cui & Parker, 2005; Ahammad et al., 2021). Our simulation results highlight that the sequence of flows (initial high/low flow) was less important for transport of fines because any of the flows of the reduced hydrographs ($>0.5Q_2$) were capable of transporting this sediment.

The movement of debris flow sediment pulses was strongly translational because its grain size distribution was much finer than the bed (Ahammad et al., 2021; Cui & Parker,

2005; Lisle, 2008; Lisle et al., 1997, 2001; Sklar et al., 2009). Model results showed that this translational effect decreases as the grain-size distribution of the debris flow sediment increases (steeper transport curves in initial 5 years for Figure 4.7a than Figure 4.7c). Importantly, all hydrographs showed similar responses to the different debris flow grain-size distributions (Figure 4.7 - 4.9). All hydrographs show systematic reduction in bed grain-size as the location neared the downstream outlet (Figure 4.11, 4.12). The overall impact on the bed of different debris flow sediment grain-size distributions was similar between the 30-year daily and reduced hydrographs as the bed depth and all grain sizes varied within a similar range (Figure 4.11, 4.12).

4.6.2 Network control

In a systematic test of the same debris flow sediment volume and grain-size distribution, from the upstream most location of tributaries, we were able to investigate the sediment transfer processes from each tributary (Rice, 2017). Our work quantified the delivery from each tributary, extent of mainstem aggradation, total transport to the reservoir, and arrival time of sediments to the reservoir to identify controlling factors of tributary-driven mainstem aggradation. In general, tributary influences increased with total network length and drainage area (Figure 4.17h; Benda et al., 2004a; Benda, 2008; Rice, 2017). Tributary driven aggradation generally reduced the slope upstream as the majority of deposition happened in the upstream half of the mainstem (Figure 4.16h). In this way, stored material steepens the channel slope to maintain its sediment transporting capacity (Miller, 1958; Church & Kellerhals, 1978; Rice & Church, 1998, 2001; Benda et al., 2004a; Harmar & Clifford, 2006). Empirical models utilizing field studies suggest that symmetry ratio and tributary caliber

(product of drainage area and slope) are key surrogate metrics to predict tributary delivery to mainstem (Knighton, 1980; Rice 1998, 2017; Benda et al., 2004a). Our analysis agreed with and confirmed these expectations (Figure 4.15a, f). Our model results also showed that tributary steepness compared to mainstem alone did not predict transport from the tributary to the mainstem, because of the importance of other parameters like length, width, bed material grain-size, etc. (which can be scaled by drainage area) on transport (Figure 4.15b, 4.16b, 4.17b, 4.18b; Ferguson & Hoey, 2008; Ferguson et al., 2006; Rice et al., 2006). However, when the mainstem slope was more similar in slope to its tributaries, transport was more efficient and more sediment was transported to the reservoir (Figure 4.17e).

Our model also captured geomorphic impacts of local network pattern (i.e., accumulation in links), through the reduction in slopes locally (lower transport in Sc-3; Figure 4.17e). In addition to quantitatively identifying geomorphologically significant tributaries, we, therefore, introduced another strong predictor for transport through the mainstem. The slope change (steepness of upstream link compared to any link) maps the mean debris flow sediment accumulation very closely (Figure 4.6, 4.13). Simulations showed that mainstem aggradation extent largely depended on mainstem slope characteristics (average mainstem slope, and average change in mainstem slope, normalized by mainstem length; Figure 4.16c, d).

4.7 Summary

Debris flow sediment routing in a 650 km^2 river network was simulated in this work to explore hydrologic and network control on sediment transport. An updated river network

model based on Czuba (2018) and Murphy et al. (2019) was applied in the Provo River network upstream of the Jordanelle Reservoir (in Northern Utah) to test two independent hypotheses. First, simplifying a flow hydrograph to use in model simulations should result in major differences at short timescales, but these differences were expected to be less substantial at longer timescales. This study found that differences between transport by 30-year daily hydrograph and simplified hydrograph were greatest in the first few years, but errors decreased to around 10% after 10 years.

Our second hypothesis was that, the same debris flow sediment input can result in different downstream effects, such as delivery and mainstem aggradation, based on the debris flow sediment input location. We used the model to quantitatively test relevant network characteristics for efficient transport from tributaries. Results were supported by findings from previous studies that the symmetry ratio was important to detect significant tributaries. We found that relative steepness of the immediately upstream link to any location, has the potential to highlight aggradation of that location, and thus, throughout the network. While the introduced quantification of the extent of mainstem aggradation, model results showed that it was mainly a function of mainstem slope characteristics. However, to predict aggradation from these network characteristics more confidently, more widespread (in several other river networks) model application with field validation would be useful.

The use of compressed and simple hydrographs can optimize computational efforts greatly. Results from these flow scenarios on sediment transport at different timescales is helpful to river managers as it highlights that network responses to any event in short timescale are mostly unpredictable because it depends a lot on the specific flows that occur, but after 5-10 years, the delivery is more predictable as more of the variability is averaged

over. The results of network characteristics are important, because they suggest how differences in input locations can aggrade the network and reservoir in different ways. These predictions of debris flow sediment accumulation can help inform management of post-wildfire landscapes. Moreover, tributary-driven confluence aggradation, through sediment connectivity, are often key controls of habitat heterogeneity in stream networks. Thus, our results have implication for river biodiversity and cumulative ecosystem health as well.

Chapter 5

Conclusion

While a sustainable environment requires proper functioning of watersheds to provide clean water and to sustain a productive and diverse ecosystem, water managers are facing challenges of increasing population and changing climate. Although sediment is a naturally occurring component of our environment, humans are arguably the most important geomorphic agent currently shaping the surface of the Earth today by causing accelerated erosion through agricultural activities, urbanization, forest activities, infrastructure, river regulation etc. (Hooke, 1994). With increasing awareness of potential consequences of sedimentation processes, scientific studies require consideration of watershed-scale processes associated with sediment sources, transport routes, and depositional sinks, as well as the potential future effects on the environment. Time-lags delay the arrival of sediment eroded from landscapes and transported through river systems to downstream ecosystems, which is one primary focus of management interventions (Pizzuto et al., 2014). A thorough understanding of sediment sources, transport, fate, and delivery is therefore necessary for effective management actions with a goal of decreasing negative impacts of sediment loads. Recent advances in data collection techniques have substantially increased both the resolution and spatial scale of data on sediment dynamics, which is helpful in linking small, site-scale measurements of transport processes in the field with large-scale modeling efforts. Herein, this thesis presents guidance for site-scale measurement, along with sediment transport dynamics in river networks from its source to sink.

Applied to the techniques of suspended sediment measurement (by LISST-SL2) and dynamics of bed-material sediment on river networks, this research has produced the following main results:

1. We collected a comprehensive dataset of 136 LISST-SL2 samples along with 65 physical samples for SSC measurement and 24 physical samples for PSD measurement during 2018-2020 from 11 sites in Washington and Virginia, USA. These sites drain area of different physiographic settings, ranging from 57 to 7500 km^2, and provide suitable conditions for testing the LISST-SL2. The best-fit value for computed effective density was 1.99 g/mL and ranged from 0.4 to 5.8 g/mL, across a wide range of suspended sediment concentration (SSC_M: 12 - 4,364 mg/L).

2. Our results highlight the need for a correction of the raw LISST-SL2 measurements to improve the estimation of effective density and PSD with the help of a physical sample. By doing so, we showed how this would increase the accuracy (via RMSRE) of SSC from 117% to 24% and D_{50} from 78% to 49%.

3. We advanced a river network model (of Czuba, 2018) for bed material transport by adding components for stress partitioning, initial bed sediment initialization, background supply and link-capacity partitioning. We applied the updated model in a linear network of the Nisqually River, Washington, and compared our model results against available field measurements.

4. Channel incision may occur instead of aggradation when sediment pulse volume is relatively small and pulse grain size is finer than the bed.

5. Intermediate grain size sediment pulses have the largest downstream effects; finer sizes translate quickly and coarser sizes disperse slowly.

6. A mixed-size sediment pulse with smaller median grain size than the bed increases bed mobility more than a uniform-size sediment pulse.

7. With a better understanding from model application for sediment pulse movement through a linear network, we have applied the 1-D Lagrangian model for debris flow sediment routing in the Provo River network (of northern Utah) to explore hydrologic and network control on sediment transport. This river network has a number of tributaries, which allows us to examine complex transport and network processes.

8. This study found that differences between transport by the 30-year daily hydrograph and simplified hydrographs were greatest in the first few years, but errors decreased to around 10% in the long-term.

9. Our simulation results highlight that the sequence of flows (initial high/low flow) was less important for transport of finer sediment because any of the flows of the simplified hydrographs (all flows were greater than half of the 2-year flow) were capable of transporting this sediment.

10. We used the model to quantitatively test relevant network characteristics for efficient transport from tributaries. Results were supported by findings from previous studies that the symmetry ratio was important to detect significant tributaries. We found that relative steepness of the immediately upstream link to any location, has the potential to highlight aggradation of that location, and thus, throughout the network.

The guidance provided by this study will facilitate more reliable and effective data collection by the LISST-SL2 in the future. We emphasize on more detailed microscopic analysis of the suspended material should be performed for assessing particle shape and surface characteristics. It can provide further insight into the causes that are responsible

for the varying computed effective densities resulted in this study. Given the fact that the laser diffraction method can continuously measure suspended sediment by grain size, and allows us to better understand the temporal characteristics of sediment transport in fluvial environments, improving the accuracy and consistency of suspended sediment measurements by laser diffraction will help revolutionize fluvial sediment monitoring. The LISST-SL2, specifically, has great potential to study the spatial and temporal variation of suspended sediment concentration and grain-size distribution arising from turbulence and sediment supply.

While applying the river network model, this study only focused on the one-dimensional aspects of sediment-pulse evolution, but the spatial complexity of rivers can influence patterns of sediment-pulse evolution (Kasprak et al., 2015; Nelson & Dubé, 2016; Recking et al., 2016). Local or reach-scale topography can affect how sediment pulses are transported through a reach and affect how well bedload equations developed from flume studies translate to field scale (Recking et al., 2016). Sediment pulses tend to accumulate on point bars and their growth can modify flow patterns and lead to more active channel migration (Humphries et al., 2012; Parker et al., 2011). Additionally, sediment can fill pools or locally deposit behind large woody debris, further complicating sediment-pulse evolution (Harrison et al., 2018; Major et al., 2012; Ryan et al., 2014; Wohl & Scott, 2017). The model used in this study does not currently consider time-varying channel width, and the interactions among bank supply, bed structure, and lateral sediment exchange. Along with incorporating these components, the inclusion of a sand transport equation would make the model more robust in simulating the transport of combined gravel and sand mixtures, particularly in cases where bed sand fraction is high (>10%).

Even with confidence in the inputs, network connectivity, and reach-scale dynamics,

there are challenges of verifying whether the modeled emergent behavior actually exists at the watershed scale. Unfortunately, very few basins have uninterrupted, long-term sediment delivery data to facilitate this kind of model validation (Garcia, 2008). Although the current model produced expected results that are comparable to other studies and field observations, more directly testing an updated model against field data sets would provide a robust validation of sediment-pulse movement in rivers. In time, a detailed sensitivity analysis of parameters related to hydro-geomorphic properties is suggested. It will allow us to better parameterize this modeling framework, and present model results with a confidence bound.

REFERENCES

Agrawal, Y. C., and H. C. Pottsmith (1994), Laser diffraction particle sizing in STRESS, *Cont. Shelf Res., 14*(10–11), 1101– 1121, doi:10.1016/0278-4343(94)90030-2.

Agrawal, Y. C., and H. C. Pottsmith (2000), Instruments for particle size and settling velocity observations in sediment transport, *Mar. Geol., 168*, 89– 114, doi:10.1016/S0025-3227(00)00044-X.

Agrawal, Y. C., McCave, I. N. and J. B. Riley, J. B. (1991), Laser diffraction size analysis, in *Principles, Methods and Application of Particle Size Analysis*, edited by J. M. P. Syvitski, pp. 119– 128, Cambridge Univ. Press, N. Y.

Agrawal, Y. C., & Mikkelsen, O. (2019), Sediments in river columns- particle size distribution and concentrations measured with a LISST-SL2 isokinetic instrument. *E-proceedings of the 38th IAHR World Congres*s, Panama City, Panama.doi:10.3850/38WC092019-1767

Agrawal, Y. C., and Traykovski, P. (2001), Particles in the bottom boundary layer: Concentration and size dynamics through events, *J. Geophys. Res., 106*(C5), 9533– 9542, doi:10.1029/2000JC900160.

Agrawal, Y. C., Whitmire, A., Mikkelsen, O. A., & Pottsmith, H. C. (2008). Light scattering by random shaped particles and consequences on measuring suspended sediments by laser diffraction. *Journal of Geophysical Research: Oceans, 113*(C4), doi: 10.1029/2007JC004403.

Ahammad, M., Czuba, J. A., Pfeiffer, A. M., Murphy, B. P., & Belmont, P. (2021). Simulated Dynamics of Mixed Versus Uniform Grain Size Sediment Pulses in a Gravel-Bedded River. *Journal of Geophysical Research: Earth Surface, 126*(10), e2021JF006194.

American Public Health Association, American Water Works Association, Water Pollution Control Federation, & Water Environment Federation. (1912). *Standard methods for the examination of water and wastewater*(Vol. 2). American Public Health Association.

An, C., Cui, Y., Fu, X., & Parker, G. (2017). Gravel-bed river evolution in earthquake-prone regions subject to cycled hydrographs and repeated sediment pulses. *Earth Surf. Process. Landforms, 42*(14), 2426–2438. https://doi.org/10.1002/esp.4195

Andrews, S., Nover, D., & Schladow, S. G. (2010). Using laser diffraction data to obtain accurate particle size distributions: the role of particle composition. *Limnology and Oceanography: Methods, 8*(10), 507-526, doi: 10.4319/lom.2010.8.507.

Anderson, S., & Pitlick, J. (2014). Using repeat lidar to estimate sediment transport in a steep stream. *J. Geophys. Res. Earth Surf., 119*(3), 621–643. https://doi.org/10.1002/2013JF002933

Arnaud, F., Piégay, H., Béal, D., Collery, P., Vaudor, L., & Rollet, A. J. (2017). Monitoring gravel augmentation in a large regulated river and implications for process-based restoration. *Earth Surface Processes and Landforms, 42*(13), 2147-2166. https://doi.org/10.1002/esp.4161

Asselman, N. E. M. (1999), Suspended sediment dynamics in a large drainage basin: The River Rhine. *Hydrol. Processes, 13*(10), 1437–1450.

Ashworth, P. J., & Ferguson, R. I. (1989). Size-selective entrainment of bed load in gravel bed streams. *Water Resources Research, 25*(4), 627-634. https://doi.org/10.1029/WR025i004p00627

Bellmore, J. R., Duda, J. J., Craig, L. S., Greene, S. L., Torgersen, C. E., Collins, M. J., & Vittum, K. (2017). Status and trends of dam removal research in the United States. *Wiley Interdisciplinary Reviews: Water, 4*(2), e1164. https://doi.org/10.1002/wat2.1164

Benda, L., & Dunne, T. (1997a). Stochastic forcing of sediment supply to channel networks from landsliding and debris flow. *Water Resources Research, 33*(12), 2849-2863. https://doi.org/10.1029/97WR02388

Benda, L., & Dunne, T. (1997b). Stochastic forcing of sediment routing and storage in channel networks. *Water Resources Research, 33*(12), 2865-2880. https://doi.org/10.1029/97WR02387

Benda, L. (2008). *Confluence environments at the scale of river networks* (pp. 271-300). John Wiley & Sons: Chichester, UK.

Benda, L. E., & Cundy, T. W. (1990). Predicting deposition of debris flows in mountain channels. *Canadian Geotechnical Journal, 27*(4), 409-417.

Benda, L. E. E., Andras, K., Miller, D., & Bigelow, P. (2004a). Confluence effects in rivers: interactions of basin scale, network geometry, and disturbance regimes. *Water Resources Research, 40*(5). https://doi.org/10.1029/2003WR002583

Benda, L. E. E., Poff, N. L., Miller, D., Dunne, T., Reeves, G., Pess, G., & Pollock, M. (2004b). The network dynamics hypothesis: how channel networks structure riverine habitats. *BioScience, 54*(5), 413-427.

Blott, S. J., Croft, D. J., Pye, K., Saye, S. E., & Wilson, H. E. (2004). Particle size analysis by laser diffraction. *Geological Society, London, Special Publications, 232*(1), 63-73, doi: 10.1144/GSL.SP.2004.232.01.08.

Bogen, J. (1980), The hysteresis effect of sediment transport systems, *Nor. Geogr. Tidsskr., 34*, 45–54.

Bombar, G., Elçi, Ş., Tayfur, G., Güney, M. Ş., & Bor, A. (2011). Experimental and numerical investigation of bed-load transport under unsteady flows. *Journal of Hydraulic Engineering, 137*(10), 1276-1282.

Bracken, L. J., Turnbull, L., Wainwright, J., & Bogaart, P. (2015). Sediment connectivity: a framework for understanding sediment transfer at multiple scales. *Earth Surface Processes and Landforms, 40*(2), 177-188.

Bradley, J. B., & Hadley, H. R. (2014). Impacts of the Mount St. Helens Eruption on the Columbia and Cowlitz Rivers and the Corps' Response to Date. In *World Environmental and Water Resources Congress 2014* (pp. 1128-1137).

Cashman, M. J., Gellis, A. C., Boyd, E., Collins, M. J., Anderson, S. W., McFarland, B. D., & Ryan, A. M. (2021). Channel response to a dam-removal sediment pulse captured at high-temporal resolution using routine gage data. *Earth Surface Processes and Landforms, 46*(6), 1145-1159. https://doi.org/10.1002/esp.5083

Castro-Bolinaga, C. F., Diplas, P., & Bodnar, R. J. (2020). Modeling Hydro-Morphodynamic Processes During the Propagation of Fluvial Sediment Pulses: A Physics-Based Framework. *Journal of Geophysical Research: Earth Surface, 125*(12), e2020JF005722. https://doi.org/10.1029/2020JF005722

Castro, J. (1995). *Effects of sediment on the aquatic environment: potential NRCS actions to improve aquatic habitat*(No. 6). US Department of Agriculture, Soil Conservation Service.

Cavalli, M., Trevisani, S., Comiti, F., & Marchi, L. (2013). Geomorphometric assessment of spatial sediment connectivity in small Alpine catchments. *Geomorphology, 188*, 31-41.

Church, M., and R. Gilbert (1975), Proglacial fluvial and lacustrine environments, glaciofluvial and glaciolacustrine sedimentation, *Spec. Publ. Soc. Econ. Paleontol. Minerol., 23*, 40–100.

Church, M., & Kellerhals, R. (1978). On the statistics of grain size variation along a gravel river.*Canadian Journal of Earth Sciences, 15*(7), 1151-1160.

Chen, H. X., Zhang, L. M., Zhang, S., Xiang, B., & Wang, X. F. (2013). Hybrid simulation of the initiation and runout characteristics of a catastrophic debris flow. *Journal of Mountain Science, 10*(2), 219-232.

Copeland, E. A. (2009). Recent periglacial debris flows from Mount Rainier, Washington, M.S. thesis, Oregon State University, Corvallis, Oregon.

Crandell, D. R. (1971). *Postglacial lahars from Mount Rainier volcano*, Washington. US Geological Survey Professional Paper 677, 75 p.

Cui, P., Hu, K., Zhuang, J., Yang, Y., & Zhang, J. (2011). Prediction of debris-flow danger area by combining hydrological and inundation simulation methods. *Journal of Mountain Science, 8*(1), 1-9.

Cui, Y. (2007). The unified gravel-sand (TUGS) model: Simulating sediment transport and gravel/sand grain size distributions in gravel-bedded rivers. *Water Resour. Res., 43*, W10436. https://doi.org/10.1029/2006WR005330

Cui, Y., Collins, M. J., Andrews, M., Boardman, G. C., Wooster, J. K., Melchior, M., & McClain, S. (2019). Comparing 1-D sediment transport modeling with field observations: Simkins Dam removal case study. *International Journal of River Basin Management, 17*(2), 185-197. https://doi.org/10.1080/15715124.2018.1508024

Cui, Y., & Parker, G. (2005). Numerical model of sediment pulses and sediment-supply disturbances in mountain rivers. *Journal of Hydraulic Engineering, 131*(8). https://doi.org/10.1061/(ASCE)0733-9429(2005)131:8(646)

Cui, Y., Parker, G., Braudrick, C., Dietrich, W. E., & Cluer, B. (2006a). Dam removal express assessment models (DREAM). Part 1: Model development and validation. *Journal of Hydraulic Research, 44*(3). https://doi.org/10.1080/00221686.2006.9521683

Cui, Y., Parker, G., Braudrick, C., Dietrich, W. E., & Cluer, B. (2006b). Dam removal express assessment models (DREAM). Part 2: Sample runs/sensitivity tests. *Journal of Hydraulic Research, 44*(3). https://doi.org/10.1080/00221686.2006.9521684

Cui, Y., Parker, G., Lisle, T. E., Gott, J., Hansler-Ball, M. E., Pizzuto, J. E., Allmendinger, N. E., & Reed, J. M. (2003a). Sediment pulses in mountain rivers: 1. Experiments. *Water Resour. Res., 39*(9), 1239. https://doi.org/10.1029/2002WR001803

Cui, Y., Parker, G., Pizzuto, J., & Lisle, T. E. (2003b). Sediment pulses in mountain rivers: 2. Comparison between experiments and numerical predictions. *Water Resour. Res., 39*(9), 1240. https://doi.org/10.1029/2002WR001805

Cui, Y., & Wilcox, A. (2008). Development and application of numerical models of sediment transport associated with dam removal, in *Sedimentation engineering: Processes, measurements, modeling, and practice, American Society of Civil Engineers manuals and reports on engineering practice*, no. 110, edited by M. H. Garcia, pp. 995-1020, ASCE, Reston, Virginia.

Cui, Y., Wooster, J. K., Braudrick, C. A., & Orr, B. K. (2014). Lessons learned from sediment transport model predictions and long-term postremoval monitoring: Marmot Dam removal project on the Sandy River in Oregon. *Journal of Hydraulic Engineering, 140*(9), 04014044. https://doi.org/10.1061/(ASCE)HY.1943-7900.0000894

Curran, C. A., Grossman, E. E., Magirl, C. S., & Foreman, J. R. (2016). *Suspended sediment delivery to Puget sound from the lower Nisqually River, Western Washington, July 2010–November 2011* (No. 2016-5062). US Geological Survey.

Czuba, C. R., Randle, T. J., Bountry, J. A., Magirl, C. S., Czuba, J. A., Curran, C. A., & Konrad, C. P. (2011). *Anticipated sediment delivery to the lower Elwha River during and following dam removal*. US Department of the Interior, US Geological Survey.

Czuba, J. A. (2018). A Lagrangian framework for exploring complexities of mixed-size sediment transport in gravel-bedded river networks. *Geomorphology, 321*, 146-152. https://doi.org/10.1016/j.geomorph.2018.08.031

Czuba, J. A., Czuba, C. R., Magirl, C. S., & Voss, F. D. (2010). *Channel-conveyance capacity, channel change, and sediment transport in the lower Puyallup, White, and Carbon Rivers,*

western Washington. U.S. Geological Survey Scientific Investigations Report 2010–5240, 104 p.

Czuba, J. A., & Foufoula-Georgiou, E. (2014). A network-based framework for identifying potential synchronizations and amplifications of sediment delivery in river basins. *Water Resour. Res., 50*(5), 3826–3851. https://doi.org/10.1002/2013WR014227

Czuba, J. A., Foufoula-Georgiou, E., Gran, K. B., Belmont, P., & Wilcock, P. R. (2017). Interplay between spatially-explicit sediment sourcing, hierarchical river-network structure, and in-channel bed-material sediment transport and storage dynamics. *Journal of Geophysical Research - Earth Surface, 122*(5), 1090-1120. https://doi.org/10.1002/2016JF003965

Czuba, J. A., Magirl, C. S., Czuba, C. R., Curran, C. A., Johnson, K. H., Olsen, T. D., ... & Gish, C. C. (2012a). *Geomorphic analysis of the river response to sedimentation downstream of Mount Rainier, Washington,* U.S. Geological Survey Open-File Report 2012–1242, 134 p. [Available at http://pubs.usgs.gov/of/2012/1242/]

Czuba, J. A., Magirl, C. S., Czuba, C. R., Grossman, E. E., Curran, C. A., Gendaszek, A. S., & Dinicola, R. S. (2011). *Sediment load from major rivers into Puget Sound and its adjacent waters*, U.S. Geological Survey Fact Sheet 2011–3083, 4 p. [Available at http://pubs.usgs.gov/fs/2011/3083/]

Czuba, J. A., Hirschler, M., Pratt, E. A., Villamagna, A., & Angermeier, P. L. (2022). Bankfull shear velocity predicts embeddedness and silt cover in gravel streambeds. *River Research and Applications, 38*(1), 59-68, doi: 10.1002/rra.3878.

Czuba, J. A., Olsen, T. D., Czuba, C. R., Magirl, C. S., & Gish, C. C. (2012b). *Changes in sediment volume in Alder Lake, Nisqually River Basin, Washington, 1945–2011*, U.S. Geological Survey Open-File Report 2012–1068, 30 p. (Available at http://pubs.usgs.gov/of/2012/1068/).

Czuba, J. A., Straub, T. D., Curran, C. A., Landers, M. N., & Domanski, M. M. (2015). Comparison of fluvial suspended-sediment concentrations and particle-size distributions measured with in-stream laser diffraction and in physical samples. *Water Resources Research, 51*(1), 320-340, doi: 10.1002/2014WR015697.

Davis, B. E. (2005), *A guide to the proper selection and use of federally approved sediment and water-quality samplers*, U.S. Geol. Surv. Open File Rep., 2005–1087, 20 pp.(Available at http://pubs.usgs.gov/of/2005/1087/pdf/OFR_2005-1087.pdf).

De Rego, K., Lauer, J. W., Eaton, B., & Hassan, M. (2020). A decadal-scale numerical model for wandering, cobble-bedded rivers subject to disturbance. *Earth Surface Processes and Landforms, 45*(4), 912-927. https://doi.org/10.1002/esp.4784

Dingle, E. H., Attal, M., & Sinclair, H. D. (2017). Abrasion-set limits on Himalayan gravel flux. *Nature, 544*(7651), 471-474. https://doi.org/10.1038/nature22039

Despotovic, M., Nedic, V., Despotovic, D., & Cvetanovic, S. (2016). Evaluation of empirical models for predicting monthly mean horizontal diffuse solar radiation. *Renewable and Sustainable Energy Reviews, 56,* 246-260, doi: 10.1016/j.rser.2015.11.058.

Dow, S., Snyder, N. P., Ouime, W. B., Martini, A. M., Yellen, B., Woodruff, J. D., ... & Walter, R. C. (2020). Estimating the timescale of fluvial response to anthropogenic disturbance using two generations of dams on the South River, Massachusetts, USA. *Earth Surface Processes and Landforms, 45*(10), 2380-2393. https://doi.org/10.1002/esp.4886

Dudill, A., Frey, P., & Church, M. (2017). Infiltration of fine sediment into a coarse mobile bed: a phenomenological study. *Earth Surface Processes and Landforms, 42*(8), 1171-1185.

East, A. E., Logan, J. B., Mastin, M. C., Ritchie, A. C., Bountry, J. A., Magirl, C. S., & Sankey, J. B. (2018). Geomorphic evolution of a gravel-bed river under sediment-starved versus sediment-rich conditions: River response to the world's largest dam removal. *Journal of Geophysical Research: Earth Surface, 123*(12), 3338-3369. https://doi.org/10.1029/2018JF004703

East, A. E., Pess, G. R., Bountry, J. A., Magirl, C. S., Ritchie, A. C., Logan, J. B., ... & Shafroth, P. B. (2015). Large-scale dam removal on the Elwha River, Washington, USA: River channel and floodplain geomorphic change. *Geomorphology, 246*, 687-708. https://doi.org/10.1016/j.geomorph.2014.08.028

Edwards, T. K., and G. D. Glysson (1999), *Field methods for measurement of fluvial sediment,* in Techniques of Water-Resources Investigations of the U.S. Geological Survey: Book 3, Application of Hydraulics, Chap. C2, 89 p., Reston, Va.(Available at http://pubs.usgs.gov/twri/twri3-c2/pdf/TWRI_3-C2.pdf)

Fahnestock, R. K. (1963). *Morphology and hydrology of a glacial stream–White River, Mount Rainier, Washington* (Vol. 422). US Government Printing Office.

Felix, D., Albayrak, I., & Boes, R. M. (2013). Laboratory investigation on measuring suspended sediment by portable laser diffractometer (LISST) focusing on particle shape. *Geo-Marine Letters, 33*(6), 485-498, doi: 10.1007/s00367-013-0343-1.

Ferguson, R., & Hoey, T. (2008). Effects of tributaries on main-channel geomorphology. *River confluences, tributaries and the fluvial network*, 183-208.

Ferguson, R. I., Cudden, J. R., Hoey, T. B., & Rice, S. P. (2006). River system discontinuities due to lateral inputs: generic styles and controls. *Earth Surface Processes and Landforms: The Journal of the British Geomorphological Research Group, 31*(9), 1149-1166.

Ferrer-Boix, C., & Hassan, M. A. (2015). Channel adjustments to a succession of water pulses in gravel bed rivers. *Water Resources Research, 51*(11), 8773-8790.

FISP (1941). *A study of methods used in measurement and analysis of sediment loads in streams*. Report no. 5 [Available at https://water.usgs.gov/fisp/docs/Report_5.pdf]

Flannigan, M. D., Krawchuk, M. A., de Groot, W. J., Wotton, B. M., & Gowman, L. M. (2009). Implications of changing climate for global wildland fire. *International journal of wildland fire, 18*(5), 483-507.

Foley, M. M., Bellmore, J. R., O'Connor, J. E., Duda, J. J., East, A. E., Grant, G. E., ... & Wilcox, A. C. (2017). Dam removal: Listening in. *Water Resources Research, 53*(7), 5229-5246. https://doi.org/10.1002/2017WR020457.

Gaeuman, D., Stewart, R., Schmandt, B., & Pryor, C. (2017). Geomorphic response to gravel augmentation and high-flow dam release in the Trinity River, California. *Earth Surface Processes and Landforms, 42*(15), 2523-2540. https://doi.org/10.1002/esp.4191.

Ganasri, B. P., & Ramesh, H. (2016). Assessment of soil erosion by RUSLE model using remote sensing and GIS-A case study of Nethravathi Basin. *Geoscience Frontiers, 7*(6), 953-961.

García, M. H. (2008), Sediment transport and morphodynamics, chap. 2, in *Sedimentation Engineering: Processes, Measurements, Modeling, and Practice:* ASCE Manuals and Reports on Engineering Practice No.110, edited by M. H. García, pp. 21– 163, ASCE, Reston, Va.

Gartner, J. E., Cannon, S. H., & Santi, P. M. (2014). Empirical models for predicting volumes of sediment deposited by debris flows and sediment-laden floods in the Transverse Ranges of southern California. *Engineering Geology, 176,* 45-56.

Gartner, J. W., R. T. Cheng, P. F. Wang, and K. Richter (2001), Laboratory and field evaluations of LISST-100 instrument for suspended particle size determinations, *Mar. Geol., 175*(1-4), 199– 219, doi:10.1016/S0025-3227(01)00137-2.

Gitto, A. B., Venditti, J. G., Kostaschuk, R., & Church, M. (2017). Representative point-integrated suspended sediment sampling in rivers. *Water Resources Research, 53*(4), 2956-2971, doi: 10.1002/2016WR019187.

Goharian, E., Burian, S. J., Lillywhite, J., & Hile, R. (2017). Vulnerability assessment to support integrated water resources management of metropolitan water supply systems.*Journal of Water Resources Planning and Management, 143*(3), 04016080.

Gray, J. R., & Gartner, J. W. (2009). Technological advances in suspended-sediment surrogate monitoring. *Water Resources Research, 45*(4), doi: 10.1029/2008WR007063.

Gran, K. B., & Czuba, J. A. (2017). Sediment pulse evolution and the role of network structure. *Geomorphology, 277,* 17-30. https://doi.org/10.1016/j.geomorph.2015.12.015

Gray, J., D. Glysson, and T. Edwards (2008), Suspended-sediment samplers and sampling methods, section 5.3, in Sediment transport measurements, chap. 5, edited by P. Diplas et al., in *Sedimentation engineering: Processes, measurements, modeling: practice:* ASCE manuals and reports on engineering practice No. 110, edited by M. H. García, pp. 320– 339, ASCE, Reston, Va.

Gray, J. R., and Landers, M. N. (2013), *Measuring suspended sediment, in Comprehensive Water Quality and Purification*, vol. 1, edited by S. Ahuja, pp. 159– 204, Elsevier, Waltham, Mass., doi: 10.1016/B978-0-12-382182-9.00012-8.

Guney, M. S., Bombar, G., & Aksoy, A. O. (2013). Experimental study of the coarse surface development effect on the bimodal bed-load transport under unsteady flow conditions. *Journal of Hydraulic Engineering, 139*(1), 12-21.

Gunsolus, E. H., & Binns, A. D. (2018). Effect of morphologic and hydraulic factors on hysteresis of sediment transport rates in alluvial streams. *River Research and Applications, 34*(2), 183-192.

Guo, L., & He, Q. (2011). Freshwater flocculation of suspended sediments in the Yangtze River, China. *Ocean Dynamics, 61*(2-3), 371-386, doi: 10.1007/s10236-011-0391-x.

Guy, H. P. (1969). *Laboratory theory and methods for sediment analysis*, in Techniques of Water-Resources Investigations of the U.S. Geol. Surv., book 5, chap. C1, 55 p, Reston, Va. [Available at http://pubs.usgs.gov/twri/twri5c1/]

Gyawali, A. J., & Stewart, R. D. (2019). An improved method for quantifying soil aggregate stability. *Soil Science Society of America Journal, 83*(1), 27-36, doi: 10.2136/SSSAJ2018.06.0235.

Harmar, O. P., & Clifford, N. J. (2006). Planform dynamics of the lower Mississippi River. *Earth Surface Processes and Landforms: The Journal of the British Geomorphological Research Group, 31*(7), 825-843.

Harris, H. E., Baxter, C. V., & Davis, J. M. (2015). Debris flows amplify effects of wildfire on magnitude and composition of tributary subsidies to mainstem habitats. *Freshwater Science, 34*(4), 1457-1467.

Harrison, L. R., East, A. E., Smith, D. P., Logan, J. B., Bond, R. M., Nicol, C. L., ... & Luna, L. (2018). River response to large-dam removal in a Mediterranean hydroclimatic setting: Carmel River, California, USA. *Earth Surface Processes and Landforms, 43*(15), 3009-3021. https://doi.org/10.1002/esp.4464

Heckmann, T., & Schwanghart, W. (2013). Geomorphic coupling and sediment connectivity in an alpine catchment—Exploring sediment cascades using graph theory. *Geomorphology, 182*, 89-103.

Hession, W. C. (2017). *Reducing Sediment in Stroubles Creek, Blacksburg, VA*. [Available at https://vtechworks.lib.vt.edu/bitstream/handle/10919/81783/SCIP_FinalReport.pdf?sequence=1&isAllowed=y]

Hooke, R. L. (1994). On the efficacy of humans as geomorphic agents. *GSA Today, 4*(9), 217, 224–225.

Houser, B. (1980). Erosional history of the New River, Southern Appalachians, Virginia (Doctoral dissertation, Virginia Polytechnic Institute and State University).

Humphries, R., Venditti, J. G., Sklar, L. S., & Wooster, J. K. (2012). Experimental evidence for the effect of hydrographs on sediment pulse dynamics in gravel-bedded rivers. *Water Resour. Res., 48*, W01533. https://doi.org/10.1029/2011WR010419

Iverson, R. M. (1997). The physics of debris flows: Review of Geophysics Vol. 35.

Iverson, R. M., Reid, M. E., Logan, M., LaHusen, R. G., Godt, J. W., & Griswold, J. P. (2011). Positive feedback and momentum growth during debris-flow entrainment of wet bed sediment. *Nature Geoscience, 4*(2), 116-121.

Jaeger, K. L., Curran, C. A., Anderson, S. W., Morris, S. T., Moran, P. W., & Reams, K. A. (2017). *Suspended sediment, turbidity, and stream water temperature in the Sauk River Basin, western Washington, water years 2012-16* (No. 2017-5113). US Geological Survey.

Jahns, R. H., Griffitts, W. R., & Heinrich, E. W. (1952). *Mica deposits of the southeastern Piedmont, Part 1*, General features (No. 248-A). United States Government Printing Office.

James, L. A. (2010). Secular sediment waves, channel bed waves, and legacy sediment. *Geography Compass, 4*(6), 576–598. https://doi.org/10.1111/j.1749-8198.2010.00324.x

Jia, G., Shevliakova, E., Artaxo, P., De-Docoudré, N., Houghton, R., House, J., ... & Sporre, M. (2019). Land–climate interactions. In Special Report on Climate Change and Land: An IPCC Special Report on climate change, desertification, land degradation, sustainable land management, food security, and greenhouse gas fluxes in terrestrial ecosystems (pp. 133-206). IPCC.

Jones Jr, J. B., & Smock, L. A. (1991). Transport and retention of particulate organic matter in two low-gradient headwater streams. *Journal of the North American Benthological Society, 10*(2), 115-126, doi: https://doi.org/10.2307/1467572.

Kabir, S. M. I., & Ahmari, H. (2020). Evaluating the effect of sediment color on water radiance and suspended sediment concentration using digital imagery. *Journal of Hydrology, 589*, 125189, doi: 10.1016/j.jhydrol.2020.125189.

Kasprak, A., Wheaton, J. M., Ashmore, P. E., Hensleigh, J. W., & Peirce, S. (2015). The relationship between particle travel distance and channel morphology: Results from physical models of braided rivers. *Journal of Geophysical Research: Earth Surface, 120*(1), 55-74. https://doi.org/10.1002/2014JF003310

Kenney, T. A., Wilkowske, C. D., & Wright, S. J. (2007). Methods for estimating magnitude and frequency of peak flows for natural streams in Utah.

Keulegan, G. H. (1938). *Laws of turbulent flow in open channels* (Vol. 21, pp. 707-741). US: National Bureau of Standards.

Knighton, A. D. (1980). Longitudinal changes in size and sorting of stream-bed material in four English rivers. *Geological Society of America Bulletin, 91*(1), 55-62.

Kuhnle, R. A. (1992). Bed load transport during rising and falling stages on two small streams. *Earth Surface Processes and Landforms, 17*(2), 191-197.

Lancaster, S. T., & Casebeer, N. E. (2007). Sediment storage and evacuation in headwater valleys at the transition between debris-flow and fluvial processes. *Geology, 35*(11), 1027-1030.

Landers, M. N. (2012), Fluvial suspended sediment characteristics by high-resolution, surrogate metrics of turbidity, laser-diffraction, acoustic backscatter, and acoustic attenuation, PhD dissertation, 236 p., Dep. of Civil and Env. Eng., Georgia Inst. of Tech., Atlanta. [Available at http://hdl.handle.net/1853/43747]

Lauer, J. W., & Parker, G. (2008). Modeling framework for sediment deposition, storage, and evacuation in the floodplain of a meandering river: Theory. *Water Resour. Res., 44*, W04425. http://doi.org/10.1029/2006WR005528

Lauer, J. W., Viparelli, E., & Piégay, H. (2016). Morphodynamics and sediment tracers in 1-D (MAST-1D): 1-D sediment transport that includes exchange with an off-channel sediment reservoir. *Advances in Water Resources, 93,* 135-149. https://doi.org/10.1016/j.advwatres.2016.01.012

Lee, K. T., Liu, Y. L., & Cheng, K. H. (2004). Experimental investigation of bedload transport processes under unsteady flow conditions. *Hydrological processes, 18*(13), 2439-2454.

Legg, N. T., Meigs, A. J., Grant, G. E., & Kennard, P. (2014). Debris flow initiation in proglacial gullies on Mount Rainier, Washington. *Geomorphology, 226,* 249-260, doi: 10.1016/j.geomorph.2014.08.003.

Lisenby, P. E., Croke, J., & Fryirs, K. A. (2018). Geomorphic effectiveness: A linear concept in a non-linear world. *Earth Surface Processes and Landforms, 43*(1), 4-20.

Lisle, T. E. (2008). *The evolution of sediment waves influenced by varying transport capacity in heterogeneous rivers, in Gravel Bed Rivers VI: From Process Understanding to River Restoration*, edited by H. Habersack, H. Piegay, and M. Rinaldi, pp. 443–472, Elsevier, Amsterdam. https://doi.org/10.1016/S0928-2025(07)11136-6

Lisle, T. E., Cui, Y., Parker, G., Pizzuto, J. E., & Dodd, A. M. (2001). The dominance of dispersion in the evolution of bed material waves in gravel-bed rivers. *Earth Surf. Process. Landforms, 26*, 1409-1420. https://doi.org/10.1002/esp.300

Lisle, T. E., Pizzuto, J. E., Ikeda, H., Iseya, F., & Kodama, Y. (1997). Evolution of a sediment wave in an experimental channel. *Water Resour. Res., 33*(8), 1971-1981. https://doi.org/10.1029/97WR01180

Liu, Y., Stanturf, J., & Goodrick, S. (2010). Trends in global wildfire potential in a changing climate. *Forest ecology and management, 259*(4), 685-697.

Lyon, J. P., & O'CONNOR, J. P. (2008). Smoke on the water: Can riverine fish populations recover following a catastrophic fire-related sediment slug?. *Austral Ecology, 33*(6), 794-806.

Mao, L. (2018). The effects of flood history on sediment transport in gravel-bed rivers. *Geomorphology, 322,* 196-205.

Major, J. J., East, A. E., O'Connor, J. E., Grant, G. E., Wilcox, A. C., Magirl, C. S., ... & Tullos, D. D. (2017). Geomorphic responses to dam removal in the United States–a two-decade perspective. *Gravel-bed rivers, 10*(9781118971437), 355-383.

Major, J. J., O'Connor, J. E., Podolak, C. J., Keith, M. K., Grant, G. E., Spicer, K. R., Pittman, S., Bragg, H. M., Wallick, J. R., Tanner, D. Q., Rhode, A., & Wilcock, P. R. (2012). *Geomorphic response of the Sandy River, Oregon, to removal of Marmot Dam.* USGS Professional Paper 1792, 64 p.

Masteller, C. C., & Finnegan, N. J. (2017). Interplay between grain protrusion and sediment entrainment in an experimental flume. *Journal of Geophysical Research: Earth Surface, 122*(1), 274-289.

Medina, V., Hürlimann, M., & Bateman, A. (2008). Application of FLATModel, a 2D finite volume code, to debris flows in the northeastern part of the Iberian Peninsula. *Landslides, 5*(1), 127-142.

Mikkelsen, O., and M. Pejrup (2000), In situ particle size spectra and density of particle aggregates in a dredging plume, *Mar. Geol., 170*(3–4), 443– 459, doi: 10.1016/S0025-3227(00)00105-5.

Mikkelsen, O., and M. Pejrup (2001), The use of a LISST-100 laser particle sizer for in-situ estimates of floc size, density and settling velocity, *Geo Mar. Lett., 20*(4), 187– 195, doi: 10.1007/s003670100064.

Miller, J.P., 1958. *High mountain streams: effects of geology on channel characteristics and bed material*. Memoir 4, State Bureau of Mines and Mineral Resources. New Mexico Institute of Mines and Mining Technology, Socorro, New Mexico.

Miller, J. D., & Safford, H. (2012). Trends in wildfire severity: 1984 to 2010 in the Sierra Nevada, Modoc Plateau, and southern Cascades, California, USA. *Fire Ecology, 8*(3), 41-57.

Montgomery, D. R., & Buffington, J. M. (1998). Channel processes, classification, and response. *River Ecology and Management: Lessons from the Pacific Coastal Ecoregion, RJ Naiman and RE Bilby (Editors)*. Springer-Verlag, New York, New York, 13-42.

Moody, J. A., & Martin, D. A. (2001). *Hydrologic and sedimentologic response of two burned watersheds in Colorado* (No. 2001-4122).

Moody, J. A., & Martin, D. A. (2009). Synthesis of sediment yields after wildland fire in different rainfall regimes in the western United States. *International Journal of Wildland Fire, 18*(1), 96-115.

Moody, J. A., & Martin, D. A. (2004). Wildfire impacts on reservoir sedimentation in the western United States. In *Proceedings of the Ninth International Symposium on River Sedimentation* (pp. 1095-1102). Tsinghua University Press China.

Moore, R. B., McKay, L. D., Rea, A. H., Bondelid, T. R., Price, C. V., Dewald, T. G., & Johnston, C. M. (2019). *User's guide for the national hydrography dataset plus (NHDPlus) high resolution* (No. 2019-1096). US Geological Survey.

Murphy, B. P., Czuba, J. A., & Belmont, P. (2019). Post-wildfire sediment cascades: A modeling framework linking debris flow generation and network-scale sediment routing. *Earth Surface Processes and Landforms, 44*(11), 2126-2140. https://doi.org/10.1002/esp.4635

Murphy, B. P., Yocom, L. L., & Belmont, P. (2018). Beyond the 1984 perspective: Narrow focus on modern wildfire trends underestimates future risks to water security. *Earth's Future, 6*(11), 1492-1497. https://doi.org/10.1029/2018EF001006

Nash, J. E., & Sutcliffe, J. V. (1970). River flow forecasting through conceptual models part I—A discussion of principles. *Journal of hydrology, 10*(3), 282-290.

Nelson, A., & Dubé, K. (2016). Channel response to an extreme flood and sediment pulse in a mixed bedrock and gravel-bed river. *Earth Surface Processes and Landforms, 41*(2), 178-195. https://doi.org/10.1002/esp.3843

Nyman, P., Box, W. A., Stout, J. C., Sheridan, G. J., Keesstra, S. D., Lane, P. N., & Langhans, C. (2020). Debris-flow-dominated sediment transport through a channel network after wildfire. *Earth Surface Processes and Landforms, 45*(5), 1155-1167.

O'Connor, J. E., Mangano, J. F., Anderson, S. W., Wallick, J. R., Jones, K. L., & Keith, M. K. (2014). Geologic and physiographic controls on bed-material yield, transport, and channel morphology for alluvial and bedrock rivers, western Oregon. *GSA Bull., 126*(3-4), 377–397. https://doi.org/10.1130/b30831.1

Pace, K. M., Tullos, D., Walter, C., Lancaster, S., & Segura, C. (2017). Sediment pulse behaviour following dam removal in gravel-bed rivers. *River research and applications, 33*(1), 102-112. https://doi.org/10.1002/rra.3064

Paola, C., Parker, G., Seal, R., Sinha, S. K., Southard, J. B., & Wilcock, P. R. (1992). Downstream fining by selective deposition in a laboratory flume. *Science, 258*(5089), 1757-1760. https://doi.org/10.1126/science.258.5089.1757

Paola, C., Heller, P. L., & Angevine, C. L. (1992). The large-scale dynamics of grain-size variation in alluvial basins, 1: Theory. *Basin research, 4*(2), 73-90.

Parker, G. (1978). Self-formed straight rivers with equilibrium banks and mobile bed. Part 2. The gravel river. *Journal of Fluid mechanics, 89*(1), 127-146. https://doi.org/10.1017/S0022112078002505

Parker, G. (2004), 1D aggradation and degradation of rivers: Normal flow assumption, chap. 14, in *1D Sediment Transport Morphodynamics with Applications to Rivers and Turbidity Currents*, Urbana, Illinois, 38 p. [Available at http://hydrolab.illinois.edu/people/parkerg//morphodynamics_e-book.htm., last accessed 1 May 2022.]

Parker, G. (1991). Selective sorting and abrasion of river gravel. I: Theory. *J. Hydraul. Eng., 117*(2), 131-149. https://doi.org/10.1061/(ASCE)0733-9429(1991)117:2(131)

Parker, G., Shimizu, Y., Wilkerson, G. V., Eke, E. C., Abad, J. D., Lauer, J. W., Paola, C., Dietrich, W. E. and Voller, V. R. (2011). A new framework for modeling the migration of meandering rivers. *Earth Surf. Process. Landforms, 36*(1), 70–86. https://doi.org/10.1002/esp.2113

Parsons, A. J., Bracken, L., Poeppl, R. E., Wainwright, J., & Keesstra, S. D. (2015). Introduction to special issue on connectivity in water and sediment dynamics. *Earth Surface Processes and Landforms, 40*(9), 1275-1277.

Pechony, O., & Shindell, D. T. (2010). Driving forces of global wildfires over the past millennium and the forthcoming century. *Proceedings of the National Academy of Sciences, 107*(45), 19167-19170.

Pedocchi, F., & García, M. H. (2006). Evaluation of the LISST-ST instrument for suspended particle size distribution and settling velocity measurements. *Continental Shelf Research, 26*(8), 943-958, doi: 10.1016/j.csr.2006.03.006.

Pfeiffer, A. M., Barnhart, K. R., & Czuba, J. A. (2020). NetworkSedimentTransporter: A Landlab component for bed material transport through river networks. *Journal of Open Source Software, 5*(53), 2341. https://doi.org/10.21105/joss.02341

Pfeiffer, A. M., Collins, B. D., Anderson, S. W., Montgomery, D. R., & Istanbulluoglu, E. (2019). River bed elevation variability reflects sediment supply, rather than peak flows, in the uplands of Washington State. *Water Resources Research, 55*(8), 6795-6810. https://doi.org/10.1029/2019WR025394

Pfeiffer, A. M., & Finnegan, N. J. (2018). Regional variation in gravel riverbed mobility, controlled by hydrologic regime and sediment supply. *Geophysical Research Letters, 45*(7), 3097-3106. https://doi.org/10.1002/2017GL076747

Pfeiffer, A. M., Finnegan, N. J., & Willenbring, J. K. (2017). Sediment supply controls equilibrium channel geometry in gravel rivers. *Proceedings of the National Academy of Sciences, 114*(13), 3346-3351. https://doi.org/10.1073/pnas.1612907114

Phillips, C. B., Hill, K. M., Paola, C., Singer, M. B., & Jerolmack, D. J. (2018). Effect of flood hydrograph duration, magnitude, and shape on bed load transport dynamics. *Geophysical Research Letters, 45*(16), 8264-8271.

Pierce, J. L., Meyer, G. A., & Rittenour, T. (2011). The relation of Holocene fluvial terraces to changes in climate and sediment supply, South Fork Payette River, Idaho. *Quaternary Science Reviews, 30*(5-6), 628-645.

Pirulli, M., & Pastor, M. (2012). Numerical study on the entrainment of bed material into rapid landslides. *Geotechnique, 62*(11), 959-972.

Pitlick, J., Cui, Y., & Wilcock, P. (2009). *Manual for computing bed load transport using BAGS (Bedload Assessment for Gravel-bed Streams) Software*, Gen. Tech. Rep. RMRS-GTR-223, 45 p., USDA Forest Service, Rocky Mountain Research Station, Fort Collins, Colorado.

Pizzuto, J., Schenk, E. R., Hupp, C. R., Gellis, A. C., Noe, G., Williamson, E., … Newbold, D. (2014). Characteristic length scales and time-averaged transport velocities of suspended sediment in the mid-Atlantic region, USA. *Water Resources Research, 50*(2), 790–805. https://doi.org/10.1002/2013wr014485

PSLC, Puget Sound LiDAR Consortium (2012). 2008-2009 Lewis County LiDAR Project, accessed 4 September 2012 at http://pugetsoundlidar.ess.washington.edu/

Recking, A., Liébault, F., Peteuil, C., & Jolimet, T. (2012). Testing bedload transport equations with consideration of time scales. *Earth Surface Processes and Landforms, 37*(7), 774-789.

Recking, A., Piton, G., Vazquez-Tarrio, D., & Parker, G. (2016). Quantifying the morphological print of bedload transport. *Earth Surface Processes and Landforms, 41*(6), 809-822. https://doi.org/10.1002/esp.3869

Reid, I., Frostick, L. E., & Layman, J. T. (1985). The incidence and nature of bedload transport during flood flows in coarse-grained alluvial channels. *Earth Surface Processes and Landforms, 10*(1), 33-44.

Reneau, S. L., Katzman, D., Kuyumjian, G. A., Lavine, A., & Malmon, D. V. (2007). Sediment delivery after a wildfire. *Geology, 35*(2), 151-154.

Rice, S. P. (2017). Tributary connectivity, confluence aggradation and network biodiversity. *Geomorphology, 277*, 6-16.

Rice, S. (1998). Which tributaries disrupt downstream fining along gravel-bed rivers?. *Geomorphology, 22*(1), 39-56.

Rice, S., & Church, M. (1998). Grain size along two gravel-bed rivers: statistical variation, spatial pattern and sedimentary links. *Earth Surface Processes and Landforms: The Journal of the British Geomorphological Group, 23*(4), 345-363.

Rice, S. P., Ferguson, R. I., & Hoey, T. B. (2006). Tributary control of physical heterogeneity and biological diversity at river confluences. *Canadian Journal of Fisheries and Aquatic Sciences, 63*(11), 2553-2566.

Rice, S. P., Greenwood, M. T., & Joyce, C. B. (2001). Tributaries, sediment sources, and the longitudinal organisation of macroinvertebrate fauna along river systems. *Canadian Journal of Fisheries and Aquatic Sciences, 58*(4), 824-840.

Ritchie, A. C., Warrick, J. A., East, A. E., Magirl, C. S., Stevens, A. W., Bountry, J. A., ... & Ogston, A. S. (2018). Morphodynamic evolution following sediment release from the world's largest dam removal. *Scientific reports, 8*(1), 1-13. https://doi.org/10.1038/s41598-018-30817-8

Rickenmann, D. (2012). Alluvial steep channels: Flow resistance, bedload transport prediction, and transition to debris flows. Gravel-Bed Rivers: Processes, Tools, *Environments*, 386-397.

Robinne, F. N., Miller, C., Parisien, M. A., Emelko, M. B., Bladon, K. D., Silins, U., & Flannigan, M. (2016). A global index for mapping the exposure of water resources to wildfire. *Forests,* 7(1), 22.

Rouse, H. (1939). *An analysis of sediment transportation in the light of fluid turbulence*, U.S. Department of Agriculture, Soil Conservation Service, SCS-TR 25, Washington D.C.

Ryan, S. E., Bishop, E. L., & Daniels, J. M. (2014). Influence of large wood on channel morphology and sediment storage in headwater mountain streams, Fraser Experimental Forest, Colorado. *Geomorphology, 217,* 73-88. https://doi.org/10.1016/j.geomorph.2014.03.046

Sankey, J. B., Kreitler, J., Hawbaker, T. J., McVay, J. L., Miller, M. E., Mueller, E. R., Vaillant, N. M., Lowe, S. E., and Sankey, T. T. (2017), Climate, wildfire, and erosion ensemble foretells more sediment in western USA watersheds, *Geophys. Res. Lett., 44,* 8884–8892. https://doi.org/10.1002/2017GL073979

Santos, A. I., Carinhas, D., Oliveira, A., Pinto, J. P., Freitas, M. C., & Hanes, D. M. (2021). A statistical interpretation of acoustic backscatter and laser responses to suspended particle variations in the coastal shelf. *Marine Geology, 436*, 106474, doi: 10.1016/j.margeo.2021.106474.

Sassi, M. G., A. J. F. Hoitink, and B. Vermeulen (2012), Impact of sound attenuation by suspended sediment on ADCP backscatter calibrations, *Water Resour. Res., 48*, W09520, doi: 10.1029/2012WR012008.

Schmitt, R. J., Bizzi, S., & Castelletti, A. (2016). Tracking multiple sediment cascades at the river network scale identifies controls and emerging patterns of sediment connectivity. *Water Resources Research, 52*(5), 3941-3965.

Schmitt, R. J., Bizzi, S., Castelletti, A. F., & Kondolf, G. M. (2018). Stochastic modeling of sediment connectivity for reconstructing sand fluxes and origins in the unmonitored Se Kong, Se San, and Sre Pok tributaries of the Mekong River. *Journal of Geophysical Research: Earth Surface, 123*(1), 2-25. https://doi.org/10.1002/2016JF004105

Scott, K. M. (1988). *Origins, behavior, and sedimentology of lahars and lahar-runout flows in the Toutle-Cowlitz River system* (No. 1447-A).

Sequoia Scientific, Inc. (2017), LISST-SL2 User's Manual version 1.2, Bellevue, Wash. [Available at https://www.sequoiasci.com/wp-content/uploads/2013/07/LISST-SL2_Users_Manual_v1.2.pdf, last accessed 12 Dec 2021]

Sklar, L. S., Fadde, J., Venditti, J. G., Nelson, P., Wydzga, M. A., Cui, Y., & Dietrich, W. E. (2009), Translation and dispersion of sediment pulses in flume experiments simulating gravel augmentation below dams. *Water Resour. Res., 45*, W08439. https://doi.org/10.1029/2008WR007346

Smith, H. G., Sheridan, G. J., Lane, P. N., Nyman, P., & Haydon, S. (2011). Wildfire effects on water quality in forest catchments: a review with implications for water supply. *Journal of Hydrology, 396*(1-2), 170-192.

Snyder, N. P., Nesheim, A. O., Wilkins, B. C., & Edmonds, D. A. (2013). Predicting grain size in gravel-bedded rivers using digital elevation models: Application to three Maine watersheds. *Bulletin, 125*(1-2), 148-163. https://doi.org/10.1130/B30694.1

Staley, D. M., Negri, J. A., Kean, J. W., Laber, J. L., Tillery, A. C., & Youberg, A. M. (2017). Prediction of spatially explicit rainfall intensity–duration thresholds for post-fire debris-flow generation in the western United States. *Geomorphology, 278,* 149-162.

Sutherland, D. G., Hansler-Ball, M., Hilton, S. J., & Lisle, T. E. (2002). Evolution of a landslide induced sediment wave in the Navarro River, California. *GSA Bull. 114*(8), 1036–1048. https://doi.org/10.1130/0016-7606(2002)114<1036:EOALIS>2.0.CO;2

Takahashi, T. (1981). Debris flow. *Annual review of fluid mechanics, 13*(1), 57-77.

Tang, C., Zhu, J., Ding, J., Cui, X. F., Chen, L., & Zhang, J. S. (2011). Catastrophic debris flows triggered by a 14 August 2010 rainfall at the epicenter of the Wenchuan earthquake. *Landslides, 8*(4), 485-497.

Topping, D. J., Rubin, D. M., Wright, S. A., & Melis, T. S. (2011). *Field evaluation of the error arising from inadequate time averaging in the standard use of depth-integrating suspended-sediment samplers* (p. 95). Reston, VA: US Geological Survey.

Uhrich, M. A., Spicer, K. R., Mosbrucker, A. R., & Christianson, T. S. (2015). Evaluating turbidity and suspended-sediment concentration relations from the North Fork Toutle River

basin near Mount St. Helens, Washington; annual, seasonal, event, and particle size variations - a preliminary analysis. In *5th Federal Interagency Hydrologic Modeling Conference and the 10th Federal Interagency Sedimentation Conference.*

U.S. Geological Survey (2020), National map, http://nationalmap.gov, (accessed November 9, 2020).

U.S. Geological Survey (2014), *Sediment laboratory quality assurance project*, U.S. Department of the Interior, U.S. Geological Survey, Reston, Va. [Available at http://bqs.usgs.gov/slqa/frontpage_study_results.htm, last accessed 12 Dec 2021]

U.S. Department of Agriculture (2011). National Agricultural Imagery Program, U.S. Department of Agriculture website accessed December 14, 2011, at http://www.fsa.usda.gov/FSA/apfoapp?area=home&subject=prog&topic=nai

USGS, U.S. Geological Survey (2021). USGS 12082500, Nisqually River near National, WA. Accessed 15 July 2021 at https://waterdata.usgs.gov/nwis/inventory/?site_no=12082500&agency_cd=USGS

Venditti, J. G., Dietrich, W. E., Nelson, P. A., Wydzga, M. A., Fadde, J., & Sklar, L. (2010a). Effect of sediment pulse grain size on sediment transport rates and bed mobility in gravel bed rivers. *J. Geophys. Res., 115*, F03039. https://doi.org/10.1029/2009JF001418

Venditti, J. G., Dietrich, W. E., Nelson, P. A., Wydzga, M. A., Fadde, J., & Sklar, L. (2010b). Mobilization of coarse surface layers in gravel-bedded rivers by finer gravel bed load. *Water Resour. Res., 46*, W07506. https://doi.org/10.1029/2009WR008329

Viparelli, E., Lauer, J. W., Belmont, P., & Parker, G. (2013). A numerical model to develop long-term sediment budgets using isotopic sediment fingerprints. *Computers & geosciences, 53*, 114-122. https://doi.org/10.1016/j.cageo.2011.10.003

Walder, J. S., & Driedger, C. L. (1993). *Volcano fact sheet; glacier-generated debris flows at Mount Rainier* (No. 93-124). US Geological Survey.

Walder, J. S., & Driedger, C. L. (1994). Rapid geomorphic change caused by glacial outburst floods and debris flows along Tahoma Creek, Mount Rainier, Washington, USA. *Arctic and Alpine Research, 26*(4), 319-327.

Wall, S. (2021), Predictive Models of Post-Wildfire Debris Flow Volume and Grain Size Distribution in the Intermountain West, M.S. Thesis, Utah State University.

Walling, D. E., and B. W. Webb (1987), Suspended load in gravel-bed rivers: UK experience, in *Sediment Transport in Gravel-Bed Rivers*, edited by C. R. Thorne, J. C. Bathurst, and R. D. Hey, pp. 691–732, John Wiley, New York.

Wang, G., Sassa, K., & Fukuoka, H. (2003). Downslope volume enlargement of a debris slide–debris flow in the 1999 Hiroshima, Japan, rainstorm. *Engineering geology, 69*(3-4), 309-330.

Warrick, J. A., Bountry, J. A., East, A. E., Magirl, C. S., Randle, T. J., Gelfenbaum, G., ... & Duda, J. J. (2015). Large-scale dam removal on the Elwha River, Washington, USA: Source-to-sink sediment budget and synthesis. *Geomorphology, 246*, 729-750. https://doi.org/10.1016/j.geomorph.2015.01.010

Waters, K. A., & Curran, J. C. (2015). Linking bed morphology changes of two sediment mixtures to sediment transport predictions in unsteady flows. *Water Resources Research, 51*(4), 2724-2741.

Welber, M., Papangelakis, E., Ashmore, P., & MacVicar, B. (2020). Experiments on restoring alluvial cover in straight and meandering rivers using gravel augmentation. *River Research and Applications, 36*(8), 1543-1558. https://doi.org/10.1002/rra.3699

Welch, N. H., Allen, P. B., & Galindo, D. J. (1979). *Particle-size analysis by pipette and SediGraph* (Vol. 8, No. 4, pp. 543-546). American Society of Agronomy, Crop Science Society of America, and Soil Science Society of America.

Westerling, A. L., Turner, M. G., Smithwick, E. A., Romme, W. H., & Ryan, M. G. (2011). Continued warming could transform Greater Yellowstone fire regimes by mid-21st century. *Proceedings of the National Academy of Sciences, 108*(32), 13165-13170.

Western Water Assessment (WWA) (2021) Intermountain West climate: https://wwa.colorado.edu/climate/index.html (accessed November 9, 2021).

Wilcock, P. R., & Crowe, J. C. (2003). Surface-based transport model for mixed-size sediment. *J. Hydraul. Eng., 129*(2), 120-18. https://doi.org/10.1061/(ASCE)0733-9429(2003)129:2(120)

Wharton, G., Mohajeri, S. H., & Righetti, M. (2017). The pernicious problem of streambed colmation: A multi-disciplinary reflection on the mechanisms, causes, impacts, and management challenges. *Wiley Interdisciplinary Reviews: Water, 4*(5), e1231, doi: 10.1002/wat2.1231.

Williams, N. D., D. E. Walling, and G. J. L. Leeks (2007), High temporal resolution in situ measurement of the effective particle size characteristics of fluvial suspended sediment, *Water Res., 41*(5), 1081–1093, doi: 10.1016/j.watres.2006.11.010.

Wohl, E. (2017). Connectivity in rivers. *Progress in Physical Geography, 41*(3), 345-362.

Wohl, E., & Scott, D. N. (2017). Wood and sediment storage and dynamics in river corridors. *Earth Surface Processes and Landforms, 42*(1), 5-23. https://doi.org/10.1002/esp.3909

Wolman, M. G. (1954). A method of sampling coarse river-bed material. *Transactions of the American Geophysical Union, 35*(6), 951-956.

Wooster, J. K., Dusterhoff, S. R., Cui, Y., Sklar, L. S., Dietrich, W. E., & Malko, M. (2008). Sediment supply and relative size distribution effects on fine sediment infiltration into immobile gravels. *Water Resour. Res., 44*, W03424. https://doi.org/10.1029/2006WR005815

Xu, Q., Zhang, S., Li, W. L., & Van Asch, T. W. (2012). The 13 August 2010 catastrophic debris flows after the 2008 Wenchuan earthquake, China. *Natural Hazards and Earth System Sciences, 12*(1), 201-216.

Appendix

Text S1. Additional Modeling Advancements to Upstream Sediment Supply

The channel network is represented as a series of 400 m-long links and sediment can be supplied to any links within the network on a daily timestep. Various sediment supply methods include: (1) supplying the sediment moved at the input link's transport capacity, (2) using a sediment rating curve, or (3) maintaining an effectively infinite reservoir of sediment at the input location and letting streamflow continually erode the deposit while maintaining a fixed bed elevation at the upstream node.

For supply method 1, the volume and grain size of sediment moved at transport capacity was computed in the upstream link. The parcel volume that moved out of that link by the flow was replenished at each timestep. Thus, upstream input was always kept at transport capacity. Method 2 incorporated a sediment rating curve using the Bedload Assessment in Gravel-bedded Streams (BAGS) software (Pitlick et al., 2009). A sediment rating curve was generated using the surface-based bedload equation of Wilcock & Crowe (2003) and included inputs of Manning's n, reach average bankfull width, surface grain size distribution, reach average bed slope, and the flow discharge record at the upstream end of the model. The BAGS output was sediment transport rate by weight and size for flow discharges of different exceedance probabilities. This rating curve was then used to interpolate sediment volume

by size for a given discharge at each timestep. For method 3, an infinite volume of sediment (large enough so as not to empty during the simulation) was stored in the upstream link with a fixed bed elevation. The flow continuously eroded this sediment and delivered it downstream in the river network. This option was the most numerically stable for this model application and was used throughout all model runs.

Text S2. Space-Time Contours of Sediment Depth and Gravel Size

We have summarized pulse impacts in terms of sediment depth and median gravel size. But in this application, we found that changes in median gravel size were inversely related to the changes in sediment depth (i.e., bed aggradation occurred with bed fining and bed incision occurred with bed coarsening). We illustrate this by showing results from the uniform 10 mm pulse of 0.4 m depth (i.e., 19,000 m^3) under the medium flow condition (Figure S1). If we take a vertical slice through these space-time contours (e.g., dashed vertical brown line in Figures S1a, b at stationing 26.8 km), we can observe the fluctuations in sediment depth or grain size at a specific location through time (Figures S1c, d). The flow hydrograph is included as well to highlight that most fluctuations in bed sediment occur at high flow events.

In all other model results, when there is incision from baseline conditions (e.g., Figure S1a, brown regions), we also find coarsening of the bed surface (e.g., Figure S1b, blue regions). Conversely, model results exhibit a decrease in gravel size when/where a finer

sediment pulse accumulated. Incision from baseline implies increased transport due to the pulse introduction. The associated bed coarsening suggests that this transport is mainly of finer sediment. In this example, we also focus on a location 26.8 km downstream (brown plus sign in Figure 3.1; vertical lines in Figures S1a, b) to show the changes that occur at a single location through time (Figures S1c, d). The pulse (indicated by a star) arrived within 1.5 years at this location. Incision and bed coarsening both reach their maximum values at the same time, within 1 year, just prior to arrival of the pulse at this location. The maximum accumulation occurred once the pulse arrived (1.5 years), with a consequent decrease in median gravel size. After the pulse (i.e., after 1.5 years) changes were minor at this location. We do not suggest reading too much into individual fluctuations, but instead focus on larger scale trends.

Text S3. Additional Model Results

Comparison of changes from different pulse size: 10 mm and 30 mm pulse under medium flow

Model results showed initial pre-pulse incision in both cases (brown nearly straight lines in Figures S2a, b and negative fluctuations in Figure S2d) until the pulse arrives at 1.5 years and 3.5 years, respectively, causing aggradation (more or less straight blue line, Figures S2a, b). Model results showed more incision for the 10 mm pulse and more aggradation for the 30 mm pulse throughout the reach compared to the baseline condition. For the 30 mm pulse, we see incision at upstream reaches with higher slopes and prominent aggradation (15-17 km) at wider reaches with low slope.

Maximum changes from baseline are of similar magnitude for both pulse sizes at 7.6 km (Figure S2d). Model results showed that 80% of the pulse arrives at the outlet within 1.5 years for the 10 mm pulse and within 3.5 years for 30 mm pulse (Figure 3.4). The entire volume arrives within 2 years for the 10 mm pulse while only 93% of the 30 mm pulse arrives at the system outlet within the 30-year simulation period. Once that pulse has moved past the location at 7.6 km (after 1.5 years and 3.5 years for 10 mm and 30 mm pulse, respectively), pulse mixing with, and mobilizing of, the bed sediment results in longer term incision for the finer pulse and aggradation for the coarser pulse compared to baseline.

Comparison of changes from different pulse size: 30 mm and 70 mm pulse under high flow

We see initial pre-pulse incision in both cases until 1.5 years (brown nearly straight lines, Figures S3a, b). There is also slight pre-pulse aggradation due to the coarser pulse (1.5 to 11 years), which is observed at location 7.6 km (Figure S3d). The pulses aggraded the bed at 1.5 years and 11.5 years (more or less straight blue lines, Figures S3a, b, respectively). Under the high flow condition, these two pulse grain sizes create different post-pulse impact patterns. Once the pulse has passed this upstream reach (at 7.6 km), the mixing and mobilization of the bed sediment results in slight long-term accumulation for the finer pulse. For the 70 mm pulse, immediately after the pulse arrival (at 11.5 years), roughly 5 cm of incision occurs in this upstream reach. After this pulse has left the system, the last major flows begin to reduce the incision (at 21.5 years, Figure S3d).

The contour plots of model results show that the 30 mm pulse causes aggradation at locations with low channel slopes (6-9 km), and incision at narrow, constricted reaches (14-22 km). On the other hand, the impacts from the 70 mm pulse are largely controlled

by high flow events. There was an initial accumulation in most of the reaches, until the flow peak at around 11.5 years, which caused incision from the baseline condition during the remainder of the simulation period. There was mostly aggradation at wider downstream sections. Model results showed that 80% of the pulse arrived at the outlet within 2 years for the 30 mm pulse, and within 11.5 years for 70 mm pulse (Figure 3.4). Total pulse volume arrived within 2 years for the 30 mm pulse, while it took around 12 years for 90% of the pulse volume to travel through the system for the 70 mm pulse. The last 50% of the coarser pulse travelled very slowly compared to the finer pulse (Figure 3.4). The arrival time was, thus, primarily influenced by sediment-pulse grain size and then by the stream hydrology. At the upstream location (Figure S3d), the maximum pulse accumulation was around 8 cm (averaged over a 400-m link length) for the 70 mm pulse while it was around 6 cm for the 30 mm pulse. Additionally, incision from baseline was greater for the 70 mm pulse than for the 30 mm pulse.

Comparison of changes from different pulse volumes (depths)

Patterns of change in sediment depth were similar for two 30 mm uniform pulses with different volumes (Figures S4a, b). For both cases, there was an initial pre-pulse incision, followed by pulse accumulation (nearly straight blue line at around 3.5 years; Figures S4a, b). Post-pulse changes (after 3.5 years) included incision in steep upstream reaches and accumulation in flatter reaches (15-17 km). The upstream incision was, surprisingly, greater for the smaller pulse volume (darker brown in Figure S4a). Model results showed (Figure 3.4) that 80% of the pulse arrived at the outlet within 3.5 years for both pulse volumes, which resulted in similar timing of maximum pulse impact. The smaller volume pulse, counterintuitively, took longer (90% took more than 10 years) to fully move through the system than the larger volume pulse (for which 90% moved within 4 years; Figure 3.4).

These findings suggest that the smaller volume pulse was likely more fully mixing with the bed material and it took longer for those "tagged" pulse parcels to become remobilized and move downstream in this model.

Comparison of changes from different flow condition

We compared impacts of the 30 mm uniform pulse under medium and high flow conditions. Figures S5a, b show initial pre-pulse incision, followed by pulse accumulation (nearly straight blue line at approximately 3.5 years and 1.5 years respectively). Higher flow results in faster pulse movement through the system, as the river is able to mobilize more of the pulse. Model results showed that 80% of the pulse arrived at the outlet within 1.5 years under high flow and within 3.5 years under medium flow (Figure 3.4). This is when maximum impact from the pulse occurred (Figure S5d). The post-pulse pattern of bed change was quite different for the medium and high flow condition (Figures S5a, b). For medium flow, incision occurred in steep upstream reaches and accumulation occurred in lower slope reaches (at 15-17 km). In contrast, for high flow, more incision occurred in narrow, steep reaches and accumulation occurred in wider reaches. There was also a larger post-pulse accumulation during high flow at 7.6 km compared to medium flow (Figure S5d).

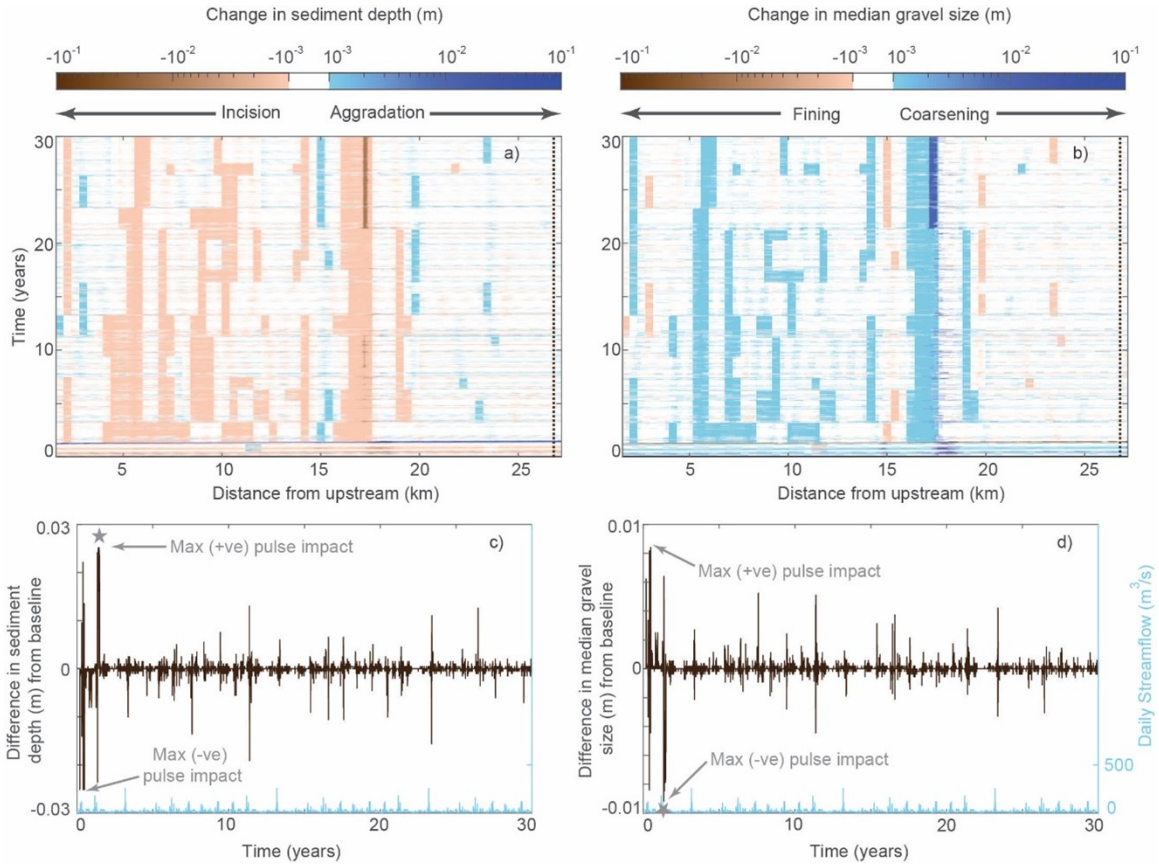

Figure S1: Changes from baseline condition resulting from a 10 mm uniform pulse of 0.4 m depth under the medium flow condition. (a, b) Space-time contours of change in sediment depth and median gravel size from baseline. (c, d) Temporal changes in sediment depth and median gravel size from baseline at a specific location (stationing 26.8 km; dotted brown line in (a, b)). The star indicates the arrival time of the sediment pulse at this location.

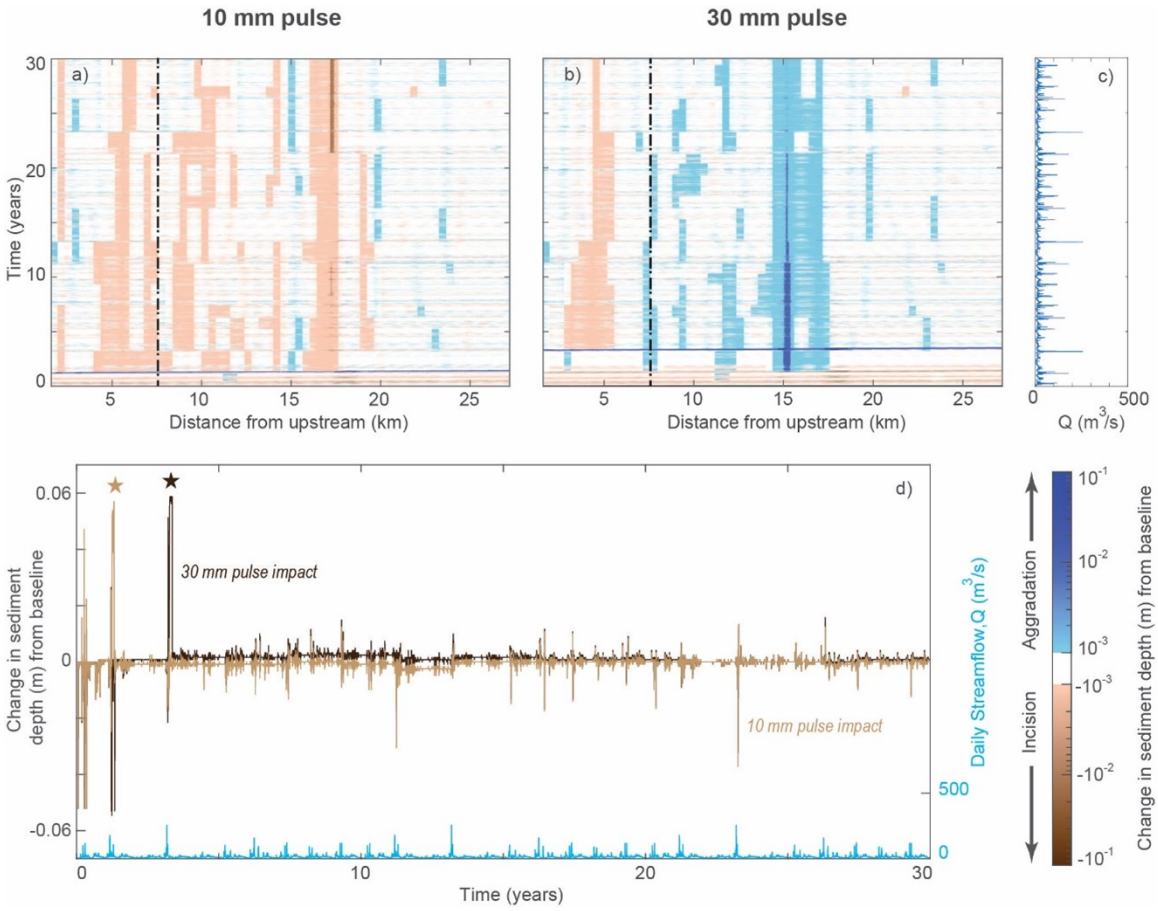

Figure S2: Comparison of the bed-elevation changes from 10 mm and 30 mm uniform pulses of 0.4 m depth for the medium flow condition. (a, b) Space-time contours of change in sediment depth from baseline due to 10 mm and 30 mm pulse. (c) Daily discharge at the upstream end of the model in medium flow condition. (d) Temporal changes in sediment depth from baseline at 7.6 km (location shown as dashed lines in (a) and (b)) due to 10 mm and 30 mm pulse, where the star indicates the location of the pulse.

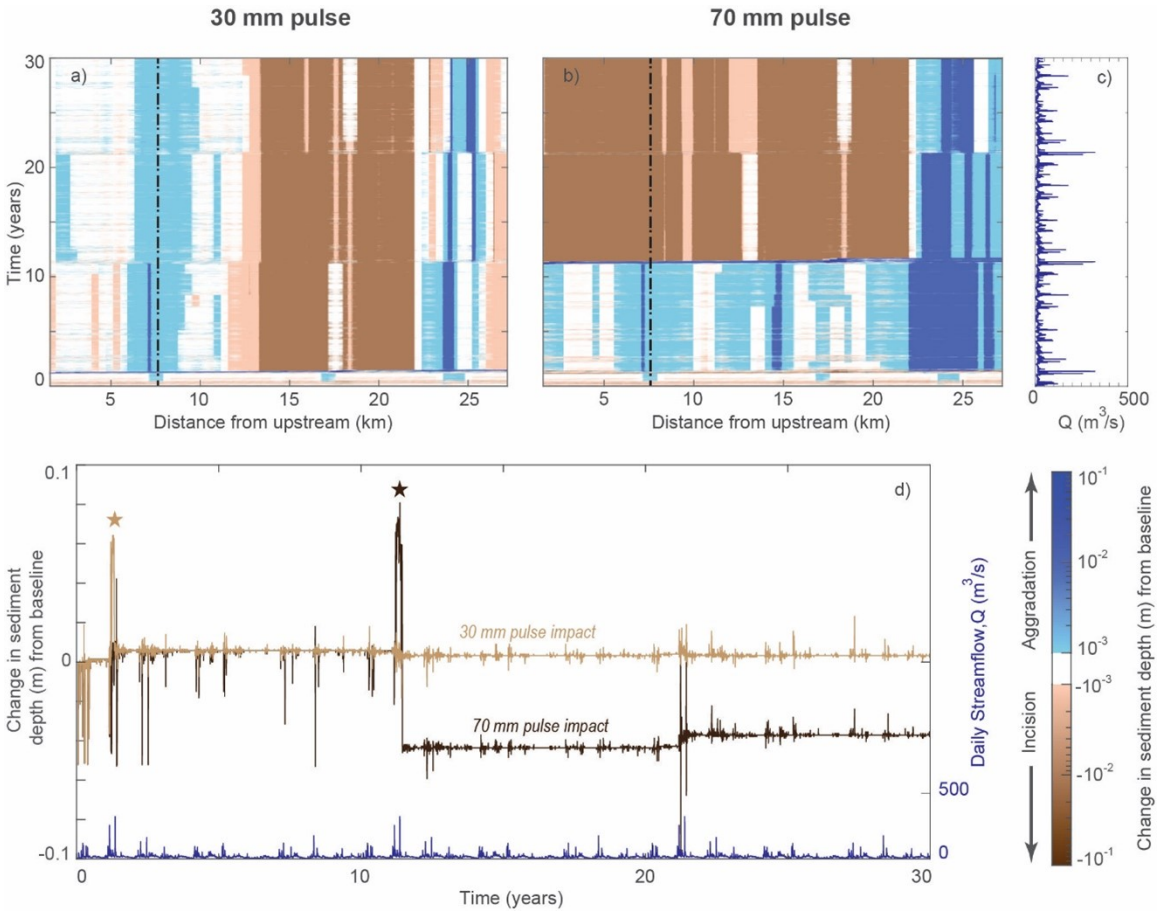

Figure S3: Comparison of the bed-elevation changes from 30 mm and 70 mm uniform pulses of 0.4 m depth for the high flow condition. (a, b) Space-time contours of change in sediment depth from baseline due to 30 mm and 70 mm pulse. (c) Daily discharge at the upstream end of the model in high flow condition. (d) Temporal changes in sediment depth from baseline at 7.6 km (location shown as dashed lines in (a) and (b)) due to 30 mm and 70 mm pulse, where the star indicates the location of the pulse.

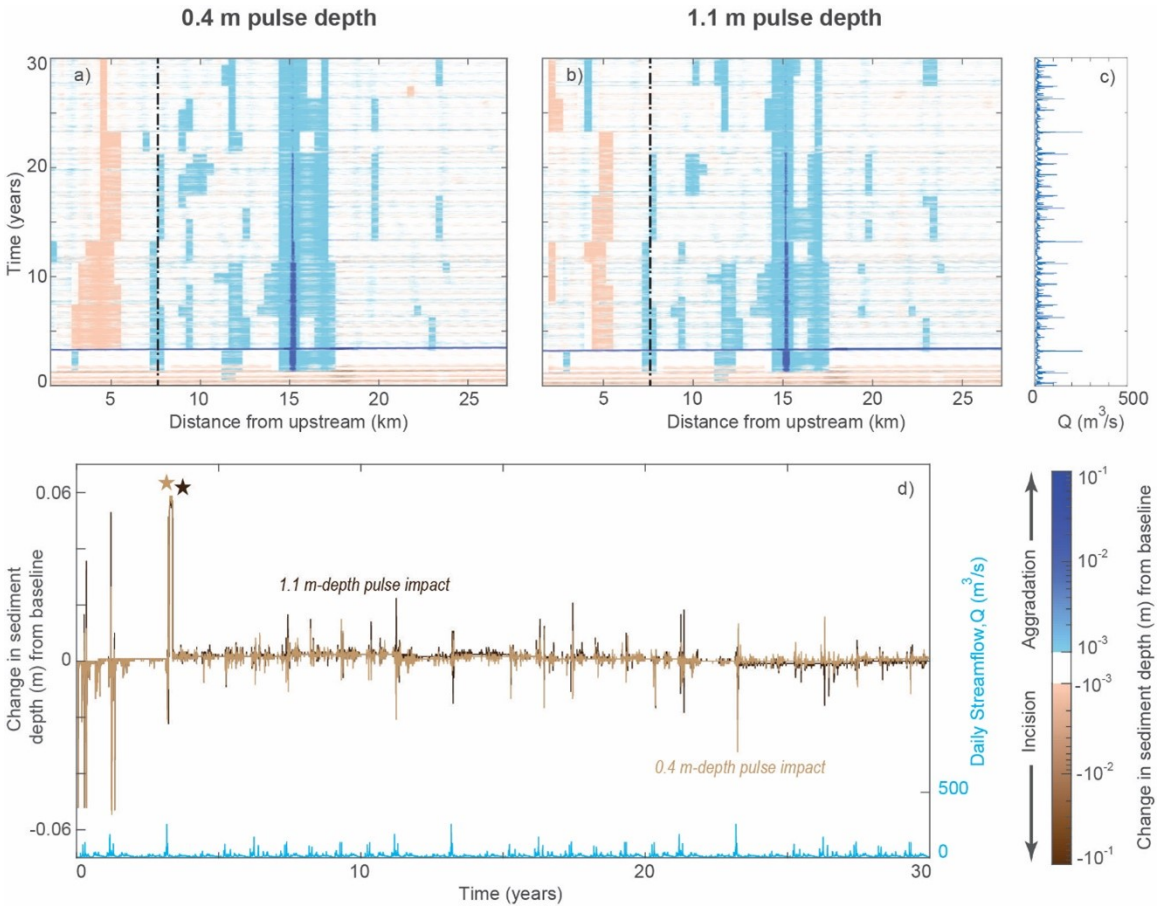

Figure S4: Comparison of the bed-elevation changes from 30 mm uniform pulse of 0.4 m and 1.1 m depth for the medium flow condition. (a, b) Space-time contours of change in sediment depth from baseline due to 0.4 m and 1.1 m pulse depth. (c) Daily discharge at the upstream end of the model in medium flow condition. (d) Temporal changes in sediment depth from baseline at 7.6 km (location shown as dashed lines in (a) and (b)) due to 0.4 m and 1.1 m pulse depth, where the star indicates the location of the pulse.

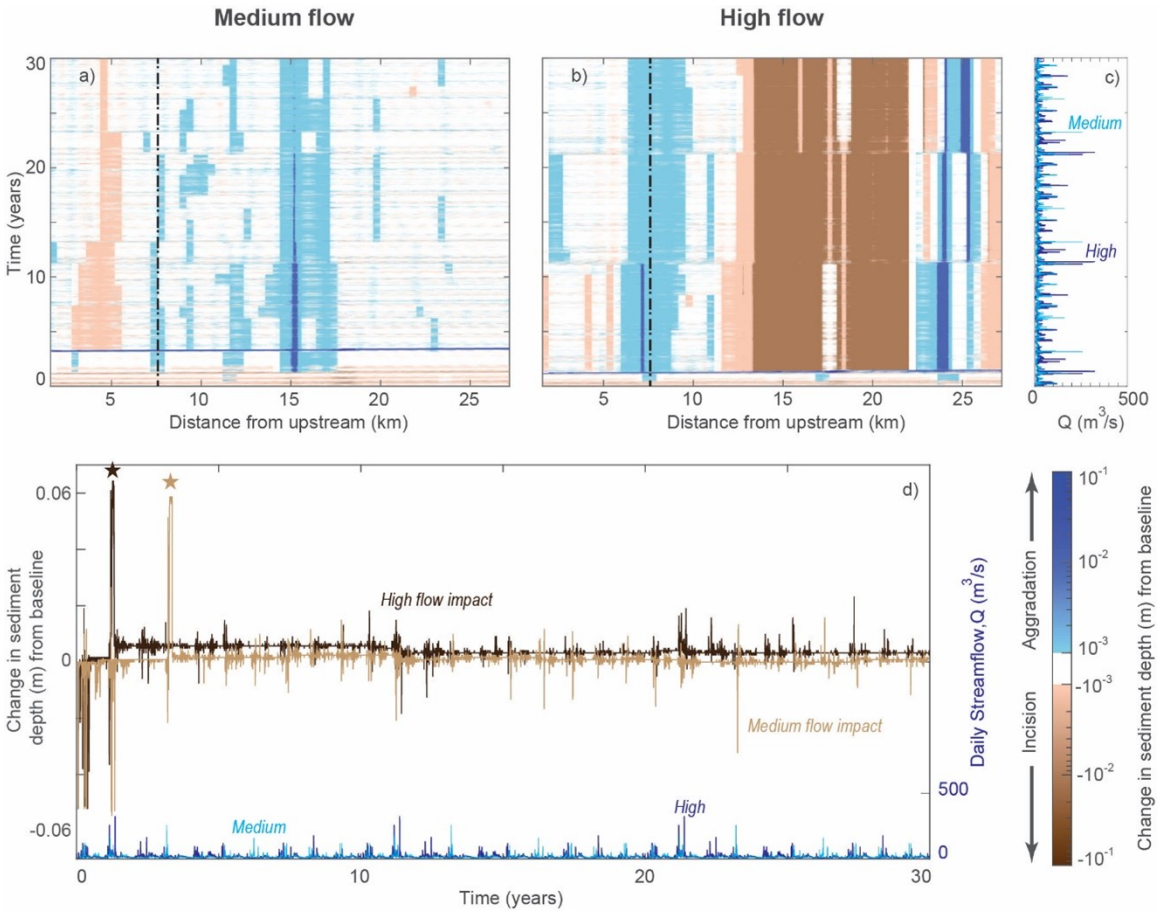

Figure S5: Comparison of the bed-elevation changes from 0.4 m depth 30 mm uniform pulse under medium and high flow condition. (a, b) Space-time contours of change in sediment depth from baseline due to medium and high flow. (c) Daily discharge at the upstream end of the model in medium and high flow condition. (d) Temporal changes in sediment depth from baseline at 7.6 km (location shown as dashed lines in (a) and (b)) due to medium and high flow, where the star indicates the location of the pulse.